A three amino acid sequence gates protein stability control of bHLH104 and iron uptake in *Arabidopsis thaliana*

Dibin Baby[1,2], Sarah Weldi[1], Marie Knopf[1], Vinitha Venkadasamy[1], Jessica Lee Erickson[3], Petra Bauer[1,2*]

[1]Institute of Botany, Heinrich Heine University, Düsseldorf 40225, Germany

[2]Cluster of Excellence on Plant Science (CEPLAS), Heinrich Heine University, Düsseldorf 40225, Germany

[3] Zentrum für Molekularbiologie der Pflanzen (ZMBP), Allgemeine Genetik, University of Tübingen, 72076 Tübingen, Germany.

***Corresponding author:** Petra Bauer, petra.bauer@hhu.de

Dibin Baby- https://orcid.org/0000-0003-0592-6067

Petra Bauer- https://orcid.org/0000-0002-0404-4532

Abstract

Iron (Fe) homeostasis is precisely regulated to prevent iron imbalance. The basic helix-loop-helix (bHLH) transcription factor bHLH104, a member of bHLH subgroup IVc, activates Fe uptake. bHLH104 is negatively controlled by the Fe-binding E3 ligase BRUTUS (BTS) that interacts with the C-terminus of bHLH104, according to predictions with involvement of the last three amino acids proline-alanine-alanine (PAA). Yet, experimental evidence for the PAA interaction site and importance for post-translational regulation are lacking. Here, we demonstrate the role of PAA for plant growth and bHLH104 regulation. Transgenic plants expressing a bHLH104 variant lacking the terminal PAA (*b104^dPAA*) have a constitutive Fe deficiency response. Strong accumulation of Fe causes *b104^dPAA* plants to have abnormal shoot and root development and delayed flowering, accompanied by mis-regulated Fe response and upregulated Fe acquisition genes. The severity of Fe accumulation phenotypes coincides with bHLH104 protein amounts. In plants, bHLH104 levels are controlled by proteasomal degradation in a PAA-dependent manner. Cell assays show that the PAA sequence is required for bHLH104 interaction with BTS and subsequent ubiquitination. Taken together, bHLH104 requires the terminal PAA to be post-translationally

controlled by BTS. Manipulation of bHLHIVc protein PAA sequence represents a biofortification strategy for crop plants.

60-word Plain language summary

Plants need iron but excess is harmful. Iron uptake transcription factor bHLH104 is negatively controlled by Fe-binding E3 ligase BTS. We show that three–amino acid terminal sequence of bHLH104 controls its breakdown by the BTS pathway. Removing PAA keeps bHLH104 active, driving constant iron uptake and iron accumulation phenotypes. Targeting this motif can be a strategy for crop biofortification.

Highlights of this study

- A conserved C-terminal PAA sequence in bHLH104 is required for its post-translational control in *Arabidopsis thaliana.*
- Expression of bHLH104 lacking the PAA sequence (*b104^dPAA*) perturbs Fe regulation, resulting in constitutive iron accumulation in plants depending on *b104^dPAA* protein levels.
- The PAA sequence mediates interaction with E3 ligases BTS and is essential for bHLH104 ubiquitination.

Keywords: *Arabidopsis thaliana*, iron, bHLHIVc, transcription factor, ubiquitination, BTS,

Introduction

Iron (Fe) is an essential micronutrient required for plant growth and development. It plays critical roles in photosynthesis, respiration, chlorophyll biosynthesis, and redox reactions (Briat et al., 2007; Jeong and Guerinot, 2009). Although Fe is abundant in the Earth's crust, it is mostly present in the ferric (Fe^{3+}) form, which is poorly soluble and difficult for plant roots to absorb—especially in alkaline or calcareous soils (Marschner, 2012). At the same time, excess Fe can be toxic due to its ability to generate reactive oxygen species (ROS) (Panda and Yamamoto, 2019). Therefore,

plants must tightly regulate Fe uptake, distribution, and storage to maintain internal balance.

In *Arabidopsis thaliana*, a group of basic helix–loop–helix (bHLH) IVc transcription factors—including bHLH34, bHLH104, ILR3 (bHLH105), and bHLH115—acts as an early regulatory module in the Fe deficiency (-Fe) response. These proteins activate the expression of internal Fe allocation and Fe deficiency response regulatory genes in roots and shoots (Schwarz and Bauer, 2020). Among their targets are also genes coding for bHLH Ib transcription factors that, together with the bHLH transcription factor FIT (FER-LIKE IRON DEFICIENCY-INDUCED TRANSCRIPTION FACTOR), induce root Fe uptake genes such as *IRT1* and *FRO2* (Long et al., 2010; Selote et al., 2015; Zhang et al., 2015; Li et al., 2016; Liang et al., 2017).

The regulation of bHLH IVc transcription factors is not fully understood. Notably, transcript levels of *bHLH IVc* genes do not change substantially under - Fe conditions (Zhang et al., 2015; Li et al., 2016; Liang et al., 2017), indicating that they are activated during the - Fe response primarily at protein level. One proposed mechanism involves post-translational regulation via the 26S proteasome mediated by the E3 ubiquitin ligase proteins, BRUTUS (BTS)/BTS-LIKE (BTSL) proteins. It is proposed that these E3 ligases target bHLHIVc proteins such as bHLH105/ILR3 and bHLH115 for degradation (Selote et al., 2015; Hindt et al., 2017). This hypothesis is particularly intriguing since stability of the BTS/BTSL E3 ligases is controlled by their N-terminus which contains hemerythrin domains for Fe and oxygen sensing (Selote et al., 2015; Pullin et al., 2025). It is possible, and supported by genetic studies that, BTS become destabilized under - Fe, resulting in their inactivation and allowing downstream targets such as bHLH IVc transcription factors to activate Fe uptake. However, molecular mechanisms are not yet fully resolved.

One bHLH IVc group protein is bHLH104 (Zhang et al., 2015; Li et al., 2016). The protein-level regulatory mechanisms controlling its function remain incompletely characterized. The C-terminus of bHLH104 can interact with BTS/L proteins (Lichtblau et al., 2022). It possesses a conserved C-terminal sequence. In our previous study, we showed that deleting this 25-amino-acid-long stretch abolished bHLH104 interaction with BTS (Lichtblau et al., 2022). T-DNA loss-of-function lines have an Fe deficiency-sensitive phenotype (Li et al., 2016). Previous studies have shown that

mutations at the C-terminal region of bHLH IVc proteins, including large deletions (60-64 amino acids) or point mutations at the terminal alanine residue, cause Fe accumulation phenotypes or disrupt interaction with proteosome components (Rampey et al., 2006; Zhao et al., 2016; Sharma and Yeh, 2020; Li et al., 2021). Structural predictions further revealed that a conserved three–amino acid short sequence—proline–alanine–alanine (PAA)—is located near the BTS-binding interface (Lichtblau et al., 2022). Hereafter, we refer to this as the PAA short sequence.

So far, it has not yet been demonstrated whether the PAA short sequence is important for bHLH104 regulation. The key open questions of this study were whether this minimal motif is necessary and sufficient for BTS engagement and ubiquitination, whether it governs bHLH104 protein abundance, and how its loss impacts Fe homeostasis and plant development. We show that the PAA short sequence plays a critical role for all these steps and in regulating Fe homeostasis properly in *planta*. Our work provides mechanistic insight into how bHLH104 is regulated and highlights the broad impact of post-translational control in nutrient signaling networks.

Results

Plants with bHLH104 lacking PAA (*b104^dPAA*) have distinct growth phenotypes

At first, we tested the hypothesis that the PAA short sequence plays a role in the functionality of bHLH104 in plants (Figure 1). We studied the growth of transgenic *Arabidopsis thaliana* lines in the wild-type Col-0 background expressing either regular full-length bHLH104 (*pb104::b104*) or a mutant deletion variant lacking the conserved PAA short sequence (*pb104::b104^dPAA*), both driven by the native *BHLH104* promoter (Figure 2A). Interestingly, obvious phenotypic variation was already visible in the T1 population of the *pb104::b104^dPAA* transgenics: While some plants displayed severely reduced growth with brown necrotic spots on leaves, others appeared indistinguishable from wild type (WT) (Supplementary Figure S1). To capture these contrasting phenotypes, we selected and propagated four *pb104::b104^dPAA* lines, two with severe phenotypes (#1, #2) and two with no obvious macroscopic phenotype (#3, #4), in addition to *pb104::b104 #1* and *#2* controls.

To quantify phenotypic variation across the life cycle, detailed morphological and physiological assessments were made with T3 plants grown on agar plates or soil. In 12-day-old seedlings*, pb104::b104^dPAA* lines *#1* and *#2* showed significantly shorter primary roots than #3, #4 or *pb104::b104* control lines (Figure 2B, 2C). Root Fe(III) reductase activity is necessary for Fe uptake in roots (Yi and Guerinot, 1996). Reductase activity measurements revealed that *pb104::b104^dPAA* lines *#1* and *#2* have high Fe reductase activity compared to #3, #4 and the control plants (Figure 2D). The machine-aided Phenospex PlantEye phenotyping platform can reliably depict minor variation in leaf color and rosette size in *A. thaliana* (Knopf and Bauer, 2025). By four weeks, *pb104::b104^dPAA* lines *#1* and *#2* displayed low rosette area (Figures 2E, 2F) and low normalized difference vegetation index (NDVI) values (Figure 2G), which indicate low chlorophyll content, photosynthetic efficiency and growth performance compared with other lines. Flowering was delayed compared to other lines (Figure 2H) and seed yield was significantly lower for *pb104::b104^dPAA* lines *#1* and *#2* compared to other lines (Figure 2I).

Having established that pb104::b104^dPAA lines exhibited distinct growth phenotypes (Figure 2), we selected among them representative lines for detailed molecular and physiological characterization. We focused subsequent analyses on pb104::b104^dPAA line #2, which showed strong phenotypes, and line #3, which showed mild phenotypes, to comprehensively analyze Fe content, gene expression, and the molecular basis of these phenotypes.

Reduced root and shoot growth can be a consequence of Fe toxicity in plants (Naranjo-Arcos et al., 2017). Thus, we tested whether the growth defects observed in *pb104::b104^dPAA* plants were alleviated in conditions of Fe deficiency. We grew the representative lines on alkaline calcareous soil (ACS; pH 8.1), which provides Fe-limiting conditions (Supplementary Figure S2; Knopf and Bauer, 2025). Notably, *pb104::b104^dPAA line #2*, which exhibited pronounced growth defects in control soil (pH 5.9), showed increased 3D leaf area in ACS, indicating partial recovery under Fe-limited ACS conditions (Supplementary Figure S2C). NDVI values, which were reduced when grown in control soil, were restored to near-WT levels in ACS, suggesting improved leaf health (Supplementary Figure S2D). While flowering remained delayed relative to WT, it occurred earlier in ACS than in control soil (Supplementary Figure S2E). These findings show that the growth defects observed

in control soil are largely alleviated when Fe availability is limited, linking the b104^dPAA-associated phenotypes to Fe status.

Together, these results show that removal of the PAA short sequence in bHLH104 can lead to drastic dominant growth phenotypes across the life cycle. To explore whether these phenotypes reflect altered Fe homeostasis, we next examined tissue Fe content and expression of Fe-responsive genes in both seedlings and plants at the reproductive stage.

b104^dPAA can Cause Constitutive Iron Uptake and Transcriptional Misregulation of Fe Deficiency Response genes in Seedlings

After few days of germination, *A. thaliana* seedlings rely on external Fe supply. To assess whether b104^dPAA affects Fe homeostasis during early development, we measured total Fe content via ICP-MS and analyzed gene expression profiles in 10-day-old seedlings of WT, control and contrasting *pb104::b104^dPAA* lines #2 and #3 in both +Fe and -Fe conditions (Figure 3A, B). As an additional control, *pUBQ10::b104* lines express full-length bHLH104 constitutively from the strong UBIQUITIN10 promoter, allowing us to assess whether high transcript levels alone affect Fe homeostasis. Phenotypically, *pUBQ10::b104* lines #1 and #2 are indistinguishable from WT (Supplementary Figure S3).

Elemental profiling revealed that *pb104::b104^dPAA* line #2 accumulated substantially more Fe than all other genotypes under both +Fe and –Fe conditions (Figure 3C). This increase was observed in both roots and shoots, with roots showing higher Fe levels than shoots. In contrast, *pb104::b104^dPAA* line #3 and the *pb104::bHLH104* and *pUBQ10::b104* lines had Fe contents similar to WT. All lines exhibited reduced Fe contents under –Fe, confirming the effectiveness of the treatment (Figure 3C).

Differences were also detected for manganese (Mn), zinc (Zn), and copper (Cu) levels (Supplementary Figure S4). Uptake of these metal ions is closely connected with Fe homeostasis (Connolly et al., 2002). In *pb104::b104^dPAA* line #2, Zn and Cu were elevated in roots under –Fe, and Cu was also increased in shoots. Notably, Zn levels were elevated even under +Fe in *pb104::b104^dPAA* roots compared to WT. Roots of *pUBQ10::b104* lines also showed increased Mn under –Fe compared to WT. Metal concentrations in the other lines were similar to WT. Hence, these findings suggest that *pb104::b104^dPAA* line #2 has increased Fe accumulation and affects the uptake

189 of other micronutrients like Zn and Cu. This highlights the importance of proper
190 regulation of bHLH104 function in maintaining metal homeostasis under varying Fe
191 conditions.

192 To elucidate the transcriptional response, we analyzed gene expression patterns via
193 RNA-seq following -Fe treatment at the seedling stage in both root and shoot tissues.
194 The highest number of differentially expressed genes (DEGs) was observed in shoot
195 tissue of *pb104:b104^dPAA #2* line, with 4,645 DEGs under +Fe conditions and 2,857
196 DEGs under -Fe conditions after 10 days of treatment, compared to WT. There was
197 also substantial differential expression in roots, with 1,210 DEGs under +Fe conditions
198 and 111 DEGs under -Fe conditions (Supplementary Figure S5A).

199 Gene Ontology (GO) analysis revealed that the upregulated genes in shoot tissue of
200 the *pb104:b104^dPAA* #2 plants were enriched in terms related to hypoxia and
201 oxidative stress, while genes associated with photosynthesis were downregulated. In
202 *pb104:b104^dPAA* root tissue, upregulated gene categories were additionally
203 enriched for terms related to metal ion transport, while downregulated categories
204 showed enrichment for cell wall modification-related GO terms (Supplementary Figure
205 S5B). Hence, the *pb104:b104^dPAA* #2 plants indeed show symptoms of Fe overload.

206 We examined the expression patterns of selected genes involved in Fe uptake and
207 homeostasis regulation to characterize their specific regulatory expression profiles.
208 *BHLHIVc* genes, *BHLH104, ILR3*, and *BHLH115*, were upregulated in the roots of the
209 *pb104::b104^dPAA line #2* under +Fe compared to other lines (Figure 3D). Their target
210 genes, such as *BHLH39, BHLH100, IMA1*, *PYE, BTS, BTSL1* and BTSL2, were also
211 upregulated, indicating activation of the Fe deficiency response signaling. Likewise,
212 the further downstream targets in roots, like Fe acquisition genes *IRT1, FRO2, FIT,*
213 were up-regulated (Figure 3D), consistent with the elevated Fe uptake and Fe content.
214 Interestingly, expression of negative regulators of the Fe deficiency response and of
215 Fe sufficiency markers, such as *BHLH11* and FER1 were also increased, suggesting
216 a proper response to sufficient Fe, but a failure in feedback repression mechanisms
217 (Figure 3D). In the shoot tissue, the Fe storage related gene *FER1* and transcription
218 factor bHLH121 were strongly upregulated in *pb104::b104^dPAA line #2* compared to
219 controls, regardless of Fe availability, in agreement with the elevated Fe content in this
220 line (Figure 3D). Targeted expression profiling using reverse transcription quantitative

PCR (RT-qPCR) in seedling-stage samples confirmed expression patterns to those observed in the transcriptome analysis (Supplementary Figure S6).

To summarize, the misregulation of Fe response genes indicates that bHLH104 with deleted PAA disrupts normal Fe homeostasis by constitutively activating Fe acquisition while preventing proper feedback inhibition during seedling development.

b104^dPAA Causes Constitutive Fe Uptake and Transcriptional Misregulation at a Reproductive Growth Stage

Plants redistribute nutrients during reproduction to support flowering and seed development (Waters and Grusak, 2008; Pottier et al., 2018). To assess whether b104^dPAA affects Fe homeostasis during later developmental stages, we analyzed 30-day-old Arabidopsis plants grown hydroponically and subjected to a 3-day ±Fe treatment (Figure 4A). This time, we focused on *pb104::b104^dPAA #3*. Due to its severe developmental delay and low biomass regarding very severe growth defects, *pb104::b104^dPAA #2* had to be excluded from this analysis and was examined separately, as described later (Figure 4B). Old leaves, young leaves, and roots were collected for gene expression analysis, as described in (Ngigi et al., 2025) (Figure 4C-D).

Elemental profiling showed that although there were no differences from WT at the seedling stage, *p104::b104^dPAA line #3* accumulated more Fe than control lines at the late developmental stage (Figure 4E). Under +Fe, roots of *pb104::b104^dPAA* #3 had increased Mn and Zn levels compared to WT (Supplementary Figure S7). Cu levels were similar as WT.

In transcriptome analysis, *pb104:b104^dPAA* #3 plants had the highest DEG counts in young leaves (3,877 DEGs) and old leaves (1,895 DEGs) under +Fe conditions compared with controls, while root tissue exhibited minimal differential expression differences (71 DEGs) (Supplementary Figure S8A). GO term enrichment analysis revealed that genes associated with immune response were significantly upregulated in both old and young leaves of *pb104:b104^dPAA* #3 plants under +Fe conditions. In contrast, 3-day -Fe treatment resulted in the upregulation of genes related to Fe homeostasis in young leaves and roots (Supplementary Figure S8B). This indicates a tissue-specific transcriptional response to iron availability at the reproductive stage.

Specifically, expression analysis showed that in roots of *pb104::b104^dPAA line #3* genes were upregulated under +Fe, similar as we reported above for the #2 line at the seedling stage, namely upregulation of *BHLHIVc* genes, Fe deficiency response, Fe sufficiency marker and negative regulator genes (Figure 4F). Interestingly, Fe deficiency response genes were not upregulated under –Fe in *pb104::b104^dPAA line #3*, suggesting that the –Fe response may have been suppressed due to negative feedback signaling caused by elevated internal Fe levels in this line, in contrast to controls where these genes were upregulated (Figure 4F). In line with this notion, the Fe storage gene *FER1* was upregulated in the leaves of *pb104::b104^dPAA* line #2 compared to controls. Targeted expression profiling by RT-qPCR confirmed again the patterns (Supplementary Figure S9).

Finally, as *pb104::b104^dPAA* line #2 grew poorly in +Fe hydroponic conditions, we modified the hydroponic growth system and changed to a Fe resupply assay. Seedlings were transferred to -Fe medium for 27 days, followed by a 3-day +/- Fe resupply. Here, we found interesting phenotypes. While controls remained chlorotic and accumulated Fe mostly in the roots following the Fe resupply, *pb104::b104^dPAA* line #2 showed substantial Fe accumulation in root and leaves despite persistent leaf chlorosis, suggesting very high root-to-shoot Fe translocation. Interestingly, *pb104::b104^dPAA* line #2 accumulated significantly less Mn, Zn, Cu compared to control plants (Supplementary Figure S10). This shows that at the reproductive stage, there is a particularly elevated Fe uptake and translocation towards shoots in *pb104::b104^dPAA* #2 compared to the control.

Since *pb104::b104^dPAA* lines accumulated not only Fe but also Mn, Zn, and Cu, we examined the possibility that this might have been caused by altered expression of metal transporter genes. We found elevated *NRAMP1*, *COPT2*, *MTP8*, and *ZIP* family members in *pb104::b104^dPAA* roots under +Fe at the seedling stage (Supplementary Figure S11). Interestingly, under –Fe, transporter gene expression levels were lower, yet Mn, Zn and Cu accumulation were higher, suggesting that in the absence of Fe, other metals are taken up more efficiently (Supplementary Figures S7 and S11). At the reproductive stage, *pb104::b104^dPAA* roots maintained high expression of metal transporters including *NRAMP1, ZIP3, COPT2, MTP8,* and *ZIP9*, yet only Fe accumulated, but not other elements, indicating Fe is the primary target despite activation of multiple metal transporters (Supplementary Figure S11). Interestingly, Fe

acquisition and mobilization genes were constitutively upregulated in *pb104::b104^dPAA* lines regardless of Fe availability at the seedling stage (Supplementary Figure S12).

To summarize, Fe accumulation is elevated in *pb104::b104^dPAA* lines during the reproductive stage, consistent with patterns observed at the seedling stage and with iron and metal transporter gene regulation patterns. Overall, these findings show that metal accumulation and associated phenotypes due to *b104^dPAA* expression remain consistent from seedling to reproductive plant developmental stages.

The PAA short sequence is required for 26S Proteasome-mediated degradation of bHLH104

The severity of phenotypes in *pb104::b104^dPAA* lines was not explained by differences in transgene transcript levels (Supplementary Figures S6, S9). Additionally, *pUBQ10::b104* lines showed no significant phenotype compared to WT despite elevated *bHLH104* transgene expression (Supplementary Figure S3, Supplementary Figure S6). Therefore, we predicted that variation in bHLH104 protein accumulation underlies the observed phenotypic differences.

We thus examined *in vivo* accumulation of mTurquoise2-tagged bHLH104 and b104^dPAA proteins, expressed under either the UBQ10 or bHLH104 promoter (Figure 5A, B). Immunoblotting of root tissue proteins revealed high accumulation of b104^dPAA protein in *pb104::b104^dPAA* lines #1 and #2, correlated with their strong phenotypes (Figure 5B). In contrast, full-length bHLH104 protein was barely detectable in both *pb104::bHLH104* and *pUBQ10::b104* lines. *pb104::b104^dPAA* lines #3 and #4 showed lower protein abundance, corresponding to weaker phenotypes.

To check whether the low abundance of bHLH104 is due to proteasomal degradation, we treated samples with proteosome inhibitor MG132. MG132 treatment stabilized full-length bHLH104 in *pUBQ10::b104* lines by more than two-fold. However, MG132 treatment did not affect the abundance of bHLH104 in any native promoter lines (Figure 5B-C). To confirm that bHLH104 is subject to proteasomal degradation, a cell-free degradation assay was performed. When bHLH104 protein was incubated with whole protein extracts from WT seedlings, it was rapidly degraded. This degradation

316 was inhibited by the proteasome inhibitor MG132, supporting the involvement of the
317 26S proteasome (Figure 5D).

318 Confocal imaging of root meristems further confirmed the increased abundance of
319 b104^dPAA, as indicated by strong fluorescence signals in *pb104::b104^dPAA* lines,
320 whereas fluorescence was undetectable in lines expressing full-length bHLH104
321 (Figure 5E).

322 Altogether, these findings show that the PAA short sequence is most required for
323 degradation of bHLH104 by the 26S proteasome. Removing this short sequence
324 prevents normal turnover of the protein and is correlated with increased Fe uptake and
325 associated phenotypes.

326 **The C-terminal PAA sequence of bHLH104 mediates interaction with BTS E3**
327 **ligases and enables ubiquitination**

328 To understand how the PAA sequence contributes to bHLH104 degradation, we
329 examined its role in mediating interaction with BTS.

330 AlphaFold2 multimer modeling (Evans et al., 2021; Jumper et al., 2021) and
331 electrostatic surface analysis (Pettersen et al., 2004) revealed a charge-based
332 interface with high pLDDT scores, indicating strong confidence in the predicted
333 structure (Figure 6A-B). These models suggest that the PAA sequence forms a stable
334 and specific docking surface for BTS, likely critical for E3-substrate recognition.

335 To further study protein interaction in the presence and absence of PAA experimentally,
336 we made use of established protein expression systems. Due to the difficulties of
337 detecting bHLH104 and BTS in plant cell assays, we opted for the yeast two hybrid
338 (Y2H) assay (Lichtblau et al., 2022). BTS interacts with the C-terminal part of bHLH104
339 (bHLH104-C) in yeast, and bHLH104-C does not auto-activate in the yeast-two-hybrid
340 (Y2H) system (Figure 6C) (Lichtblau et al., 2022). We now tested whether interaction
341 is different with bHLH104-C^dPAA. Indeed, deletion of the PAA sequence abolished
342 the interaction with BTS (Figure 6D). bHLH104 is known to homodimerize (Zhang et
343 al., 2015; Li et al., 2016; Lichtblau et al., 2022). bHLH104-C^dPAA still dimerized with
344 bHLH104-C, confirming that bHLH104-C^dPAA is present and properly folded in yeast
345 cells. A similar loss of interaction was observed between bHLH104-C-dPAA and and

346 BTSL1 and BTSL2 (Supplementary Figure S13), indicating that the PAA sequence is
347 broadly required for recognition by BTS/ BTSL E3 ligases.

348 To test whether bHLH104 is ubiquitinated by BTS with requirement of the short
349 sequence PAA, we established the bacterial UbiGate system (Kowarschik et al., 2018;
350 Ortmann et al., 2023) to reconstitute a BTS-dependent ubiquitin-conjugation cascade
351 for bHLH104 (Figure 6E). Previous reports on the ubiquitination activity of BTS have
352 been based on *in vitro* ubiquitination assays (Selote et al., 2015; Rodríguez-Celma et
353 al., 2019). However, *in vitro* studies are often ambiguous as purified target proteins
354 are contained in a reaction mix. In this study, we employed the UbiGate system, in
355 which all components of the ubiquitination cascade—including ubiquitin, E1, E2, E3
356 ligases, and the substrate protein—are co-expressed in bacterial cells, a far more
357 complex environment than an *in vitro* reaction. The resulting ubiquitination patterns
358 are analyzed directly from bacterial cell lysates. Each component is fused to a distinct
359 epitope tag, allowing individual tracking and detection of the proteins involved. Since
360 full-length BTS is unstable in *E. coli*, we used a truncated version (BTS-HC) lacking
361 the first two hemerythrin domains. In the presence of E1, E2 (UBC8), and BTS-HC,
362 bHLH104-C was polyubiquitinated, while, in contrast, this was not the case for b104-
363 C^dPAA (Figure 6F). BTS ubiquitination served as a control. It has been reported that
364 BTS undergoes autoubiquitination (Selote et al., 2015), which we also observed in our
365 assay. bHLH115 has been previously proposed as a target of BTS-dependent
366 degradation (Selote et al., 2015; Xing et al., 2021). As a validation of the UbiGate
367 assay, we confirmed that BTS directly ubiquitinated bHLH115 (Supplementary Figure
368 S14).

369 These results provide direct biochemical evidence that bHLH104 is a substrate of BTS
370 inside living cells and that the PAA short sequence is required for both physical
371 interaction and ubiquitination. Deletion of PAA sequence disrupts recognition and
372 ubiquitination by BTS.

373

374 **Discussion**

375 Our findings in this study demonstrate that the terminal PAA short sequence of
376 bHLH104 is most relevant for bHLH104 control via proteasome-mediated turnover.
377 Lack of PAA leads to higher abundance and a stabilization of bHLH104, constitutive

Fe uptake, and transcriptional misregulation across developmental plant growth stages. The PAA sequence is directly involved in protein interaction and ubiquitination by BTS, highlighting its importance as an E3 ligase–interaction interface in maintaining Fe homeostasis through post-translational regulation of transcription factors and transcriptional output.

bHLH104 abundance is controlled via the proteasome

The regulation of bHLH104 activity at protein level had been largely unknown, but regarded relevant (Zhang et al., 2015; Li et al., 2016; Liang et al., 2017). Our results show that wild-type bHLH104 protein is susceptible to degradation in a plant cell environment, and inhibition of the proteasome pathway increases bHLH104 abundance. Interestingly, despite having high *BHLH104* transcript levels, pUBQ10::b104 lines showed no phenotype, implying that protein stability, rather than transcript level, determines bHLH104 activity.

The direct interaction of bHLH104 with the BTS E3 ligase has been reported previously (Long et al., 2010; Selote et al., 2015; Lichtblau et al., 2022), and genetic evidence supported a regulatory relationship between BTS and bHLH104 (Zhang et al., 2015). The *bts-2* mutant exhibits increased Fe uptake similar to bHLH104 overexpression, whereas *bts-2 bhlh104-2* double mutants lose this phenotype, confirming that BTS negatively regulates bHLH104 function (Zhang et al., 2015). Recent studies have identified that BTS interacts with the C-terminal region of bHLHIVc proteins (Li et al., 2021; Lichtblau et al., 2022). Interestingly, C-terminal mutations in bHLH IVc proteins in other plant species also result in Fe accumulation (Rampey et al., 2006; Zhao et al., 2016; Sharma and Yeh, 2020), suggesting the functional importance of this conserved region. We tested this hypothesis and identified that PAA is needed for BTS interaction. We propose a model (Figure 7) in which bHLH104 protein is maintained at low abundance through proteasome-mediated degradation. Lack of the PAA sequence increases bHLH104 protein abundance, which results in increased Fe uptake in plants. A limitation of this study is the difficulty in visualizing mTurquoise2-tagged bHLH104 in planta under standard conditions, and the relatively low abundance of b104^dPAA protein suggests that additional regulatory mechanisms beyond PAA-mediated degradation may exist. Future studies should investigate other post-translational modifications and identify conditions that promote bHLH104 stabilization.

410

411 **b104^dPAA perturbs Fe regulation and metal homeostasis**

412 bHLHIVc transcription factors are functionally redundant (Zhang et al., 2015; Li et al.,
413 2016; Liang et al., 2017). Our study showed that gain-of-function of bHLH104 alone
414 caused a physiological effect in *pb104::b104^dPAA* lines where bHLH104 protein
415 abundance was increased. Notably, *pb104::b104^dPAA* lines accumulated not only Fe
416 but also Mn, Zn, and Cu, which coincided with elevated expression of *NRAMP1*,
417 *COPT2*, *MTP8*, and *ZIP* family members in *pb104::b104^dPAA* roots under +Fe. This
418 indicated that indeed excessive metal acquisition was a consequence of elevated
419 gene expression and resulting transporter activity in these cases. The lower metal
420 transporter gene expression at -Fe when elevated Mn, Zn and Cu accumulation was
421 noted, was indeed surprising, suggesting that in the absence of Fe, other metals are
422 taken up more efficiently, perhaps through the regular -Fe-induced Fe acquisition
423 routes involving IRT1 (Vert et al., 2002). Indeed, the multi-metal accumulation can be
424 explained by persistent activation of broad-specificity transporters IRT1 and NRAMP1,
425 which transport Fe, Mn, Zn, and Cu (Connolly et al., 2002; Vert et al., 2002; Cailliatte
426 et al., 2010). This pattern is also consistent with reports that heavy metals like Zn can
427 induce Fe deficiency responses at the level of Fe sensing rather than by directly
428 inhibiting Fe transport (Lešková et al., 2017), suggesting that accumulated metals may
429 reinforce the Fe deficiency signal in *pb104::b104^dPAA* plants. Similar phenotypes
430 where Fe accumulation disrupts plant growth have been reported in *BTS* loss-of-
431 function mutants and in overexpression lines of *BHLH39* or *BHLH105* (Zhang et al.,
432 2015; Li et al., 2016; Hindt et al., 2017; Naranjo-Arcos et al., 2017). A still unresolved
433 question is why the known negative post-translational regulation mechanisms, e.g.
434 IRT1 ubiquitination and degradation under low Fe and excessive Zn and Mn, are not
435 in place here (Dubeaux et al., 2018; Abuzeineh et al., 2022). Perhaps this type of
436 regulation requires that Zn and Mn are supplied in the rhizosphere rather than inside
437 the root. In our experimental settings, excessive Zn and Man were not supplied and
438 Zn and Mn accumulated due to plant internal misbalance.

439 We observed that b104^dPAA protein abundance in seedling roots correlated with
440 phenotype severity among *pb104::b104^dPAA* lines. A plausible explanation is that
441 this variation in protein abundance across lines results from differences in transgene

copy number arising from the floral dip transformation method (Gelvin, 2003). Notably, *pb104::b104^dPAA line #3*, which showed negligible b104^dPAA protein in seedling roots, grew normally during early development but accumulated Fe in leaves at the reproductive stage. This suggests that minimal b104^dPAA activity can increase Fe content without causing severe growth defects, highlighting potential for Fe biofortification strategies. Additional investigations are required to determine the precise threshold at which bHLH104 protein levels affect plant function without compromising growth. In sum, our discovery that a three–residue PAA sequence gates BTS-mediated turnover of bHLH104 delivers a precise target for tuning Fe acquisition in plants. The findings integrate with emerging work on BTS/BTSL hemerythrin-based Fe/oxygen sensing (Selote et al., 2015; Pullin et al., 2025) and clarify how post-translational control translates Fe status into transcriptional outputs.

Pleiotropic and tissue-specific effects of b104^dPAA

The phenotypes observed in *pb104::b104^dPAA* plants extend beyond simple Fe accumulation, suggesting that constitutive Fe deficiency signaling has broader physiological consequences. Several phenotypes observed in these lines may reflect activation of multiple stress regulatory pathways. First, the delayed flowering phenotype may result from -Fe response signaling interfering with flowering time control through epigenetic, circadian, and hormone pathways (Cheng et al., 2004; Salomé et al., 2012; Chen et al., 2013; Hong et al., 2013; Wild et al., 2016; Dutta et al., 2017; Maruoka et al., 2022). Second, gene ontology analysis of *pb104::b104^dPAA* leaves showed enrichment of immune signaling and salicylic acid signaling terms. Fe deficiency treatment is known to elevate salicylic acid levels and induce salicylic acid-responsive genes (Shen et al., 2016), and bHLH105 can integrate Fe homeostasis with plant immune responses against pathogens (Rampey et al., 2006; Aparicio and Pallás, 2017; Samira et al., 2018). This suggests that the Fe deficiency response is interconnected with immune signaling pathways.

Expression of b104^dPAA in *pb104::b104^dPAA* lines results in distinct tissue-specific consequences. The absent upregulation of internal Fe allocation genes such as *BTS, PYE, IMA1*, *BHLH100, BHLH39* under -Fe condition in the leaves of mature *pb104::b104^dPAA* lines suggests that elevated local Fe levels in the leaves must normally suppress systemic Fe deficiency signaling upstream of bHLH104, consistent with recent evidence that leaf Fe responses are determined mainly by local Fe status

475 rather than root-derived systemic signals (Nguyen et al., 2022; Ngigi et al., 2025). In
476 contrast, in roots of *pb104::b104^dPAA* lines, -Fe acquisition genes such as *FIT*, *IRT1*
477 and *FRO2* were upregulated. This indicates that, rather than systemic signaling, an
478 active and constitutive Fe acquisition response is maintained in the roots. In wild-type
479 plants, bHLH104 is likely stabilized only under Fe deficiency, enabling transient
480 activation of uptake genes. Lack of PAA prevents this regulation, resulting in
481 constitutive bHLH104 activity and continuous Fe uptake regardless of Fe status.
482 Interestingly, we observed enhanced Fe mobilization to young leaves in
483 *pb104::b104^dPAA line #2* after 3 days of Fe supply following growth in –Fe. In
484 contrast, wild-type plants retained most Fe in roots. Increased *IRT1* expression when
485 b104^dPAA is expressed aligns with recent findings that IRT1 protein, independent of
486 its Fe(II) transport activity, is necessary for effective root-to-shoot Fe partitioning
487 (Quintana et al., 2022). This shows that bHLH104 protein stability serves as a critical
488 control point linking Fe sensing to transcriptional responses in roots, whereas leaves
489 respond primarily to local Fe availability through independent regulatory mechanisms.
490 Grafting experiments would help determine whether the effects of stabilized bHLH104
491 are root-autonomous or involve systemic signaling to shoots.

492 **The short sequence PAA is critical for protein interaction**

493 The present study found that the terminal PAA sequence of bHLH104 mediates critical
494 interactions. Additionally, small proteins IMA1 and IMA3, which interact with BTS and
495 BTSL1, also contain a conserved C-terminal PAA sequence, indicating that this
496 sequence is broadly conserved for E3 ligase recognition (Li et al., 2021; Lichtblau et
497 al., 2022). Other members of the bHLH IVc family have instead a PVA terminal
498 sequence. It has not yet been examined which role PVA plays and whether it is similar
499 to PAA. One possible explanation is that the middle alanine in the PAA sequence of
500 bHLH104 may not be essential. Proline is structurally distinctive because its cyclic side
501 chain imparts rigidity and promotes tight turns in protein structure, suggesting that the
502 proline residue plays a critical structural role (Melnikov et al., 2016). Previous studies
503 have shown the significance of terminal alanine residue in bHLH IVc protein regulation.
504 The terminal alanine in bHLH115 and bHLH105 is essential for BTS interaction (Li et
505 al., 2021), while overexpression of bHLH34 with its terminal alanine substituted to
506 valine resulted in a metal accumulation phenotype similar to our observations (Sharma
507 and Yeh, 2020). Taken together, these observations support the conclusion that the

508 PAA sequence is required for the recognition of bHLH104 by the proteasomal
509 degradation system. The conservation of this sequence in bHLH104 orthologues, and
510 its presence with minor variations in other bHLH IVc members, suggests the existence
511 of a conserved BTS(L) recognition interface within the family. In future studies, the
512 specificity and position effects of each amino acid in the PAA and PVA short sequences
513 can be further examined. It will also be interesting to test whether artificial addition of
514 PAA to transcription factors can target them for degradation by BTS/L proteins under
515 Fe deficiency. If so, this can be exploited in the future in synthetic and biotechnological
516 approaches.

517 **Concluding remarks and perspectives**

518 This study provides evidence that a short three–amino acid PAA sequence in
519 bHLH104 is required for post-translational regulation of protein abundance and
520 activity.

521 The conserved PAA sequence provides opportunities for biotechnological
522 applications. As bHLH IVc proteins are conserved across plant species (Jiang et al.,
523 2024), genome editing of this sequence in crop orthologues may enhance Fe
524 accumulation for biofortification. In contrast to whole-gene overexpression, precise
525 PAA editing offers potential to increase Fe content while minimizing pleiotropic effects.
526 However, because the PAA sequence is also present in IMA proteins, which positively
527 regulate Fe uptake, editing approaches must specifically target bHLH IVc genes
528 without affecting *IMA* genes. Testing whether PAA addition to other transcription
529 factors targets them for BTS/BTSL-mediated degradation could enable Fe-responsive
530 protein degradation systems for synthetic biology applications.

531 Overall, our findings provide comprehensive evidence which shows that post-
532 translational regulation of bHLH104 is necessary to maintain a balance between Fe
533 acquisition and normal growth and development, and that disrupting this control can
534 lead to wide-ranging physiological effects. This research has direct impact for
535 improving crop productivity on alkaline/calcareous soils and under climate stress.
536 Identifying sequence motifs that control master regulators of Fe uptake such as
537 bHLH104 provides paths for crop improvement and biofortification. Our discovery that
538 a three–residue PAA motif gates BTS-mediated turnover of bHLH104 delivers a
539 precise target for tuning Fe acquisition in plants. Given current efforts to enhance

540 micronutrient use efficiency and nutritional quality, these insights are both
541 mechanistically fundamental and directly translatable.

542

543

544 **Materials and methods**

545 **Gene Accession numbers**

546 The following *Arabidopsis thaliana* genes were the focus of this study: bHLH104
547 (AT4G14410), BTS/BRUTUS (AT3G18290), BTSL1 (AT1G74770), and BTSL2
548 (AT1G18910).

549 **Plant Material and Growth Conditions**

550 *Arabidopsis thaliana* Columbia-0 (Col-0) was used as the wild type in this study. The
551 transgenic lines pbHLH104::mTurquoise2:bHLH104,
552 pUBQ10::mTurquoise2:bHLH104, and pbHLH104::mTurquoise2:b104^dPAA were
553 used for phenotypic and molecular analyses.

554 Seeds were surface-sterilized in 6% (v/v) sodium hypochlorite solution supplemented
555 with 0.1% (v/v) Triton X-100 for 8 min, followed by five washes with sterile distilled
556 water. Sterilized seeds were stratified in the dark at 4°C for 48 h before sowing.

557 For plate-based experiments, seeds were germinated and grown vertically on modified
558 Hoagland agar medium containing 1.5 mM $Ca(NO_3)_2 \cdot 4H_2O$, 0.5 mM KH_2PO_4, 1.25
559 mM KNO_3, 0.75 mM $MgSO_4 \cdot 7H_2O$, 50 μM H_3BO_3, 25 μM KCl, 10 μM $MnSO_4 \cdot H_2O$, 2
560 μM $ZnSO_4 \cdot 7H_2O$, 1.5 μM $CuSO_4 \cdot 5H_2O$, and 0.075 μM $(NH_4)_6Mo_7O_{24}$, supplemented
561 with 1% (w/v) sucrose and 1.4% (w/v) plant agar, pH adjusted to 5.8. Iron was supplied
562 as 50 μM Fe(III)-EDTA for Fe-sufficient conditions (+Fe) or omitted for Fe-deficient (-
563 Fe) conditions. Seedlings were grown under long-day photoperiods (16 h light/8 h
564 dark) at 21°C, under white light at 120 μmol m^{-2} s^{-1} (CLF Plant Climatics). For Fe
565 deficiency experiments, seedlings were grown for 10 days before tissue collection. For
566 root length measurements, an independent set of seedlings was grown on Hoagland
567 plates for 12 days prior to measurement.

568 For hydroponic experiments, seedlings were initially grown on Hoagland agar plates
569 for 12 days before being transferred to a hydroponic setup based on a quarter-strength

570 Hoagland solution (Nguyen et al., 2016) containing 0.75 mM $Ca(NO_3)_2$, 0.625 mM
571 KNO_3, 0.25 mM KH_2PO_4, 0.375 mM $MgSO_4$, 25 µM H_3BO_3, 25 µM KCl, 5 µM $MnSO_4$,
572 1 µM $ZnSO_4$, 0.75 µM $CuSO_4$, and 0.0375 µM $(NH_4)_6Mo_7O_{24}$. Fe was supplied as 25
573 µM FeNaEDTA (+Fe). The nutrient solution was replaced every three days and
574 continuously aerated using air pumps. Plants were grown under the same
575 photoperiod, light intensity, and temperature conditions as plate-grown seedlings.
576 Hydroponic growth continued until 27 days after germination, at which point plants
577 were divided into +Fe and –Fe conditions by either maintaining or omitting FeNaEDTA.
578 After three days of treatment (day 30), tissues were harvested, immediately frozen in
579 liquid nitrogen, and stored at –80°C.

580 For soil-based phenotyping experiments, seedlings were transferred to soil on the
581 eighth day after germination. Plants were grown in growth cabinets (Polyklima, True
582 Daylight + LED) under long-day conditions (16 h light/8 h dark) with a light intensity of
583 98–112 $\mu mol \cdot m^{-2} \cdot s^{-1}$. The temperature was maintained at 21°C during the light period
584 and 19°C during the dark period. Humidity was not controlled. Soil was prepared using
585 a peat-based substrate, and the pH was determined as described below. Eight plants
586 per genotype were grown, with eight pots fitted per tray. Phenotypic measurements
587 were taken after three weeks of soil growth.

588 **Generation of Transgenic Lines**

589 Constructs for generating transgenic lines were assembled using the GreenGate
590 cloning system (Lampropoulos et al., 2013). For the
591 pbHLH104::mTurquoise2:bHLH104 and pbHLH104::mTurquoise2:bHLH104^dPAA
592 constructs, a 1636-bp promoter region upstream of the bHLH104 start codon was
593 amplified and inserted into the pGGA000 entry vector. The coding sequences of
594 bHLH104 (852 bp) and bHLH104^dPAA (843 bp) were separately cloned into the
595 pGGC000 entry vector. The bHLH104 terminator sequence (975 bp) was cloned into
596 the pGGE000 entry vector. For both constructs, an N-terminal mTurquoise2
597 fluorescent tag from pGGB009 and a dummy linker sequence from pGGD002 were
598 included. The selection cassette (pUBQ10::HygromycinR::tOCS) was provided by
599 pGGF005. All entry modules were combined into the pGGZ003 destination vector
600 through a single GreenGate assembly reaction. Primers used are listed in
601 Supplementary Table 1.

602 For the pUBQ10::mTurquoise2:bHLH104 construct, the UBQ10 promoter was cloned
603 from the pGGA006 entry vector to drive expression of the mTurquoise2-tagged
604 bHLH104 coding sequence. The remaining modules, including the coding sequence,
605 dummy linker, terminator, and selection cassette, were assembled as described
606 above. Primers used in this study is listed in Supplementary table S1.

607 All final plasmids were verified by sequencing and introduced into Rhizobium
608 radiobacter strain GV3103 (pSOUP). Arabidopsis thaliana Col-0 plants were
609 transformed using the floral dip method (Clough and Bent, 1998). Transgenic
610 seedlings were selected on hygromycin-containing medium. Independent T1 lines
611 were established and propagated and used for phenotypic and molecular analyses.

612 **Phenotyping and Image Acquisition**

613 Automated phenotyping was performed using the MicroScan system equipped with a
614 PlantEye F600 sensor (Phenospex, Heerlen, The Netherlands) and controlled by the
615 implemented software HortControl (Phena version 2.0, HortControl version 3.85). To
616 minimize interference from non-plant background, image analysis was optimized by
617 removing color information corresponding to Hue values between 200° and 360° (blue
618 to purple) as previously described (Arend et al., 2016; Hüther et al., 2020; Knopf and
619 Bauer, 2025).

620 Plants were individually measured by placing the pots into a blue holder, which fixed
621 the plant height and ensured positioning within the scanning unit. For technical
622 replication, plant pots were rotated by 90° between successive measurements.

623 The PlantEye system recorded three-dimensional and spectral parameters. The three-
624 dimensional surface area of the plants (3D leaf area, in mm^2) was determined. Spectral
625 data included, the normalized difference vegetation index (NDVI), calculated as (near-
626 infrared reflectance [NIR] − red reflectance [RED])/(NIR + RED). For each parameter,
627 both the average value per plant and the percentage of voxels falling within predefined
628 ranges were calculated automatically using the preset analysis settings implemented
629 in the HortControl software.

630 Root length was manually measured from plate-grown seedlings using Fiji (ImageJ).

631 Flowering time was determined by measuring the height of the primary inflorescence
632 shoot. A plant was considered to have reached flowering if the inflorescence shoot

633 exceeded 1.5 cm. If a shoot was greater than 2 cm on the previous day, or greater
634 than 3 cm two days earlier, the respective earlier day was recorded as the flowering
635 time.

636 Seed number was estimated based on seed weight. For each biological replicate, 100
637 seeds were manually counted and weighed to determine the mean weight per 100
638 seeds. The total seed weight per sample was then measured, and the total seed
639 number was calculated as (total seed weight/weight of 100 seeds)×100. Three
640 biological replicates were analyzed for each genotype.

641 **Fe reductase activity assay**

642 Fe reductase activity was measured using a modified protocol based (Gratz et al.,
643 2019). Ten-day-old Arabidopsis thaliana seedlings grown under Fe-sufficient or Fe-
644 deficient conditions were used. For each replicate, roots from five plants were rinsed
645 with 100 mM $Ca(NO_3)_2$ and transferred into 1.5 ml of assay buffer containing 100 μM
646 FeNaEDTA and 300 μM ferrozine. The samples were incubated for 3 h in the dark.
647 Formation of the Fe(II)–ferrozine complex was quantified by measuring absorbance at
648 562 nm using an Infinite 200 PRO plate reader (Tecan). Enzyme activity was
649 calculated using the ferrozine extinction coefficient (ε = 28.6 mM^{-1} cm^{-1}) and
650 normalized to total root length. Each assay included at least three biological replicates.

651 **Plant Protein Extraction and Immunoblotting**

652 Total proteins were extracted from roots of Arabidopsis thaliana seedlings. Root
653 tissues were dried, weighed, frozen in liquid nitrogen, and ground using a Precellys
654 homogenizer (three cycles at 6500 rpm). Proteins were solubilized in 2× SDG buffer
655 (125 mM Tris-HCl, pH 6.8, 5% SDS, 4% DTT, 20% glycerol, 0.02% bromophenol blue)
656 at a ratio of 10 μl buffer per 5 mg tissue. After rotation for 10 minutes and centrifugation
657 (13,000 rpm, 10 minutes, 4°C), supernatants were collected and boiled at 60°C for 10
658 minutes.

659 Proteins were separated by SDS-PAGE using 4–20% Mini-PROTEAN TGX Stain-Free
660 gels (Bio-Rad) and transferred to 0.45 μm nitrocellulose membranes (Bio-Rad) with
661 the Trans-Blot Turbo Transfer System (Bio-Rad). Gels were imaged before transfer
662 using the ChemiDoc MP Imaging System (Bio-Rad).

663 Membranes were blocked for 5 minutes in EveryBlot Blocking Buffer (Bio-Rad) and
664 incubated for 1 hour at room temperature with primary antibodies against mTurquoise2
665 (Biozol, NBS-ASJ-L9MMEL-60; 1:1000 dilution) or Actin (Agrisera, A0480; 1:5000
666 dilution) in 2.5% TBST with blocking buffer. After three washes in 1× TBST,
667 membranes were incubated with HRP-conjugated secondary antibodies (mouse anti-
668 goat for mTurquoise2 [Invitrogen, G-21040; 1:1000 dilution] and anti-mouse for Actin
669 [Jackson ImmunoResearch; 1:10,000 dilution in TBST with 5% milk]) for 1 hour.
670 Chemiluminescent signals were developed with ECL substrate (Amersham ECL
671 Select or SuperSignal West Femto) and imaged using the ChemiDoc MP Imaging
672 System.

673 To assess the effect of proteasome inhibition on bHLH104 protein stability, 10-day-old
674 Arabidopsis seedlings were transferred to liquid Hoagland medium and incubated for
675 18 hours in a plant growth chamber under the same growth conditions described
676 above. Seedlings were treated with either 50 μM MG132 or an equal volume of DMSO
677 (control). After treatment, total protein from roots was extracted and analyzed by
678 immunoblotting. Band intensities were quantified using Biorad-Image Lab™ Software,
679 and normalized to total protein staining. For each genotype, three independent
680 biological replicates were used. Relative protein abundance was calculated as the
681 ratio of normalized band intensity in MG132-treated versus DMSO-treated samples
682 (MG132/DMSO), representing the fold increase in bHLH104 accumulation upon
683 proteasome inhibition.

684 **Cell-Free Protein Degradation Assay**

685 The coding sequence of bHLH104 was cloned into an expression vector containing an
686 N-terminal His tag and transformed into Escherichia coli Rosetta (DE3) cells. Single
687 colonies were cultured overnight in LB medium with ampicillin, and secondary cultures
688 were inoculated at 1% volume, grown at 37°C to OD_{600} = 0.6–0.8, and induced with 1
689 mM IPTG at 28°C for 10–12 hours. Cells were harvested by centrifugation and stored
690 at –70°C.

691 For purification, frozen cell pellets were thawed on ice, resuspended in lysis buffer (30
692 mM Tris-HCl, pH 8.0, 150 mM NaCl) supplemented with protease inhibitors (Roche),
693 and sonicated. Lysates were clarified by centrifugation (14,000 rpm, 30 minutes, 4°C),
694 and His-tagged bHLH104 protein was purified using a Ni-NTA column (Cytiva) on a

695 Bio-Rad NGC chromatography system. Bound proteins were batch-eluted with 250
696 mM imidazole in lysis buffer, and fractions containing the target protein were pooled,
697 concentrated using Amicon centrifugal filters, and quantified using absorbance at 280
698 nm with a NanoQuant plate (Tecan). Protein concentrations were calculated using the
699 molar extinction coefficient predicted by ExPASy ProtParam, and proteins were
700 aliquoted and stored at –70°C.

701 We followed protocol from Wang et al., 2009, for cell-free degradation assay. Col-0
702 seedlings were grown for 10 days on Fe-deficient MS agar plates. Approximately 500
703 mg of root tissue was flash-frozen, ground using a Precellys homogenizer (6500 rpm,
704 three cycles of 20 seconds), and extracted in 500 µl degradation buffer (25 mM Tris-
705 HCl pH 7.5, 10 mM NaCl, 10 mM $MgCl_2$, 4 mM PMSF, 5 mM DTT, 10 mM ATP).
706 Extracts were clarified by centrifugation (15,000 rpm, 15 minutes, 4°C).

707 Degradation reactions were initiated by incubating 50 µl of plant extract with purified
708 His-bHLH104 protein at 22°C. Protein extracts were treated with either 160 µM MG132
709 or an equal volume of DMSO (control). Reactions were stopped at indicated time
710 points by adding SDS loading buffer and boiling at 95°C for 10 minutes. Proteins were
711 separated by SDS-PAGE, transferred to nitrocellulose membranes, and detected by
712 immunoblotting using an HRP-conjugated anti-His antibody (Thermo Fisher Scientific,
713 MA1-21315-HRP).

714 **Confocal Microscopy**

715 Confocal imaging was performed using a Zeiss LSM 880 laser-scanning confocal
716 microscope equipped with a 40× C-Apochromat water immersion objective. Two-day-
717 old Arabidopsis thaliana seedlings grown under Fe-sufficient (+Fe) conditions were
718 used for imaging. Excitation of mTurquoise2 fluorescence was carried out using a 458
719 nm laser line, and emitted fluorescence was collected between 493 nm and 613 nm.
720 Images were processed and analyzed using the manufacturer's software ZEN lite
721 (Zeiss).

722 **ICP-MS Analysis**

723 Tissue collection for inductively coupled plasma mass spectrometry (ICP-MS) was
724 performed with separate ceramic tools for Fe-sufficient and Fe-deficient samples to
725 prevent metal contamination. Roots, young leaves, and old leaves from hydroponically

726 grown plants, and shoots and roots from plate-grown seedlings, were harvested as
727 pooled biological replicates (three replicates per line and condition). Tissues were
728 washed sequentially in Tris-EDTA buffer and deionized water, dried on tissue paper,
729 transferred into pre-weighed 5-ml Falcon tubes, and oven-dried at 65°C for up to two
730 weeks.

731 Dry weights were recorded, and tissue digestion was performed with 67% nitric acid
732 (ICP-MS grade) at volumes adjusted to sample mass (1 ml for 20–35 mg, 500 µl for
733 10–20 mg, 350 µl for <10 mg). Samples were incubated at room temperature overnight
734 and then heated at 95°C until clear. After centrifugation (4000 rpm, 30 minutes, 4°C),
735 supernatants were diluted with deionized water to maintain a final acid concentration
736 below 5% (v/v). Dilution factors were calculated based on sample weight.

737 ICP-MS measurements were corrected for background signal and normalized by
738 sample dilution factors. Statistical analysis was performed in R using two-way ANOVA
739 followed by Tukey's post hoc test ($p < 0.05$), and data were visualized using
740 ggPlantmap scripts as described in (Jo and Kajala, 2024).

741 **RNA Isolation and RT-qPCR Analysis**

742 Total RNA was extracted from roots and shoots of 10-day-old seedlings and from roots,
743 young leaves, and old leaves of 30-day-old hydroponically grown plants using the
744 RNeasy Plant Mini Kit (Qiagen) with on-column DNase digestion. Tissues were
745 homogenized under liquid nitrogen with a Heidolph RZR 2020 and Precellys 24
746 homogenizer. RNA quality and concentration were assessed by absorbance (260/280
747 nm) using a TECAN Infinite M200 PRO plate reader; samples with ratios between 2.1
748 and 2.25 and concentrations >90 ng/µl were used.

749 First-strand cDNA synthesis was performed with the RevertAid Reverse Transcriptase
750 kit (Thermo Fisher Scientific) using 300–500 ng RNA per reaction. RNA was treated
751 with DNase I, followed by heat inactivation with EDTA and oligo$(dT)_{18}$ primer
752 annealing. Reverse transcription was carried out at 42°C for 1 hour. cDNA was diluted
753 1:10 and 1:100 for downstream applications and stored at –20°C.

754 Quantitative PCR (qPCR) was performed using SYBR Green chemistry (Bio-Rad) in
755 a CFX Opus 384 Real-Time PCR System (Bio-Rad) and according to protocol in (Ngigi
756 and Bauer, 2023). Each sample was measured in technical duplicates alongside a six-

757 point standard curve (10^7–10^2 copies) for each gene. The PCR program included an
758 initial denaturation (95°C, 3 min) followed by 40 cycles of 95°C denaturation (10 sec),
759 annealing at gene-specific temperature (15 sec), and extension (5 sec). Melt curve
760 analysis was conducted from 65°C to 95°C.

761 Starting quantities (SQ) were calculated from the standard curves, and data were
762 normalized in a two-step procedure: first by correcting gene of interest SQ values
763 using EFg normalization (to correct residual genomic DNA), and second by adjusting
764 across samples using an EFc coefficient to ensure cross-tissue comparability.
765 Negative normalized values were adjusted to zero. Normalized expression values
766 were visualized as z-score heatmaps using R.

767 **RNA Sequencing and analysis**

768 RNA sequencing (RNA-seq) was performed by BMKGENE (Biomarker Technologies).
769 Library preparation and sequencing were conducted according to the service
770 provider's standard protocols. Briefly, mRNA was enriched using poly-A selection,
771 fragmented, and reverse transcribed to generate cDNA libraries. Libraries were
772 sequenced on the Illumina NovaSeq platform, generating 150 bp paired-end reads.
773 Data was processed following protocol in (Mai, 2024).

774 RNA-seq matrices were analyzed in R (v4.3+) with limma (v3.58+) using the limma-
775 trend workflow appropriate for TPM/CPM-like data. Expression values were log2-
776 transformed as log2(x + 0.5). For each comparison (line vs WT), linear models were
777 fit with empirical Bayes moderation, and contrasts were estimated to obtain log2 fold-
778 changes (log2FC) and BH-adjusted P values. Genes were called differentially
779 expressed if FDR ≤ 0.05 and |log2FC| ≥ 0.58 (~1.5-fold). Direction (up/down) was
780 assigned by the sign of log2FC; the resulting DEG_significant tables were used for
781 enrichment and count summaries.

782 RNA-seq data will be made available in a public database upon acceptance.

783 **Gene Ontology enrichment**

784 GO Biological Process enrichment was performed with clusterProfiler (v4.10+) against
785 the appropriate org.*.eg.db annotation. Up- and down-regulated DEG sets were tested
786 separately. The gene universe for each test comprised all genes assessed in the
787 corresponding comparison. Over-representation p values were computed by the

788 hypergeometric test and adjusted by Benjamini–Hochberg; terms with FDR ≤ 0.05
789 were considered significant. When indicated, redundant terms were condensed with
790 simplify() (Wang similarity; cutoff = 0.7), retaining the most significant representative

791 **Structural Predictions and Visualization**

792 Protein structures for bHLH104, BTS and its interaction interfaces were predicted
793 using AlphaFold Multimer (Evans et al., 2021; Jumper et al., 2021) to model the full-
794 length and interacting protein complexes. The protein sequences of bHLH104 and its
795 interacting partner, BTS were input into AlphaFold Multimer to generate accurate
796 structural models of their interactions. The models were assessed for confidence using
797 the predicted Local Distance Difference Test (pLDDT) and analyzed for structural
798 integrity.

799 The resulting structures were visualized and analyzed using UCSF ChimeraX
800 (Pettersen et al., 2004). ChimeraX was used for detailed structural analysis, including
801 the electrostatic surface modeling to visualize potential protein-protein interaction
802 interfaces. Electrostatic potentials were calculated based on the predicted protein
803 structures, and interaction hotspots were identified by analyzing the electrostatic
804 properties of the interface regions.

805 **Yeast Two-Hybrid Assay**

806 Yeast two-hybrid assays were performed as described by (Gietz and Schiestl, 2007)
807 with modifications. C-terminal fragments of bHLH104 and bHLH104^dPAA were
808 cloned into the Gateway-compatible yeast vectors pACT2-GW (activation domain
809 fusion, AD) and pGBKT7-GW (DNA-binding domain fusion, BD). Primers used are
810 listed in Supplementary Table 1. Full-length BTS, BTSL1, and BTSL2 constructs were
811 obtained from (Lichtblau et al., 2022). All protein pairs were assayed in reciprocal
812 combinations (AD–X with BD–Y and BD–X with AD–Y), and empty vector controls
813 were included.

814 Yeast strain AH109 was co-transformed with plasmid pairs using the lithium acetate
815 (LiAc) method and selected on synthetic dropout (SD) medium lacking leucine and
816 tryptophan (SD–Leu–Trp). Colonies were cultured overnight in liquid SD–Leu–Trp
817 medium, adjusted to an OD_{600} of 1.0, and spotted (10 µl) in tenfold dilution series onto
818 SD medium lacking leucine, tryptophan, and histidine (SD–Leu–Trp–His). To suppress

819 autoactivation, SD–Leu–Trp–His plates supplemented with 15 mM 3-amino-1,2,4-
820 triazole (3-AT) were used specifically for assays involving BD–BTSL2. Plates were
821 incubated at 30°C, and growth was monitored for up to 14 days.

822 **UbiGate Assay**

823 Ubiquitination assays were performed using the UbiGate system as described
824 previously (Kowarschik et al., 2018; Ortmann et al., 2023) with adaptations for
825 bHLH104 substrates. The coding sequences of codon optimized bHLH104 and
826 bHLH104^dPAA were cloned into the pGG-TP1 vector (6×HA–TwinStrepII backbone)
827 by GoldenGate assembly. Complete ubiquitination modules were assembled into the
828 pGG-pET28 destination vector and included 6×His-tagged ubiquitin (pGG-TP2), E1
829 enzyme (UBA1, pGG-P3), E2 conjugating enzyme (GST–UBC8, pUG-TP4), and a
830 truncated BTS E3 ligase (BTS-HC, pGG-TP5), using the linker plasmid pICH41800.
831 Primers used are listed in Supplementary Table 1.

832 For each E3-substrate combination, full ubiquitination constructs and substrate-minus,
833 E2-minus, and E3-minus control constructs were generated. Constructs were
834 transformed into Escherichia coli Rosetta (DE3) and expressed by induction with 1
835 mM IPTG and 3% ethanol at 28°C for 3 hours. Cells were harvested by centrifugation
836 and stored at –80°C.

837 For protein extraction, bacterial pellets were resuspended in phosphate-buffered
838 saline (PBS) to OD_{600} = 13, treated with lysozyme (10 mg/mL), subjected to four
839 freeze-thaw cycles, and digested with RNase A and DNase I (1 mg/mL each). Lysates
840 were mixed with 2× Laemmli sample buffer and boiled at 95°C for 10 minutes.

841 Proteins were separated by SDS-PAGE using TGX precast gels (Bio-Rad) and
842 transferred to 0.2 µm nitrocellulose membranes with the Trans-Blot Turbo system (Bio-
843 Rad). Membranes were blocked with 5% (w/v) non-fat dry milk in TBST and probed
844 with the following primary antibodies: HRP-conjugated anti-Myc (Thermo Fisher
845 Scientific, R951-25-HRP), anti-GST (clone 8-326, Thermo Fisher Scientific) followed
846 by HRP-conjugated secondary antibody (Jackson ImmunoResearch), HRP-
847 conjugated Strep-Tactin (Fisher Scientific), and HRP-conjugated anti-6×His (Thermo
848 Fisher Scientific, MA1-21315-HRP). Signals were detected using the Amersham ECL
849 Prime kit (Cytiva) and visualized with the ChemiDoc MP Imaging System (Bio-Rad).

Statistical Analysis and Data Visualization

All statistical analyses and data visualization were performed using RStudio (version 2025.04.1). Phenotyping data were visualized using ggplot2, where violin plots with overlaid box plots were generated to compare data distributions across genotypes and experimental conditions. Gene expression data were Z-score normalized using the scale() function in R, and gene expression heatmaps were created using the pheatmap package to visualize normalized expression levels across tissues and experimental conditions. For ICP-MS data visualization, the ggPlantMap package (Jo and Kajala, 2024) was used.

Statistical comparisons were performed using two-way ANOVA followed by Tukey's Honest Significant Difference (HSD) test for multiple comparisons. A p-value threshold of 0.05 was considered significant.

Acknowledgements

We thank Elke Wieneke for excellent technical assistance. The authors thank the Biocenter-MS Platform, Sabine Ambrosius and Sabine Metzger, University of Cologne, for conducting and providing support in the ICP-MS measurements. The authors thank Center for Advanced Imaging (CAi) at Heinrich Heine University for providing advanced imaging facility. DB and VV were members of the international graduate school iGRAD-Plant, Düsseldorf (the DFG International Research Training group 2466). Chat GPT 4.0 has been used to edit and shorten text, and correct and improve language.

Author contributions

DB and PB planned and designed the research. DB, SW, MK, and VV performed the experiments and analyzed the data. DB wrote the manuscript. JLE generated and provided materials. DB and PB supervised the research. PB acquired funding and agreed to serve as the author responsible for contact and ensures communication. All authors read, commented and approved the submitted version.

Funding

This project was funded by the Deutsche Forschungsgemeinschaft (DFG, German Research Foundation) under Germany´s Excellence Strategy – EXC-2048/1 – project ID 390686111. This project received funding through the DFG International Research

881 Training group 2466 (GRK F020512056 (NextPlant)). Funded by the Deutsche
882 Forschungsgemeinschaft (DFG) – TRR 341/1 – 456082119.

883 ## References

884 **Abuzeineh A, Vert G, Zelazny E** (2022) Birth, life and death of the Arabidopsis IRT1 iron transporter:
885 the role of close friends and foes. Planta **256**: 112

886 **Aparicio F, Pallás V** (2017) The coat protein of *Alfalfa mosaic virus* interacts and interferes with the
887 transcriptional activity of the bHLH transcription factor ILR3 promoting salicylic acid-
888 dependent defence signalling response. Mol Plant Pathol **18**: 173–186

889 **Arend D, Lange M, Pape J-M, Weigelt-Fischer K, Arana-Ceballos F, Mücke I, Klukas C, Altmann T,**
890 **Scholz U, Junker A** (2016) Quantitative monitoring of Arabidopsis thaliana growth and
891 development using high-throughput plant phenotyping. Sci Data **3**: 160055

892 **Briat J-F, Curie C, Gaymard F** (2007) Iron utilization and metabolism in plants. Curr Opin Plant Biol **10**:
893 276–282

894 **Cailliatte R, Schikora A, Briat J-F, Mari S, Curie C** (2010) High-Affinity Manganese Uptake by the
895 Metal Transporter NRAMP1 Is Essential for *Arabidopsis* Growth in Low Manganese
896 Conditions. Plant Cell **22**: 904–917

897 **Chen Y-Y, Wang Y, Shin L-J, Wu J-F, Shanmugam V, Tsednee M, Lo J-C, Chen C-C, Wu S-H, Yeh K-C**
898 (2013) Iron Is Involved in the Maintenance of Circadian Period Length in Arabidopsis. Plant
899 Physiol **161**: 1409–1420

900 **Cheng H, Qin L, Lee S, Fu X, Richards DE, Cao D, Luo D, Harberd NP, Peng J** (2004) Gibberellin
901 regulates *Arabidopsis* floral development via suppression of DELLA protein function.
902 Development **131**: 1055–1064

903 **Clough SJ, Bent AF** (1998) Floral dip: a simplified method for Agrobacterium-mediated
904 transformation of Arabidopsis thaliana. Plant J **16**: 735–743

905 **Connolly EL, Fett JP, Guerinot ML** (2002) Expression of the IRT1 Metal Transporter Is Controlled by
906 Metals at the Levels of Transcript and Protein Accumulation. Plant Cell **14**: 1347–1357

907 **Dubeaux G, Neveu J, Zelazny E, Vert G** (2018) Metal Sensing by the IRT1 Transporter-Receptor
908 Orchestrates Its Own Degradation and Plant Metal Nutrition. Mol Cell **69**: 953-964.e5

Dutta A, Choudhary P, Caruana J, Raina R (2017) JMJ 27, an Arabidopsis H3K9 histone demethylase, modulates defense against *Pseudomonas syringae* and flowering time. Plant J **91**: 1015–1028

Evans R, O'Neill M, Pritzel A, Antropova N, Senior A, Green T, Žídek A, Bates R, Blackwell S, Yim J (2021) Protein complex prediction with AlphaFold-Multimer. biorxiv 2021.10. 04.463034

Gelvin SB (2003) *Agrobacterium* -Mediated Plant Transformation: the Biology behind the "Gene-Jockeying" Tool. Microbiol Mol Biol Rev **67**: 16–37

Gietz RD, Schiestl RH (2007) Large-scale high-efficiency yeast transformation using the LiAc/SS carrier DNA/PEG method. Nat Protoc **2**: 38–41

Gratz R, Manishankar P, Ivanov R, Köster P, Mohr I, Trofimov K, Steinhorst L, Meiser J, Meiser J, Mai H-J, et al (2019) CIPK11-Dependent Phosphorylation Modulates FIT Activity to Promote Arabidopsis Iron Acquisition in Response to Calcium Signaling. Dev Cell. doi: 10.1016/j.devcel.2019.01.006

Hindt MN, Akmakjian GZ, Pivarski KL, Punshon T, Baxter I, Salt DE, Guerinot ML (2017) BRUTUS and its paralogs, BTS LIKE1 and BTS LIKE2, encode important negative regulators of the iron deficiency response in Arabidopsis thaliana. Metallomics. doi: 10.1039/c7mt00152e

Hong S-Y, Seo PJ, Ryu JY, Cho S-H, Woo J-C, Park C-M (2013) A Competitive Peptide Inhibitor KIDARI Negatively Regulates HFR1 by Forming Nonfunctional Heterodimers in Arabidopsis Photomorphogenesis. Mol Cells **35**: 25–31

Hüther P, Schandry N, Jandrasits K, Bezrukov I, Becker C (2020) ARADEEPOPSIS, an Automated Workflow for Top-View Plant Phenomics using Semantic Segmentation of Leaf States. Plant Cell **32**: 3674–3688

Jeong J, Guerinot ML (2009) Homing in on iron homeostasis in plants. Trends Plant Sci **14**: 280–285

Jiang M, Niu Y, Wen G, Zhao C, Gao Q, Li G (2024) Evolutionary studies of the basic helix–loop–helix (bHLH) IVc gene family in plants and the role of *AtILR3* in *Arabidopsis* response to ABA stress. Physiol Plant **176**: e14128

Jo L, Kajala K (2024) ggPlantmap: an open-source R package for the creation of informative and quantitative ggplot maps derived from plant images. J Exp Bot **75**: 5366–5376

Jumper J, Evans R, Pritzel A, Green T, Figurnov M, Ronneberger O, Tunyasuvunakool K, Bates R, Žídek A, Potapenko A (2021) Highly accurate protein structure prediction with AlphaFold. nature **596**: 583–589

Knopf MC, Bauer P (2025) Affordable Non-Invasive Machine-Aided Phenotyping Identifies Phenotypic Variation to Soil Stress Across the *ARABIDOPSIS THALIANA* Life Cycle. Physiol Plant **177**: e70427

Kowarschik K, Hoehenwarter W, Marillonnet S, Trujillo M (2018) UbiGate: a synthetic biology toolbox to analyse ubiquitination. New Phytol **217**: 1749–1763

Lampropoulos A, Sutikovic Z, Wenzl C, Maegele I, Lohmann JU, Forner J (2013) GreenGate-a novel, versatile, and efficient cloning system for plant transgenesis. PloS One **8**: e83043

Lešková A, Giehl RFH, Hartmann A, Fargašová A, Von Wirén N (2017) Heavy Metals Induce Iron Deficiency Responses at Different Hierarchic and Regulatory Levels. Plant Physiol **174**: 1648–1668

Li X, Zhang HM, Ai Q, Liang G, Yu D (2016) Two bHLH Transcription Factors, bHLH34 and bHLH104, Regulate Iron Homeostasis in Arabidopsis thaliana. Plant Physiol. doi: 10.1104/pp.15.01827

Li Y, Li Y, Li Y, Li Y, Lu C, Lu C, Li C, Lei RH, Pu MN, Zhao JH, et al (2021) IRON MAN interacts with BRUTUS to maintain iron homeostasis in Arabidopsis. Proc Natl Acad Sci U S A. doi: 10.1073/pnas.2109063118

Liang G, Zhang H, Li X, Ai Q, Yu D (2017) bHLH transcription factor bHLH115 regulates iron homeostasis in Arabidopsis thaliana. J Exp Bot **68**: 1743–1755

Lichtblau DM, Schwarz B, Baby D, Endres C, Sieberg C, Bauer P (2022) The Iron Deficiency-Regulated Small Protein Effector FEP3/IRON MAN1 Modulates Interaction of BRUTUS-LIKE1 With bHLH Subgroup IVc and POPEYE Transcription Factors. Front Plant Sci **13**: 930049

Long TA, Tsukagoshi H, Busch W, Lahner B, Salt DE, Benfey PN (2010) The bHLH Transcription Factor POPEYE Regulates Response to Iron Deficiency in Arabidopsis Roots. Plant Cell. doi: 10.1105/tpc.110.074096

Mai H-J (2024) PlugNSeq: An Easy, Rapid, and Streamlined mRNA-Seq Data Analysis Pipeline Empowering Insightful Exploration with Well-Annotated Organisms, Requiring Minimal Bioinformatic Expertise v1. doi: 10.17504/protocols.io.4r3l2qjo3l1y/v1

965 **Marschner H** (2012) Marschner's mineral nutrition of higher plants. Academic press

966 **Maruoka T, Gan E-S, Otsuka N, Shirakawa M, Ito T** (2022) Histone Demethylases JMJ30 and JMJ32
967 Modulate the Speed of Vernalization Through the Activation of FLOWERING LOCUS C in
968 Arabidopsis thaliana. Front Plant Sci **13**: 837831

969 **Melnikov S, Mailliot J, Rigger L, Neuner S, Shin B, Yusupova G, Dever TE, Micura R, Yusupov M**
970 (2016) Molecular insights into protein synthesis with proline residues. EMBO Rep **17**: 1776–
971 1784

972 **Naranjo-Arcos MA, Maurer F, Meiser J, Meiser J, Pateyron S, Fink-Straube C, Fink-Straube C, Bauer**
973 **P** (2017) Dissection of iron signaling and iron accumulation by overexpression of subgroup Ib
974 bHLH039 protein. Sci Rep. doi: 10.1038/s41598-017-11171-7

975 **Ngigi M, Khan M, Remus R, Gupta SK, Bauer P** (2025) Age-dependent differential iron deficiency
976 responses of rosette leaves during reproductive stages in *Arabidopsis thaliana*. J Exp Bot
977 eraf207

978 **Ngigi MN, Bauer P** (2023) High-Throughput Plant Gene Expression Analysis by 384-Format Reverse
979 Transcription-Quantitative PCR for Investigating Plant Iron Homeostasis. *In* J Jeong, ed, Plant
980 Iron Homeost. Methods Protoc. Springer US, New York, NY, pp 1–22

981 **Nguyen NT, Khan MA, Castro–Guerrero NA, Chia J-C, Vatamaniuk OK, Mari S, Jurisson SS, Mendoza-**
982 **Cozatl DG** (2022) Iron Availability within the Leaf Vasculature Determines the Magnitude of
983 Iron Deficiency Responses in Source and Sink Tissues in Arabidopsis. Plant Cell Physiol **63**:
984 829–841

985 **Nguyen NT, McInturf SA, Mendoza-Cózatl DG** (2016) Hydroponics: A Versatile System to Study
986 Nutrient Allocation and Plant Responses to Nutrient Availability and Exposure to Toxic
987 Elements. J Vis Exp 54317

988 **Ortmann S, Marx J, Lampe C, Handrick V, Ehnert T-M, Zinecker S, Reimers M, Bonas U, Erickson JL**
989 (2023) A conserved microtubule-binding region in Xanthomonas XopL is indispensable for
990 induced plant cell death reactions. PLoS Pathog **19**: e1011263

991 **Panda SK, Yamamoto YY** (2019) Redox homeostasis in plants: from signalling to stress tolerance.
992 Springer

Pettersen EF, Goddard TD, Huang CC, Couch GS, Greenblatt DM, Meng EC, Ferrin TE (2004) UCSF Chimera—a visualization system for exploratory research and analysis. J Comput Chem **25**: 1605–1612

Pottier M, Dumont J, Masclaux-Daubresse C, Thomine S (2018) Autophagy is essential for optimal translocation of iron to seeds in Arabidopsis. J Exp Bot. doi: 10.1093/jxb/ery388

Pullin J, Rodríguez-Celma J, Franceschetti M, Mundy JEA, Svistunenko DA, Bradley JM, Le Brun NE, Balk J (2025) Iron-sensing and redox properties of the hemerythrin-like domains of Arabidopsis BRUTUS and BRUTUS-LIKE2 proteins. Nat Commun **16**: 3865

Quintana, J., Bernal, M., Scholle, M., Holländer-Czytko, H., Nguyen, N. T., Piotrowski, M., Mendoza-Cózatl, D. G., Haydon, M. J. & Krämer, U. 2022. Root-to-shoot iron partitioning in Arabidopsis requires IRON-REGULATED TRANSPORTER1 (IRT1) protein but not its iron(II) transport function. *Plant J,* **109,** 992-1013.

Rampey RA, Woodward AW, Hobbs BN, Tierney MP, Lahner B, Salt DE, Bartel B (2006) An Arabidopsis Basic Helix-Loop-Helix Leucine Zipper Protein Modulates Metal Homeostasis and Auxin Conjugate Responsiveness. Genetics **174**: 1841–1857

Rodríguez-Celma J, Connorton JM, Kruse I, Green RT, Franceschetti M, Chen Y-T, Cui Y, Ling H-Q, Yeh K-C, Balk J (2019) Arabidopsis BRUTUS-LIKE E3 ligases negatively regulate iron uptake by targeting transcription factor FIT for recycling. Proc Natl Acad Sci U S A. doi: 10.1073/pnas.1907971116

Salomé PA, Oliva M, Weigel D, Krämer U (2012) Circadian clock adjustment to plant iron status depends on chloroplast and phytochrome function. EMBO J **32**: 511–523

Samira R, Li B, Kliebenstein D, Li C, Davis E, Gillikin JW, Long TA (2018) The bHLH transcription factor ILR3 modulates multiple stress responses in Arabidopsis. Plant Mol Biol **97**: 297–309

Schwarz B, Bauer P (2020) FIT, a regulatory hub for iron deficiency and stress signaling in roots, and FIT-dependent and -independent gene signatures. J Exp Bot **71**: 1694–1705

Selote D, Selote D, Samira R, Matthiadis A, Gillikin JW, Long TA (2015) Iron-Binding E3 Ligase Mediates Iron Response in Plants by Targeting Basic Helix-Loop-Helix Transcription Factors. Plant Physiol. doi: 10.1104/pp.114.250837

1021 **Sharma R, Yeh K** (2020) The dual benefit of a dominant mutation in Arabidopsis *IRON DEFICIENCY*
1022 *TOLERANT1* for iron biofortification and heavy metal phytoremediation. Plant Biotechnol J
1023 **18**: 1200–1210

1024 **Shen C, Yang Y, Liu K, Zhang L, Guo H, Sun T, Wang H** (2016) Involvement of endogenous salicylic
1025 acid in iron-deficiency responses in Arabidopsis. J Exp Bot **67**: 4179–4193

1026 **Vert G, Grotz N, Dédaldéchamp F, Gaymard F, Guerinot ML, Briat J-F, Curie C** (2002) IRT1, an
1027 Arabidopsis Transporter Essential for Iron Uptake from the Soil and for Plant Growth. Plant
1028 Cell **14**: 1223–1233

1029 **Wang F, Zhu D, Huang X, Li S, Gong Y, Yao Q, Fu X, Fan L-M, Deng XW** (2009) Biochemical Insights on
1030 Degradation of *Arabidopsis* DELLA Proteins Gained From a Cell-Free Assay System. Plant Cell
1031 **21**: 2378–2390

1032 **Waters BM, Grusak MA** (2008) Whole-plant mineral partitioning throughout the life cycle in
1033 *Arabidopsis thaliana* ecotypes Columbia, Landsberg *erecta* , Cape Verde Islands, and the
1034 mutant line *ysl1ysl3*. New Phytol **177**: 389–405

1035 **Wild M, Davière J-M, Regnault T, Sakvarelidze-Achard L, Carrera E, Lopez Diaz I, Cayrel A, Dubeaux**
1036 **G, Vert G, Achard P** (2016) Tissue-Specific Regulation of Gibberellin Signaling Fine-Tunes
1037 Arabidopsis Iron-Deficiency Responses. Dev Cell **37**: 190–200

1038 **Xing Y, Xu N, Bhandari DD, Lapin D, Sun X, Luo X, Wang Y, Cao J, Wang H, Coaker G, et al** (2021)
1039 Bacterial effector targeting of a plant iron sensor facilitates iron acquisition and pathogen
1040 colonization. Plant Cell **33**: 2015–2031

1041 **Yi Y, Guerinot ML** (1996) Genetic evidence that induction of root Fe(III) chelate reductase activity is
1042 necessary for iron uptake under iron deficiency[†]. Plant J **10**: 835–844

1043 **Zhang J, Zhang J, Liu B, Li M, Feng D, Jin H, Wang P, Liu J, Liu J, Liu J, et al** (2015) The bHLH
1044 Transcription Factor bHLH104 Interacts with IAA-LEUCINE RESISTANT3 and Modulates Iron
1045 Homeostasis in Arabidopsis. Plant Cell. doi: 10.1105/tpc.114.132704

1046 **Zhao Q, Ren Y-R, Wang Q-J, Wang X-F, You C-X, Hao Y-J** (2016) Ubiquitination-Related MdBT Scaffold
1047 Proteins Target a bHLH Transcription Factor for Iron Homeostasis. Plant Physiol **172**: 1973–
1048 1988

1049

Figure 1

PAA sequence in bHLH104 enables E3 ligase interaction and degradation

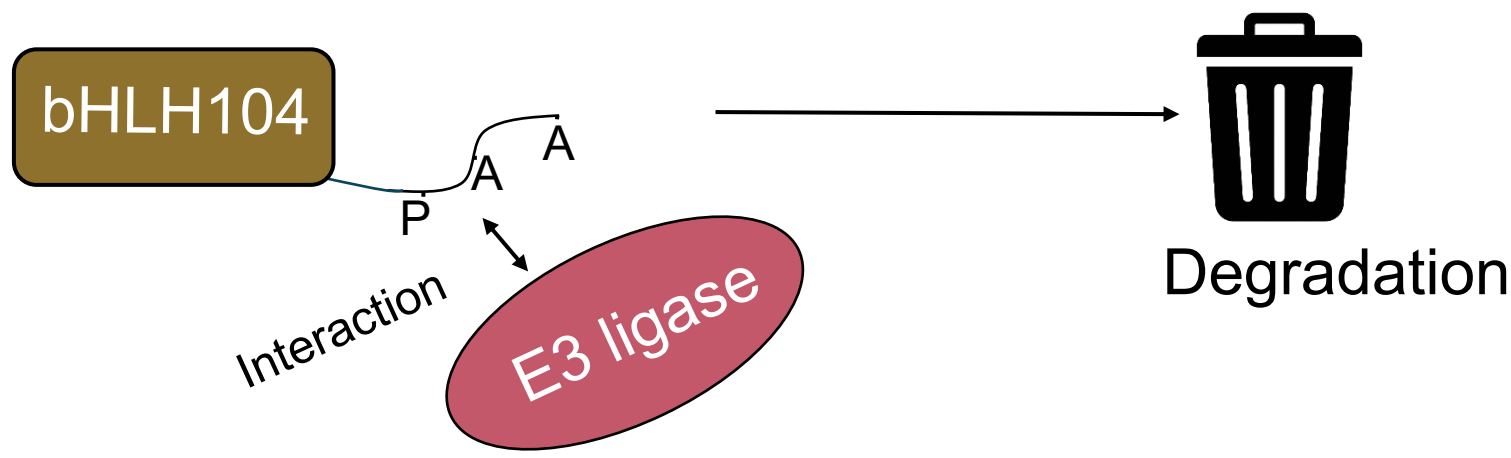

Figure 1. Conceptual model of bHLH104 regulation by its conserved PAA sequence.
In the full-length bHLH104 protein, the PAA sequence forms the interaction interface with an E3 ligase, likely enabling ubiquitination and proteasomal degradation of bHLH104.

Figure 2

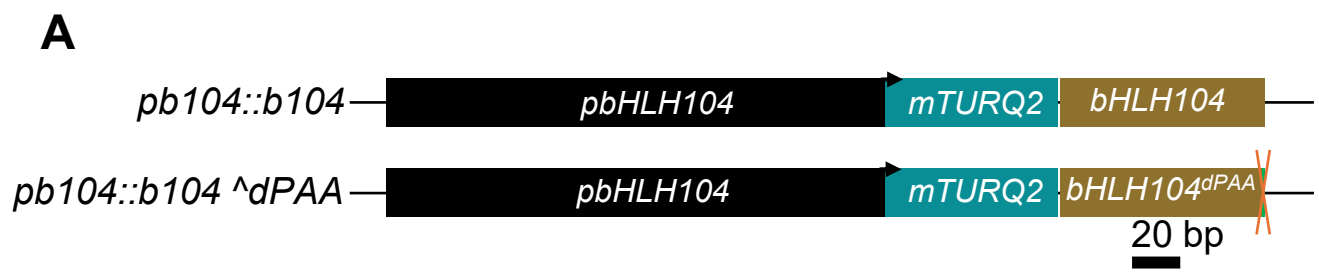
A
pb104::b104
pbHLH104
mTURQ2
bHLH104
pb104::b104 ^dPAA
pbHLH104
mTURQ2
bHLH104dPAA
20 bp

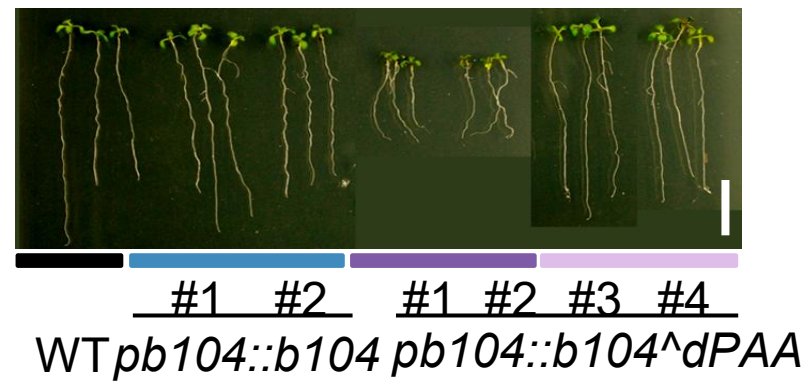
B
#1 #2 #1 #2 #3 #4
WT pb104::b104 pb104::b104^dPAA

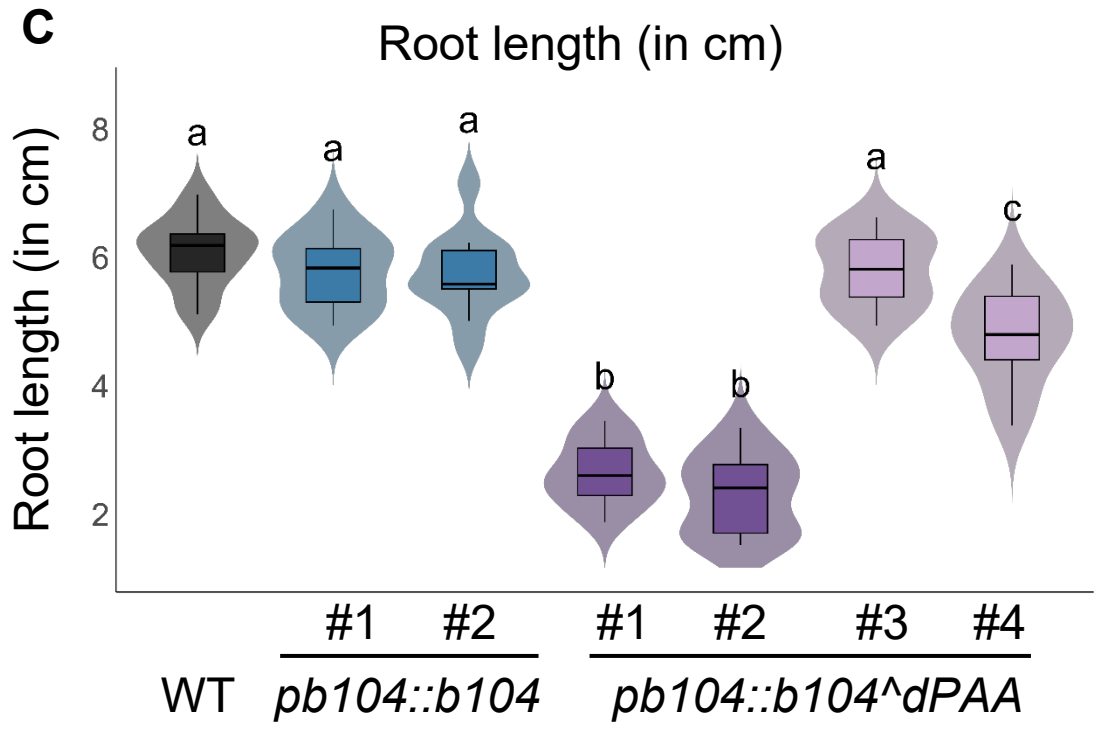
C
Root length (in cm)
Root length (in cm)
8
6
4
2
a a a b b a c
#1 #2 #1 #2 #3 #4
WT pb104::b104 pb104::b104^dPAA

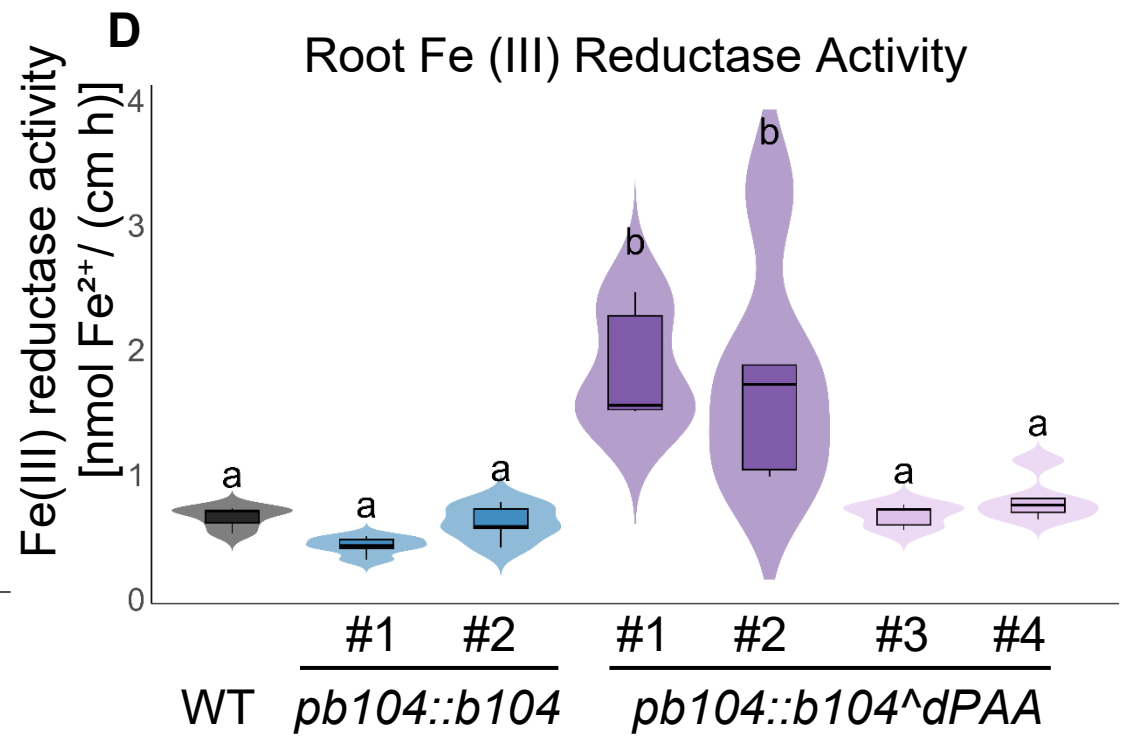
D
Root Fe (III) Reductase Activity
Fe(III) reductase activity
[nmol Fe2+ / (cm h)]
4
3
2
1
0
a a a b b a a
#1 #2 #1 #2 #3 #4
WT pb104::b104 pb104::b104^dPAA

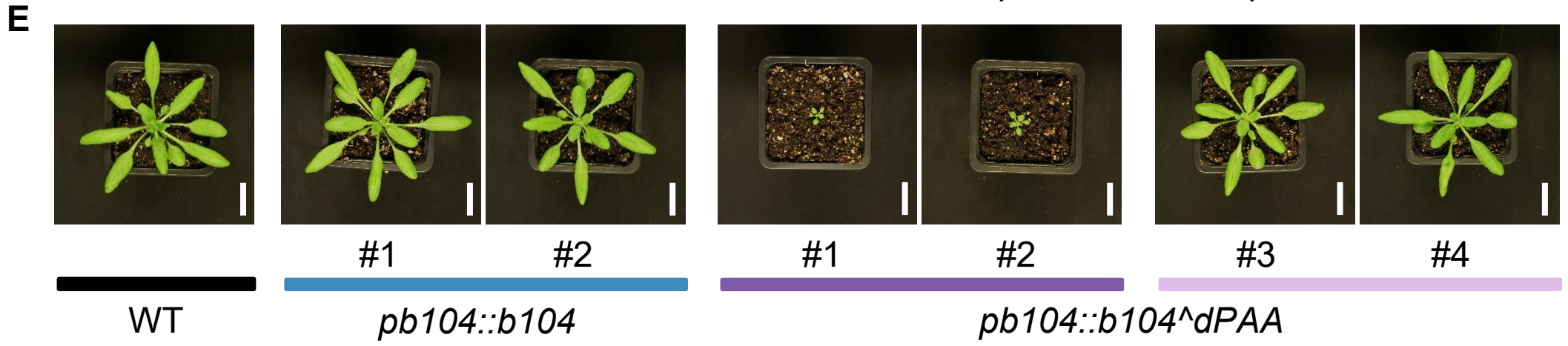
E
#1 #2 #1 #2 #3 #4
WT pb104::b104 pb104::b104^dPAA

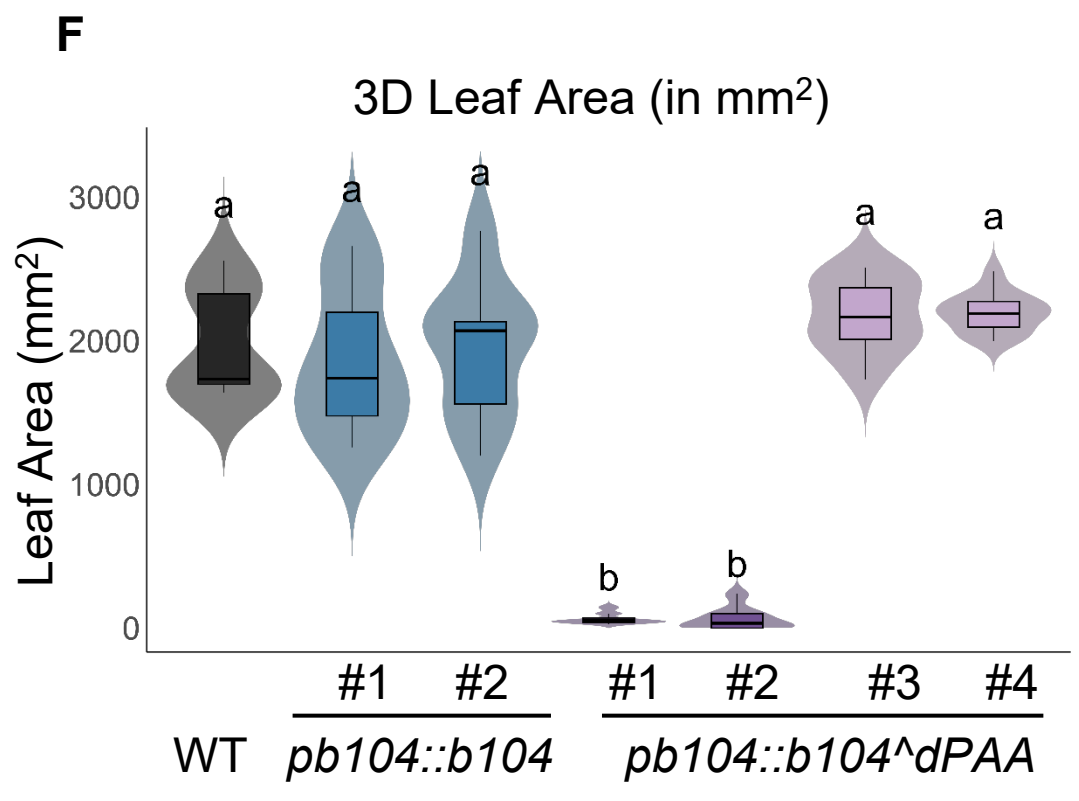
F
3D Leaf Area (in mm2)
Leaf Area (mm2)
3000
2000
1000
0
a a a b b a a
#1 #2 #1 #2 #3 #4
WT pb104::b104 pb104::b104^dPAA

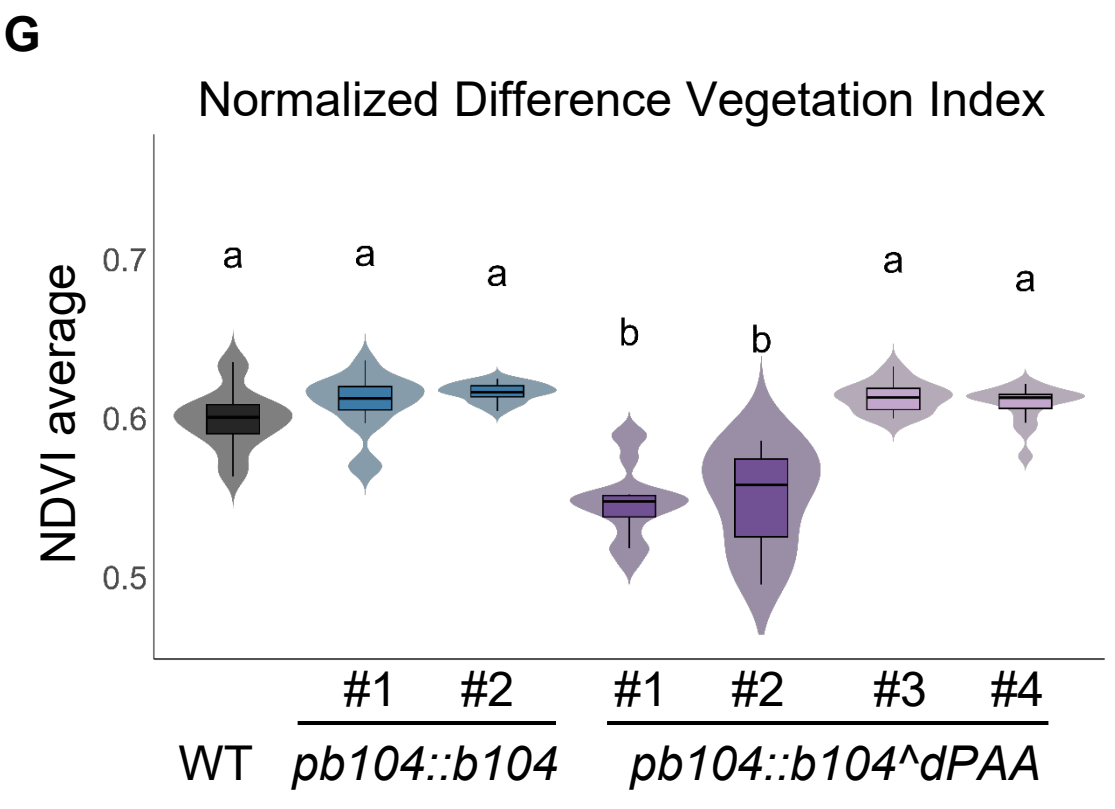
G
Normalized Difference Vegetation Index
NDVI average
0.7
0.6
0.5
a a a b b a a
#1 #2 #1 #2 #3 #4
WT pb104::b104 pb104::b104^dPAA

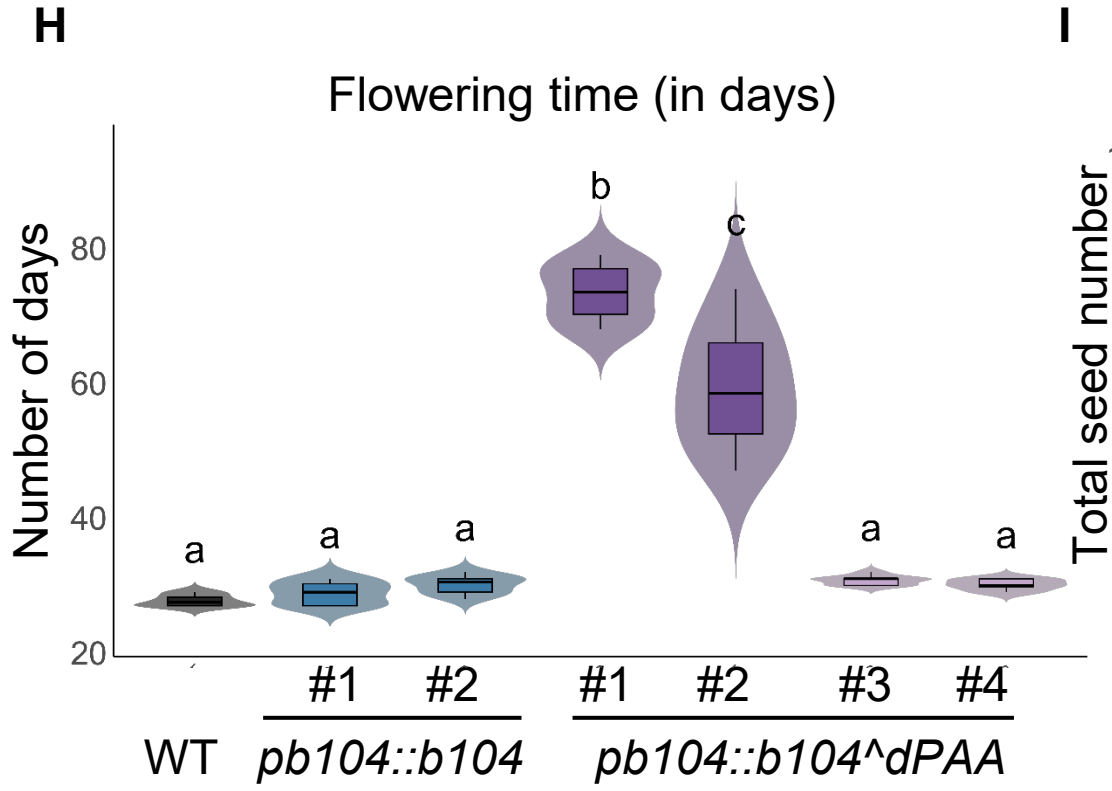
H
Flowering time (in days)
Number of days
80
60
40
20
a a a b c a a
#1 #2 #1 #2 #3 #4
WT pb104::b104 pb104::b104^dPAA

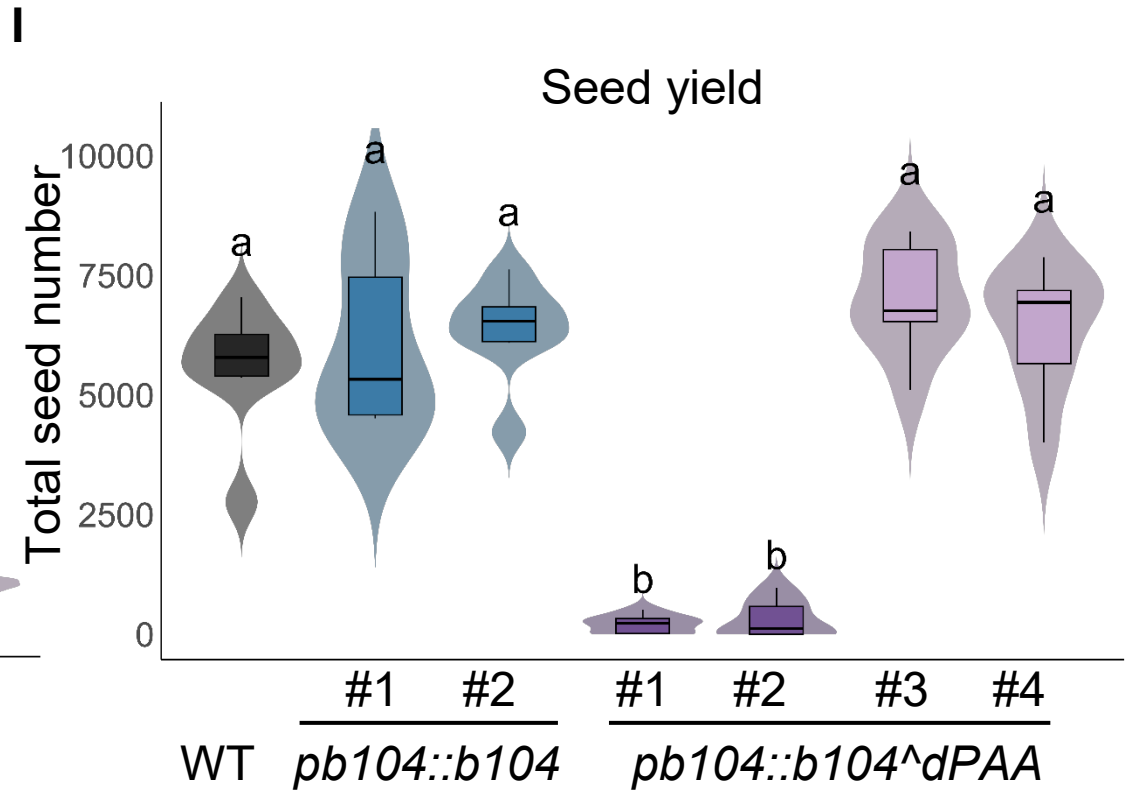
I
Seed yield
Total seed number
10000
7500
5000
2500
0
a a a b b a a
#1 #2 #1 #2 #3 #4
WT pb104::b104 pb104::b104^dPAA

Figure 2. Transgenic expression of bHLH104 lacking the PAA sequence leads to growth alterations and physiological changes in Arabidopsis.
((A) Schematic representation of constructs used to generate transgenic lines expressing either full-length bHLH104 (pb104::b104) or a C-terminal deletion variant lacking the conserved three–amino acid PAA sequence (pb104::b104^dPAA). Both constructs are driven by the native bHLH104 promoter (2,069 bp) and fused at the N-terminus to an mTurquoise2 fluorescent tag. The deleted PAA sequence in b104^dPAA is indicated by a red cross at the C-terminus. Scale bar = 20 bp.
(B) Representative images of 10-day-old seedlings grown on +Fe medium (scale bar = 2 cm).
(C) Primary root length of 12-day-old seedlings grown vertically on Hoagland medium supplemented with Fe.
(D) Fe reductase activity in roots of 10-day-old seedlings grown under +Fe. Activity was quantified spectrophotometrically as Fe(II)–ferrozine complex formation and normalized to total root length.
(E) Representative images of four-week-old soil-grown plants (scale bar = 2 cm). Shown are Col-0 (WT), two independent pb104::b104 lines (#1, #2), and four independent pb104::b104^dPAA lines (#1–4).
(F–G) Quantitative analysis of aboveground phenotypes using the Phenospex PlantEye system: (F) 3D leaf area (mm^2); (G) NDVI (Normalized Difference Vegetation Index)
(H) Flowering time, recorded as days to bolting.
(I) Seed number per plant, estimated from total seed weight based on mean weight per 100 seeds.
Data represent means ± SD (n = 7–12 biological replicates per line). Statistical analysis was performed using two-way ANOVA followed by Tukey's post hoc test. Different letters indicate statistically significant differences at $p < 0.05$.

Figure 3

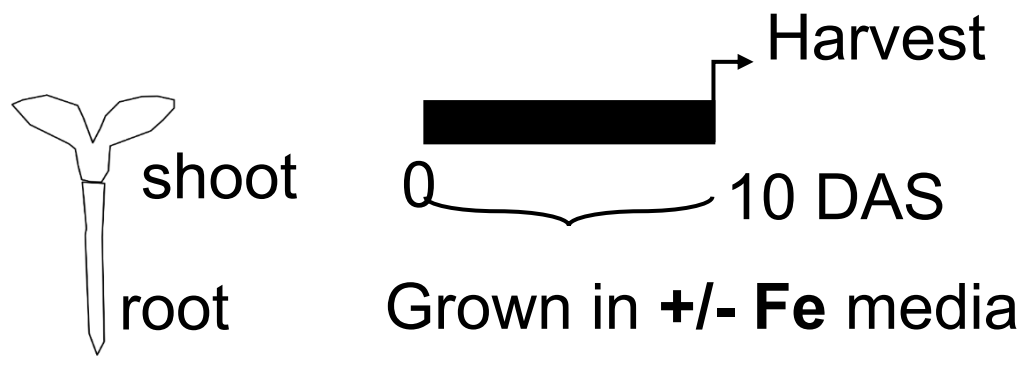

B

L1 - WT
L2 - *pb104::b104 #1*
L3 - *pb104::b104 #2*
L4 - *pb104::b104^dPAA#2*
L5 - *pb104::b104^dPAA#3*
L6 - *pUBQ10::b104#1*
L7 - *pUBQ10::b104#2*

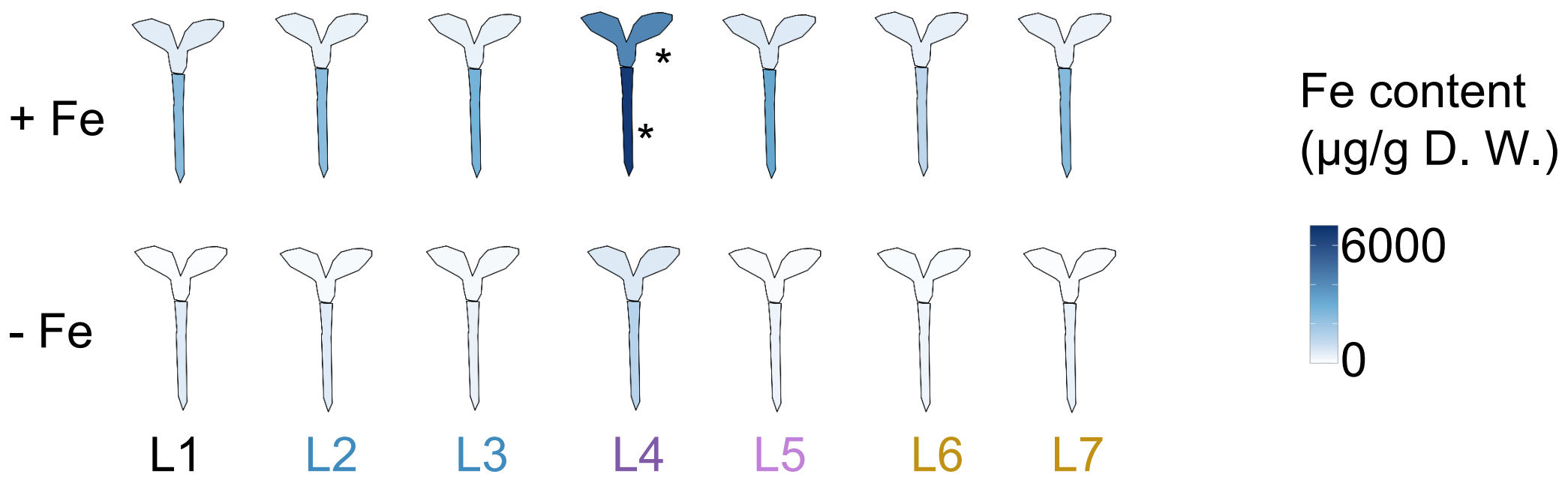

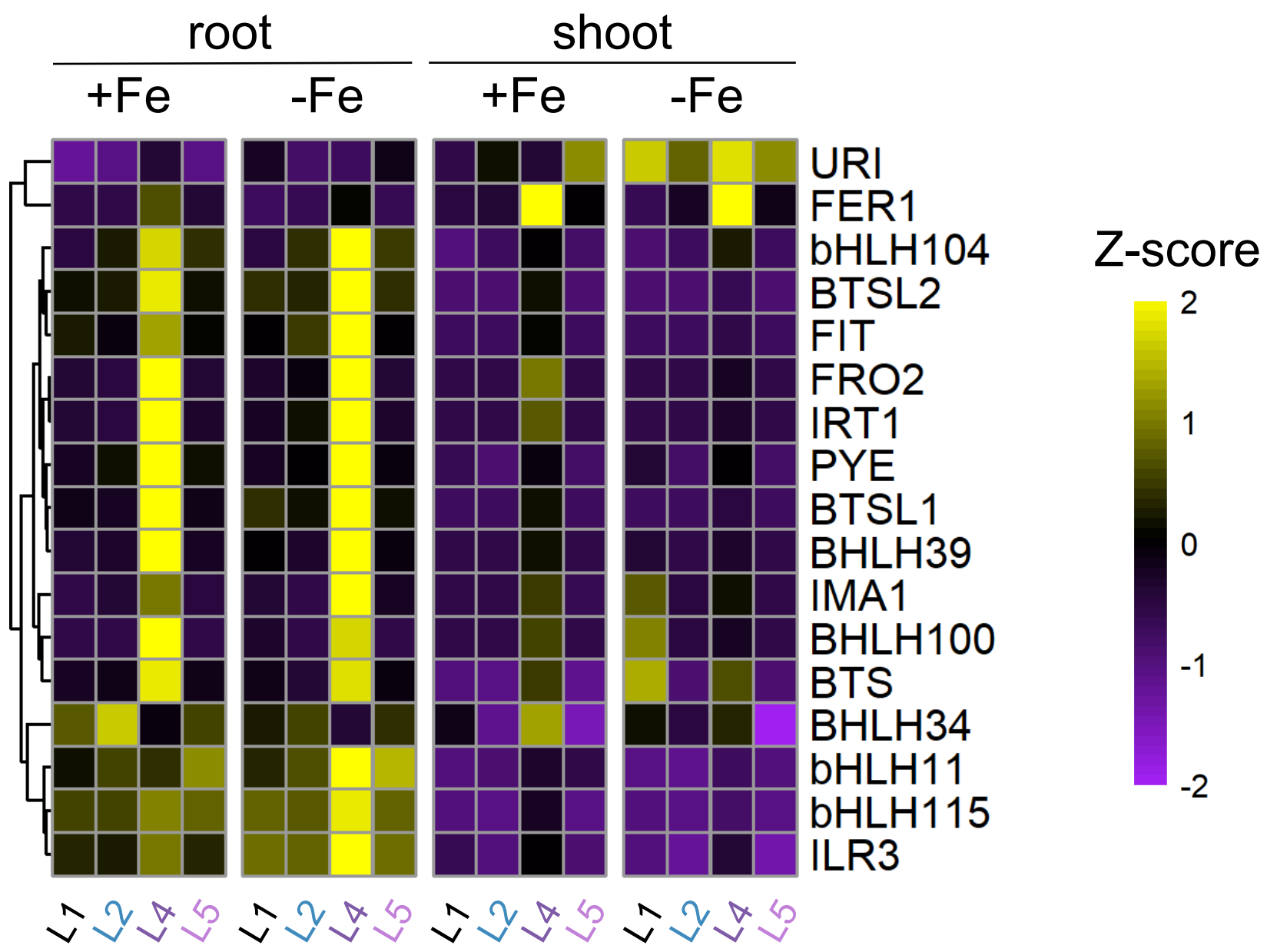

Figure 3. Transgenic lines expressing bHLH104^dPAA exhibit increased iron accumulation and altered iron homeostasis gene expression in seedling stage.
(A) Schematic representation of the experimental design. *Arabidopsis* seedlings were grown for 10 days after sowing (DAS) under either iron-sufficient (+Fe) or iron-deficient (–Fe) conditions. Shoot and root tissues were collected separately for ICP-MS and gene expression analyses. (B) Genotypes used in this study. (C) Iron content in shoot and root tissues of seedlings grown under +Fe and –Fe conditions, measured by ICP-MS. Data represent the mean of three biological replicates (n = 3). Heat map intensity reflects iron concentration (µg/g dry weight). Color shading was rendered using the R package ggplantmap, with darker blue indicating higher Fe accumulation. Notably*, pb104::b104^dPAA* lines show increased Fe accumulation in roots and shoots under +Fe conditions.(D) Clustered heatmaps showing the expression profiles (RNA sequencing) of selected Fe homeostasis genes. Heatmaps were generated in RStudio version 4.4.1 using calculated Z-scores of normalized gene expression values across tissues for both +Fe and –Fe conditions. Purple indicates low expression and yellow indicates high expression. Asterisks indicate genotypes that differ significantly from WT within the same tissue and treatment condition ($p < 0.05$), as determined by two-way ANOVA and Tukey's post hoc test (n = 3 for each group).

Figure 4

A

L1 - WT
L2 - *pb104::b104 #1*
L3 - *pb104::b104 #2*
L4 - *pb104::b104^dPAA#2*
L5 - *pb104::b104^dPAA#3*
L6 - *pUBQ10::b104#1*
L7 - *pUBQ10::b104#2*

B

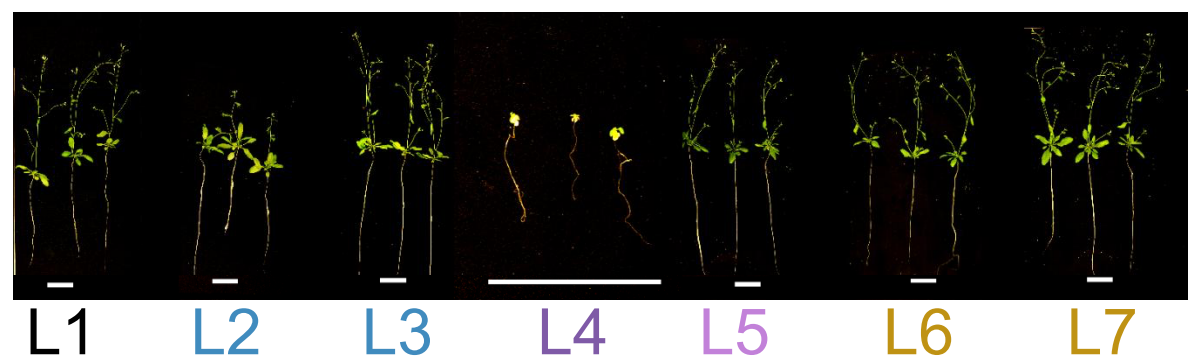

C

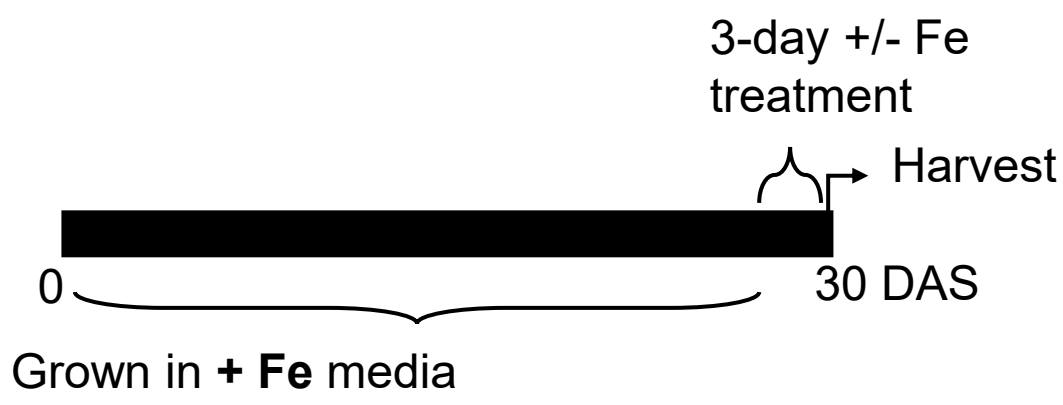

D

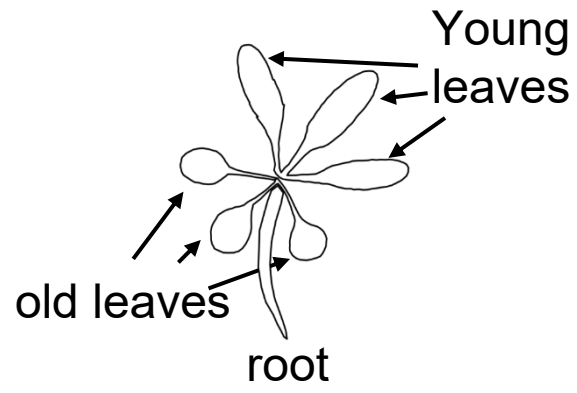

E

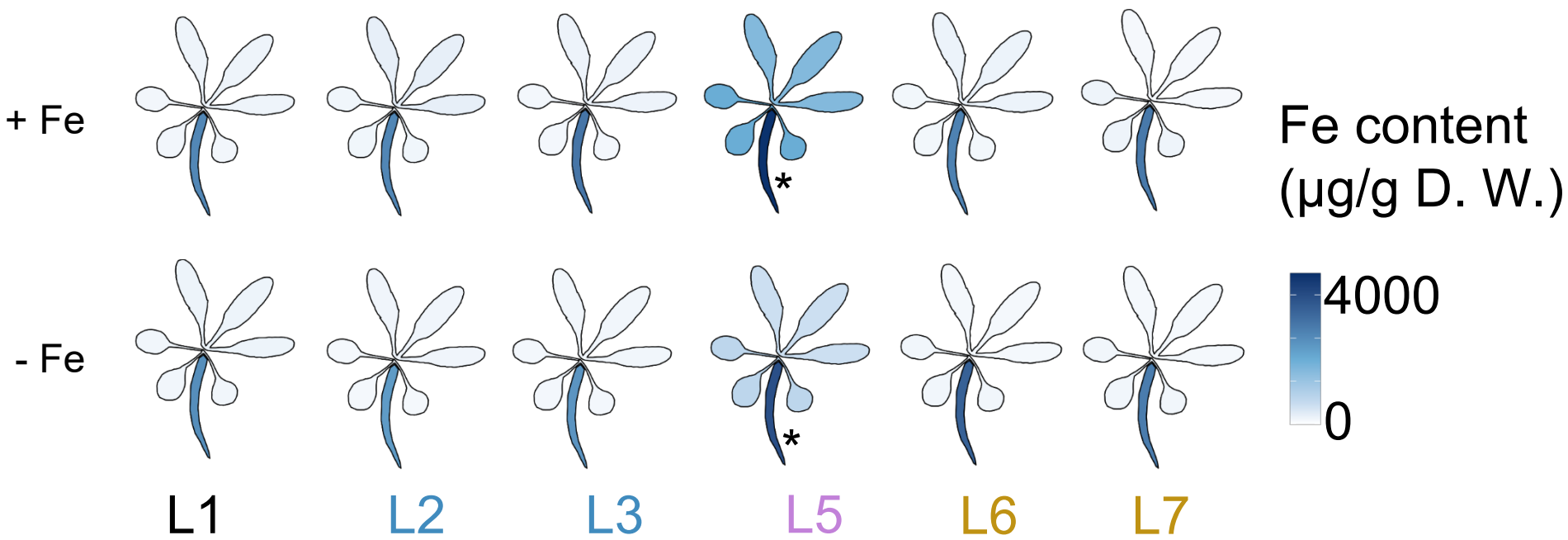

F

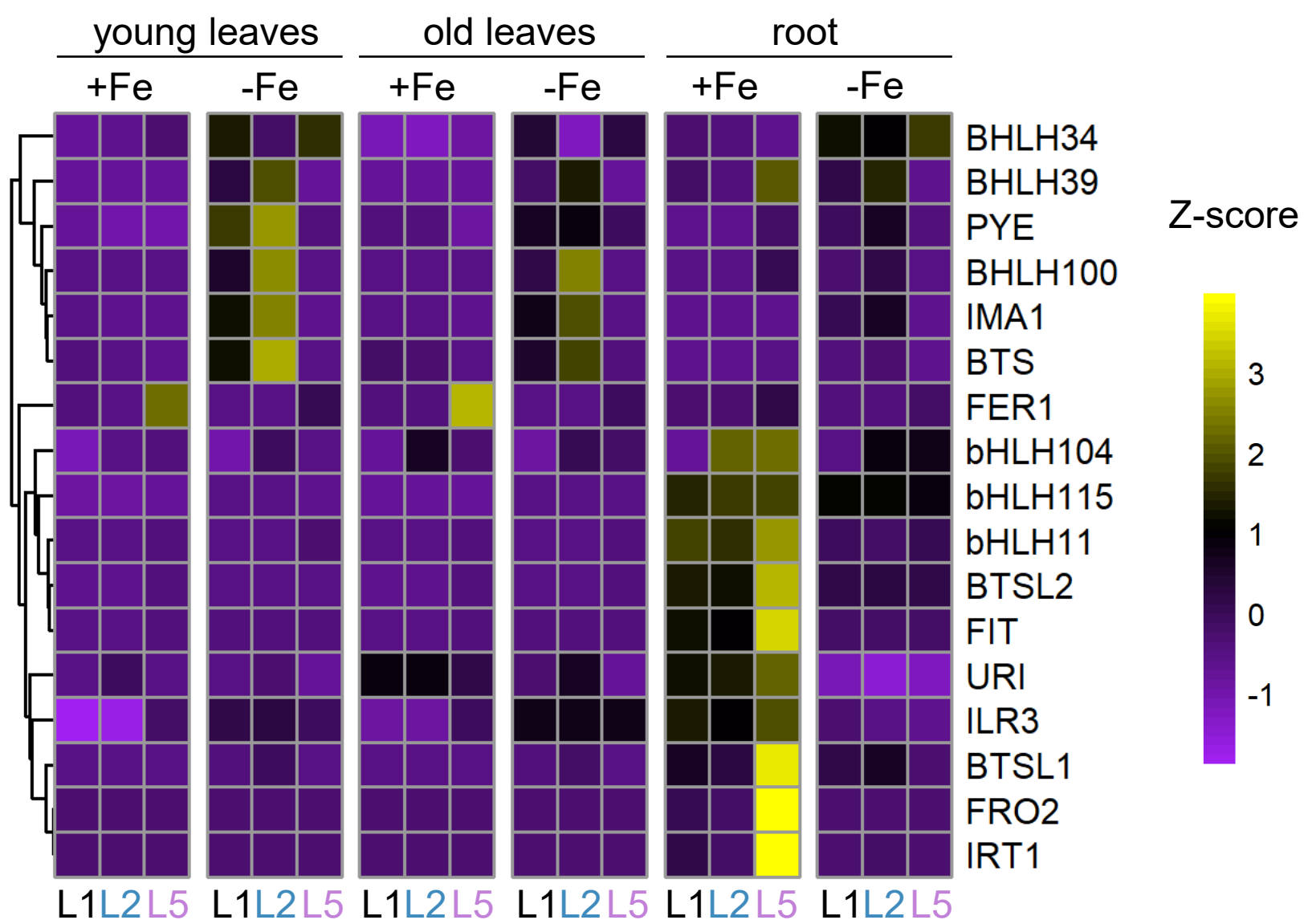

Figure 4. Elevated shoot iron accumulation and altered Fe deficiency responses in reproductive-stage bHLH104^dPAA transgenic lines.

(A) Plant lines used In this experiment
(B) Representative images of 30-days-old Arabidopsis plants grown in hydroponic system (scale bar = 5 cm). Among grown plant lines, *pb104::b104^dPAA #2* (L4) grew poorly and was not used in ICPMS and gene expression analysis.
(C) Experimental design for the dataset shown. Arabidopsis plants were grown hydroponically under iron-sufficient (+Fe) conditions for 27 days, followed by a 3-day treatment with either +Fe or –Fe media.
(D) Schematic representation of tissue separation used for both ICP-MS and RT-qPCR analysis. Young and old leaves were separated from the roots to examine tissue-specific iron accumulation and gene expression. The same tissue layout is used to represent heatmaps in the ICP-MS dataset.
(E) Iron content in young leaves, old leaves, and roots under +Fe and –Fe conditions, measured by ICP-MS. Data represent mean values from three biological replicates (n = 3). Heat map intensity reflects iron concentration (µg/g dry weight). Color shading was generated using the R package ggplantmap, with deeper blue indicating higher Fe content. Asterisks indicate genotypes that differ significantly from WT within the same tissue and treatment condition ($p < 0.05$), as determined by two-way ANOVA and Tukey's post hoc test (n = 3 for each group).
(F) Clustered heatmaps showing the expression profiles (RNA sequencing) of selected Fe homeostasis genes in young leaves, old leaves, and roots under both +Fe and –Fe conditions. Data represent the mean of three biological replicates (n = 3). Z-scores were calculated from normalized RNA expression values and visualized in RStudio version 4.4.1. Yellow indicates high expression; purple indicates low expression.

Figure 5

A

L1 - WT
L2 - *pb104::b104 #1*
L3 - *pb104::b104 #2*
L4 - *pb104::b104^dPAA#1*
L5 - *pb104::b104^dPAA#2*
L6 - *pb104::b104^dPAA#3*
L7 - *pb104::b104^dPAA#4*
L8 - *pUBQ10::b104#1*
L9 - *pUBQ10::b104#2*

B

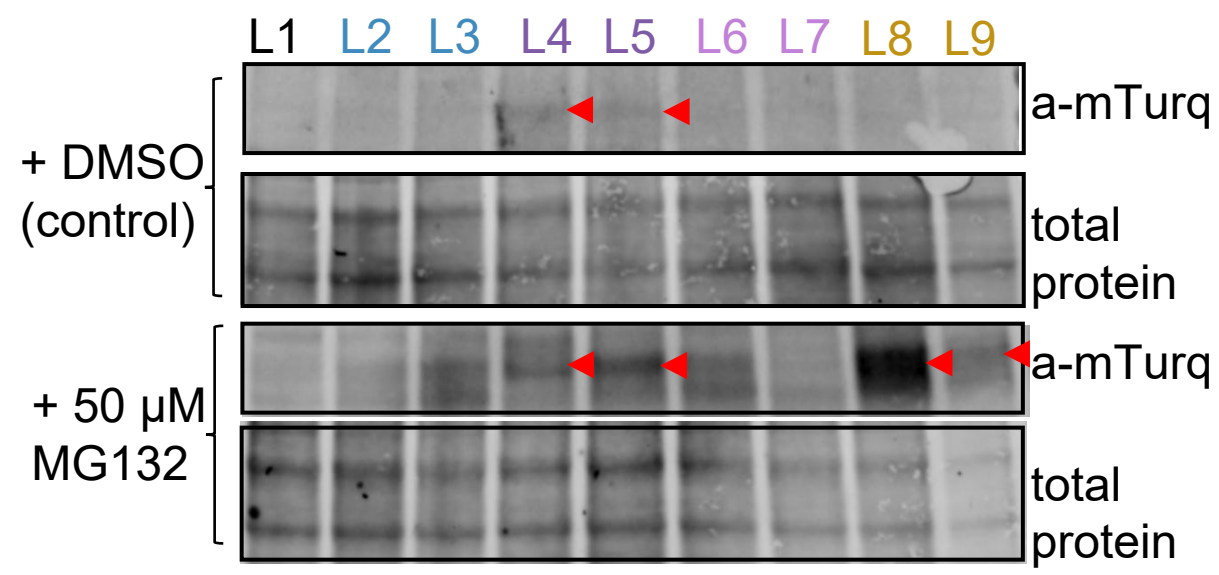

C

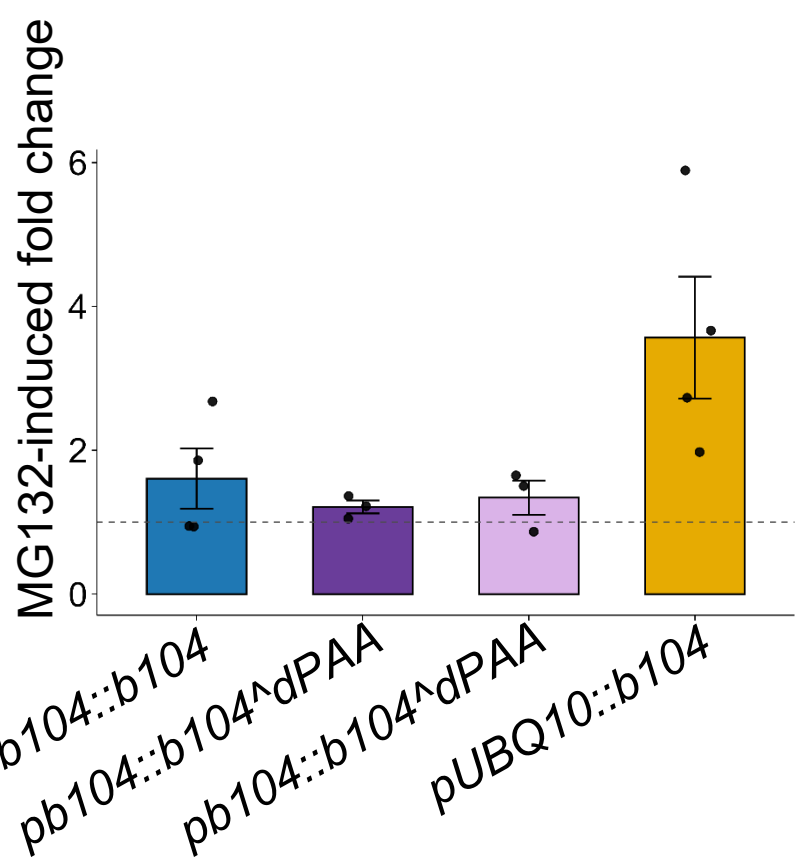

D

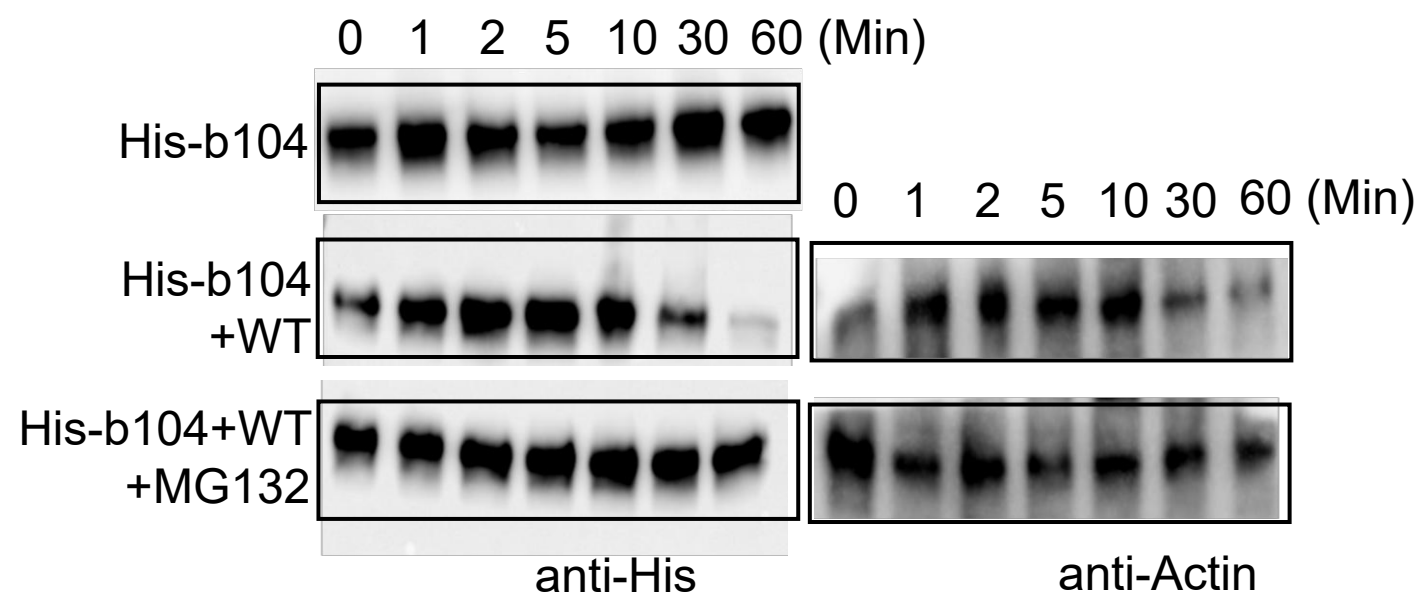

E

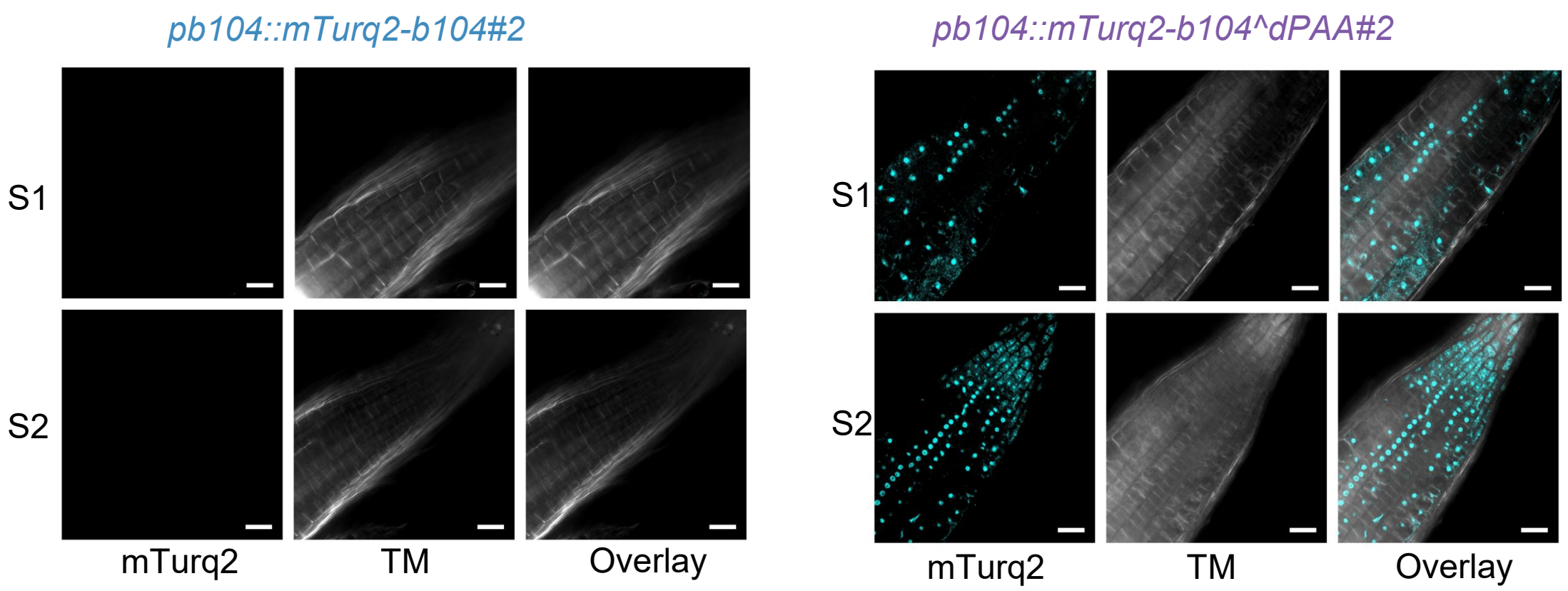

Figure 5. The PAA short sequence mediates bHLH104 protein stability and affects its abundance in Arabidopsis.

(A) Genotypes and transgenic lines used in this experiment.

(B) Immunoblot analysis of mTurquoise2-tagged bHLH104 and b104^dPAA in different transgenic lines treated with either DMSO (control) or 50 μM MG132. Total protein and anti-mTurquoise2 blots are shown. Samples are labeled from #L1 to #L9. The transgenic lines exhibiting increased protein abundance correspond to those that displayed altered growth phenotypes in Figure 1, suggesting a link between protein stability and the observed developmental responses.

(C) Relative protein levels of mTurquoise-tagged bHLH104 were determined by Western blot. Band intensities were normalized to total protein, and fold-change was calculated as the ratio of MG132-treated to DMSO-treated samples. Bars represent mean ± SEM; individual data points are shown.

(D) Cell-free degradation assay showing in vitro degradation of His-tagged bHLH104 protein when incubated with protein extracts from 10-day-old Col-0 (WT) *Arabidopsis thaliana* seedlings. His-bHLH104 was expressed in *E. coli* and remained stable on its own, but degraded upon incubation with the plant extracts, indicating proteasome-mediated degradation. Total protein from whole seedlings was extracted using standard protein extraction procedures. Samples were collected at the indicated time points and analyzed by immunoblotting with anti-His and anti-Actin antibodies. MG132 treatment stabilizes bHLH104, indicating proteasome-dependent degradation.

(E) Confocal microscopy of mTurquoise2 fluorescence in roots of transgenic Arabidopsis seedlings expressing full-length bHLH104 (left) or b104^dPAA (right). Images show two representative seedlings (S1 and S2) per genotype. Arabidopsis thaliana seedlings were at the germination stage, 5 days old, corresponding to 2 days after stratification, and grown on +Fe medium. TM, transmitted light; Overlay, merged mTurq2 and TM channels. Scale bar = 25 μm; excitation at 458 nm; emission collected from 493–613 nm.

Figure 6

A

Alphafold2 multimer structural predictions

Very high (pIDDT > 90)
Confident (90 > pIDDT > 70)
Low (70 > pIDDT > 50)
Very low (pIDDT < 50)

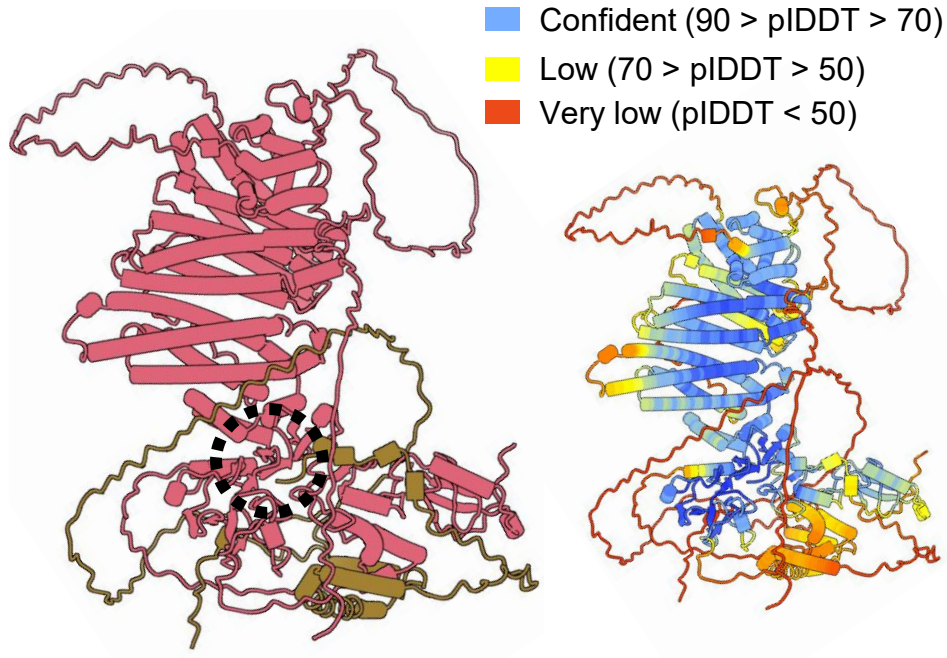

B

Electrostatic surface potential of interaction interfaces

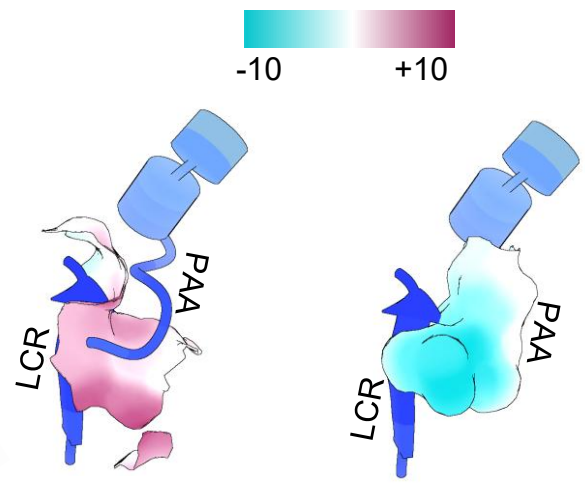

Positive electrostatic potential surface formed by BTS "LCR" residues at interface

Negative electrostatic potential surface formed by bHLH "PAA" residues at interface

C

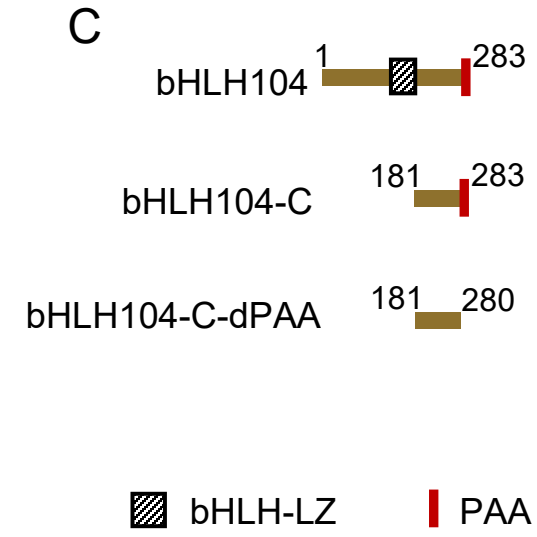

D

AD	BD
bHLH104-C	BTS
bHLH104-C-dPAA	BTS
bHLH104-C	bHLH104-C
bHLH104-C-dPAA	bHLH104-C
bHLH104-C	Empty
Empty	BTS
bHLH104-C-dPAA	Empty

AD	BD
BTS	bHLH104-C
BTS	bHLH104-C-dPAA
bHLH104-C	bHLH104-C-dPAA
Empty	bHLH104-C
BTS	Empty
Empty	bHLH104-C-dPAA

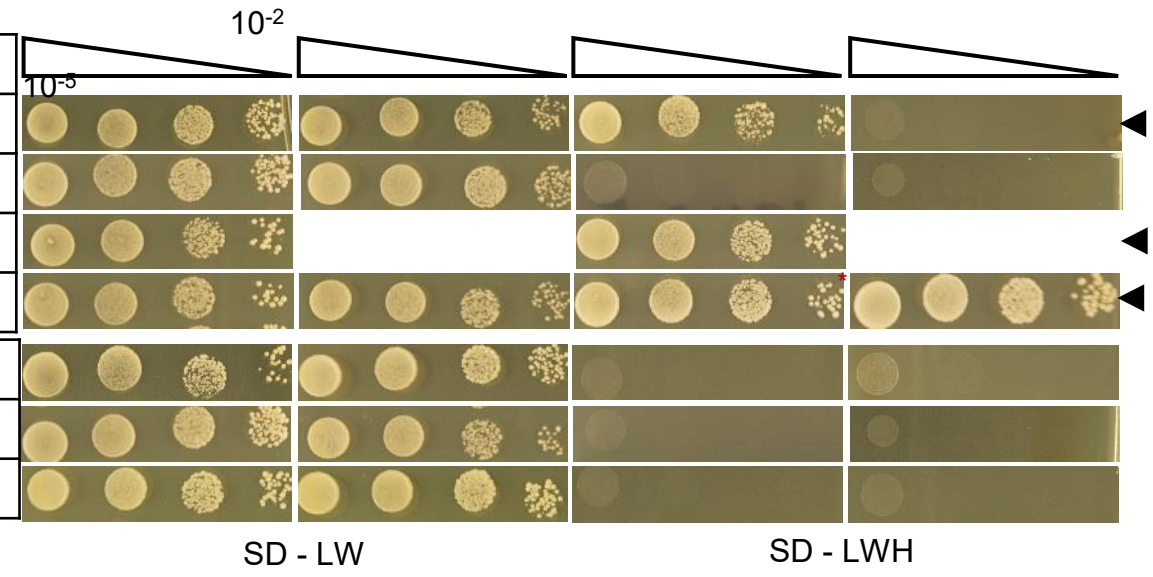

E

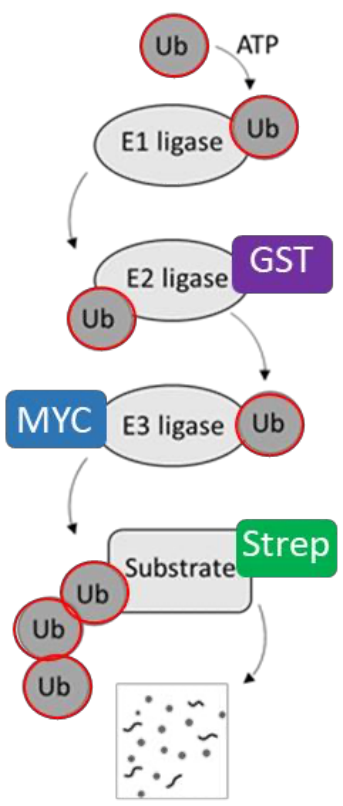

F

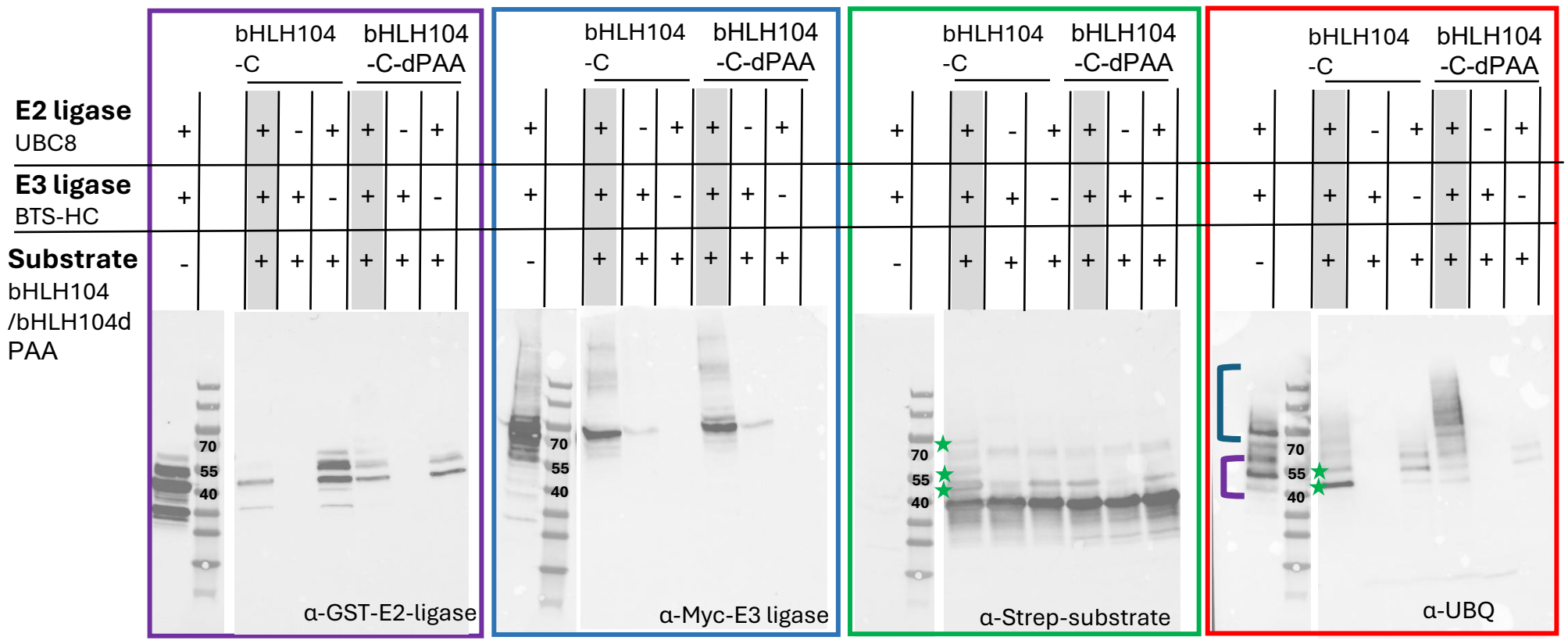

Figure 6. The PAA short sequence is required for bHLH104 interaction with BTS and its ubiquitination.

(A) Structural prediction of the bHLH104–BTS complex using AlphaFold2 Multimer (Evans et al., 2021; Jumper et al., 2021). Left: Chain-colored model showing BTS (rose color) and bHLH104 (bronze color). Right: Per-residue confidence model with pLDDT scores color-coded as very high (pLDDT > 90), confident (90 > pLDDT > 70), low (70 > pLDDT > 50), and very low (pLDDT < 50).

(B) Electrostatic surface potential modeling (Pettersen et al., 2004) reveals a negatively charged region near the proline–alanine–alanine (PAA) sequence in bHLH104 that complements a positively charged surface in the leucine–cysteine–arginine (LCR) domain of BTS. The electrostatic scale ranges from –10 (purple) to +10 (cyan) kT/e.

(C) Schematic representation of full-length bHLH104, bHLH104-C and bHLH104-C-dPAA used for Y2H and UbiGate assays. C-terminal parts lack the N-terminus and the DNA-binding basic Helix Loop Helix (bHLH) domain. Numbers indicate amino acid positions.

(D)Yeast two-hybrid assays showing protein–protein interactions between bHLH104-C or bHLH104-C^dPAA and BTS. bHLH104 homodimerization serves as a control. Full length bHLH104 shows autoactivation in Y2H. Hence bHLH104-C and bHLH104-C-dPAA were used.

(E) Schematic overview of the ubiquitin/ 26s proteosome pathway. Each component is expressed in *E.coli* for UbiGate assay. Recombinant bHLH104 or bHLH104^dPAA proteins (Strep-tagged) were used as substrates. BTS-HC served as the E3 ligase (Myc-tagged), in combination with UBC8 (E2) (GST-tagged) and an E1 activating enzyme.

(F) Ubiquitination assay showing that bHLH104 undergoes polyubiquitination in the presence of E1, E2, E3, and ubiquitin (Ub), whereas bHLH104^dPAA fails to be ubiquitinated. Immunoblots with anti-GST (E2), anti-Myc (E3), anti-Strep (substrate), and anti-UBQ (ubiquitin) confirm protein expression and substrate modification

Figure 7

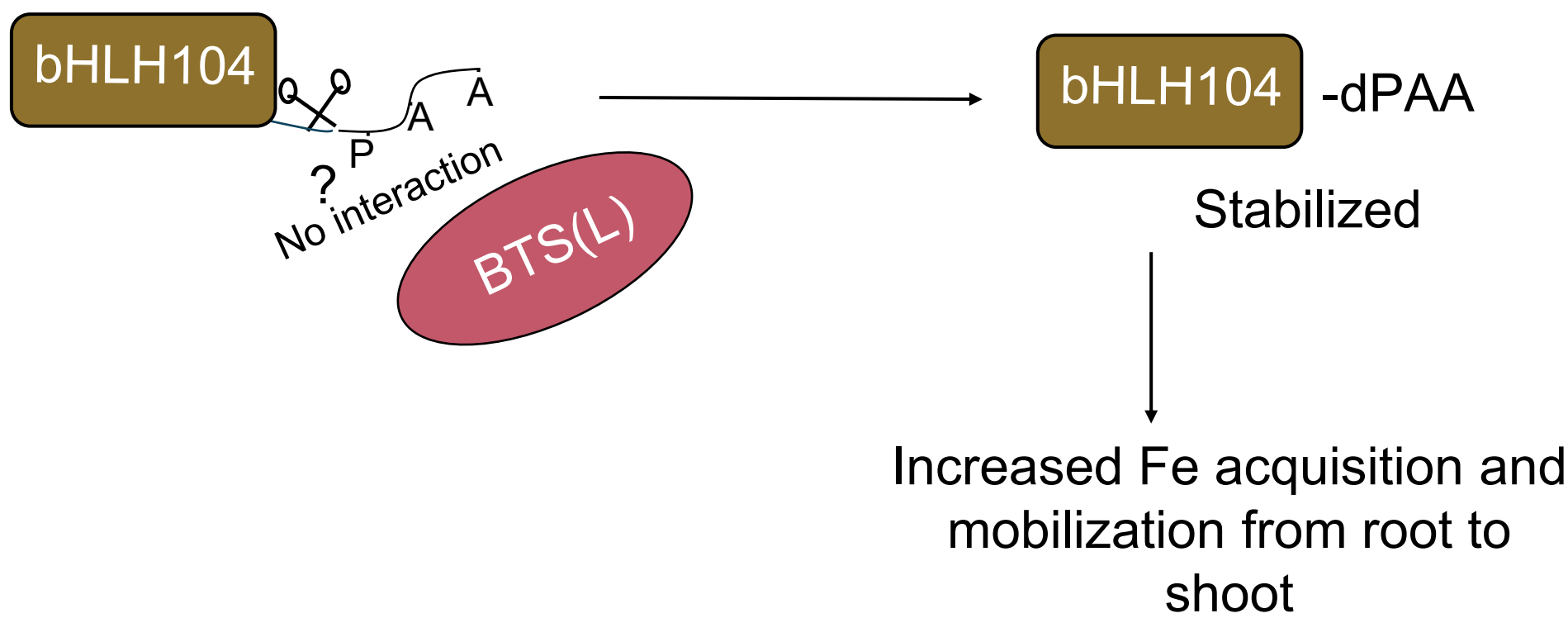

Figure 7. Working model of bHLH104 regulation through the C-terminal PAA sequence and its impact on Fe homeostasis.
The C-terminal PAA sequence in bHLH104 mediates interaction with BTS-type E3 ligases, targeting the protein for proteasomal degradation. Deletion of the PAA motif (b104^dPAA) disrupts this interaction, leading to protein stabilization. The increased abundance of stabilized b104^dPAA enhances Fe acquisition responses in *Arabidopsis*.

Supplementary Figure S1

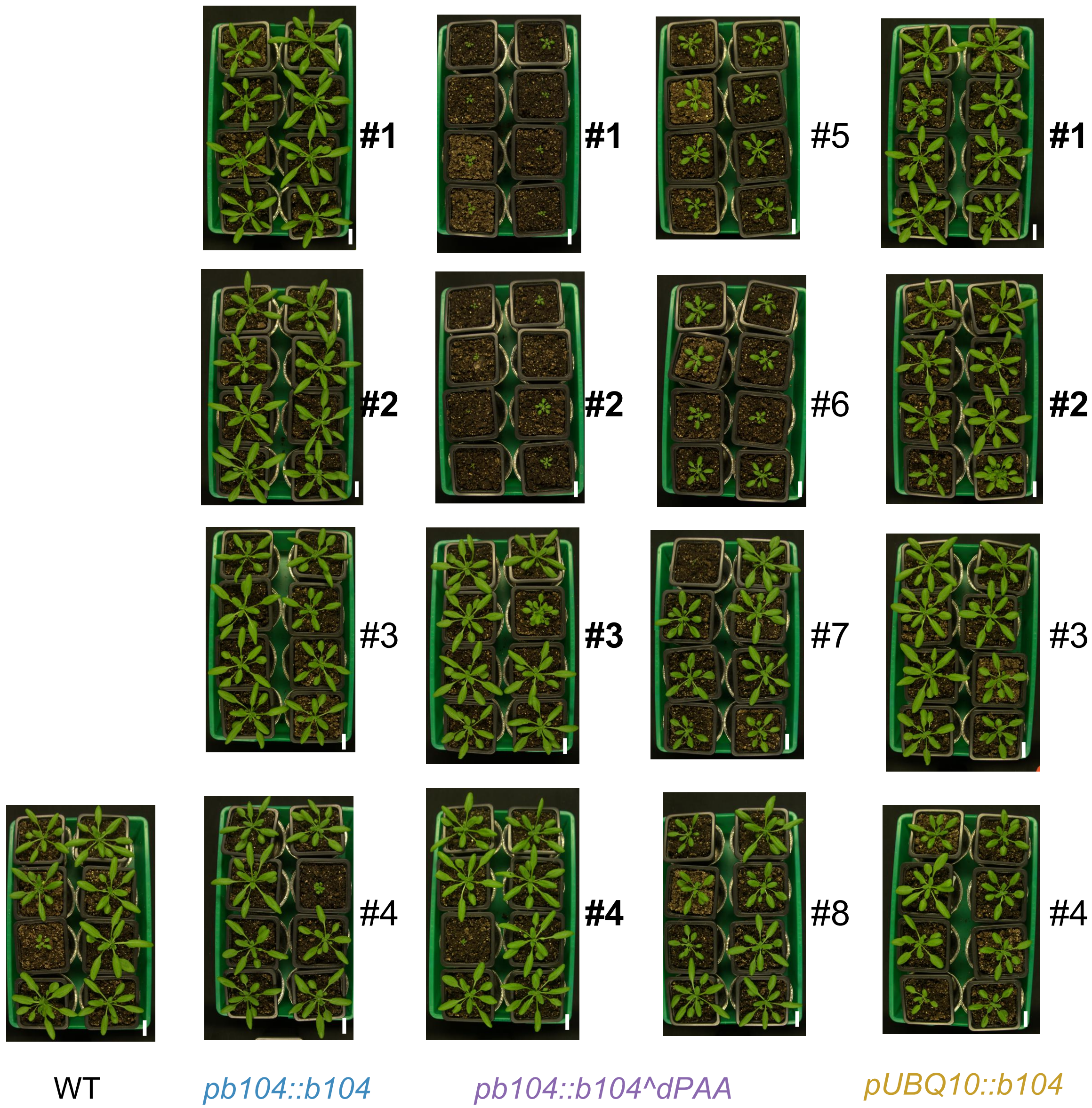

Supplementary Figure S1. Preliminary phenotypic screen of independent transgenic *Arabidopsis* lines expressing bHLH104 or bHLH104^dPAA. 26 days old plants of Col-0 wild type (WT), *pb104::b104*, *pb104::b104^dPAA*, and *pUBQ10::b104* lines were grown under same conditions. Lines selected for further analysis in the main study are indicated: *pb104::b104 lines* #1 and #2, and *pb104::b104^dPAA lines #1–#4* and *pUBQ10::b104* lines #1 and #2, scale bar = 2 cm.

Supplementary Figure S2

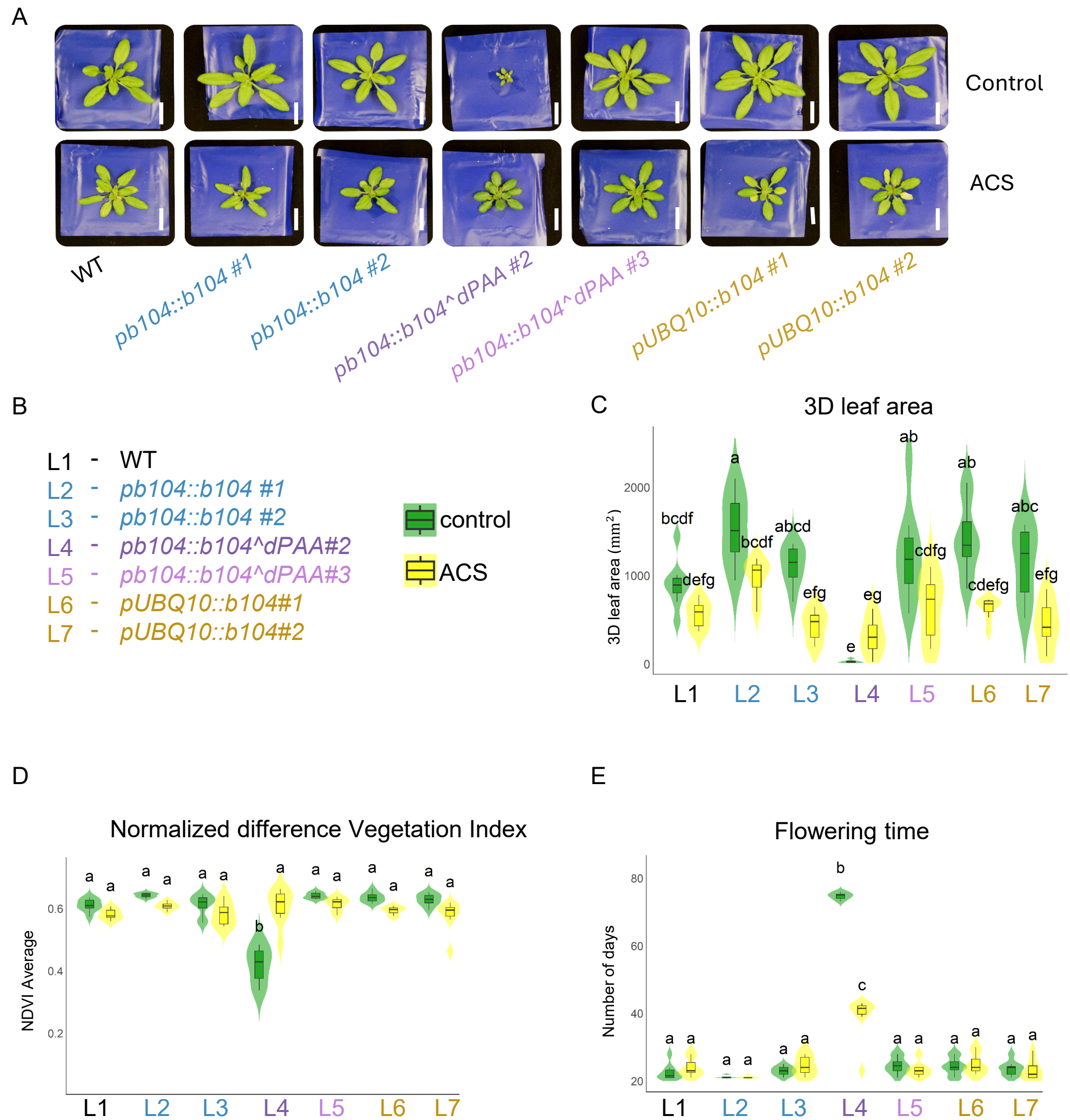

Supplementary Figure S2. Response of bHLH104^dPAA transgenic lines to iron-limiting conditions in alkaline calcareous soil (ACS).
Arabidopsis thaliana transgenic lines were grown in either control soil (pH 5.9) or alkaline calcareous soil (ACS, pH 8.1).(A) Photos of four-week-old plants grown in control and ACS soil conditions.(B) List of plant lines used in this experiment, numbered from L1 to L7. scale bar = 2 cm (C) 3D leaf area measurements: Plants were evaluated for leaf expansion and overall growth in both conditions.(D) NDVI (Normalized Difference Vegetation Index): NDVI values were measured to assess photosynthetic activity in response to ACS conditions.(E) Flowering time: Flowering time was compared between control and ACS conditions, with letters indicating statistical differences. Statistical significance was assessed by two-way ANOVA followed by Tukey's HSD test ($p < 0.05$). N = 8 plants per line.

Supplementary Figure S3

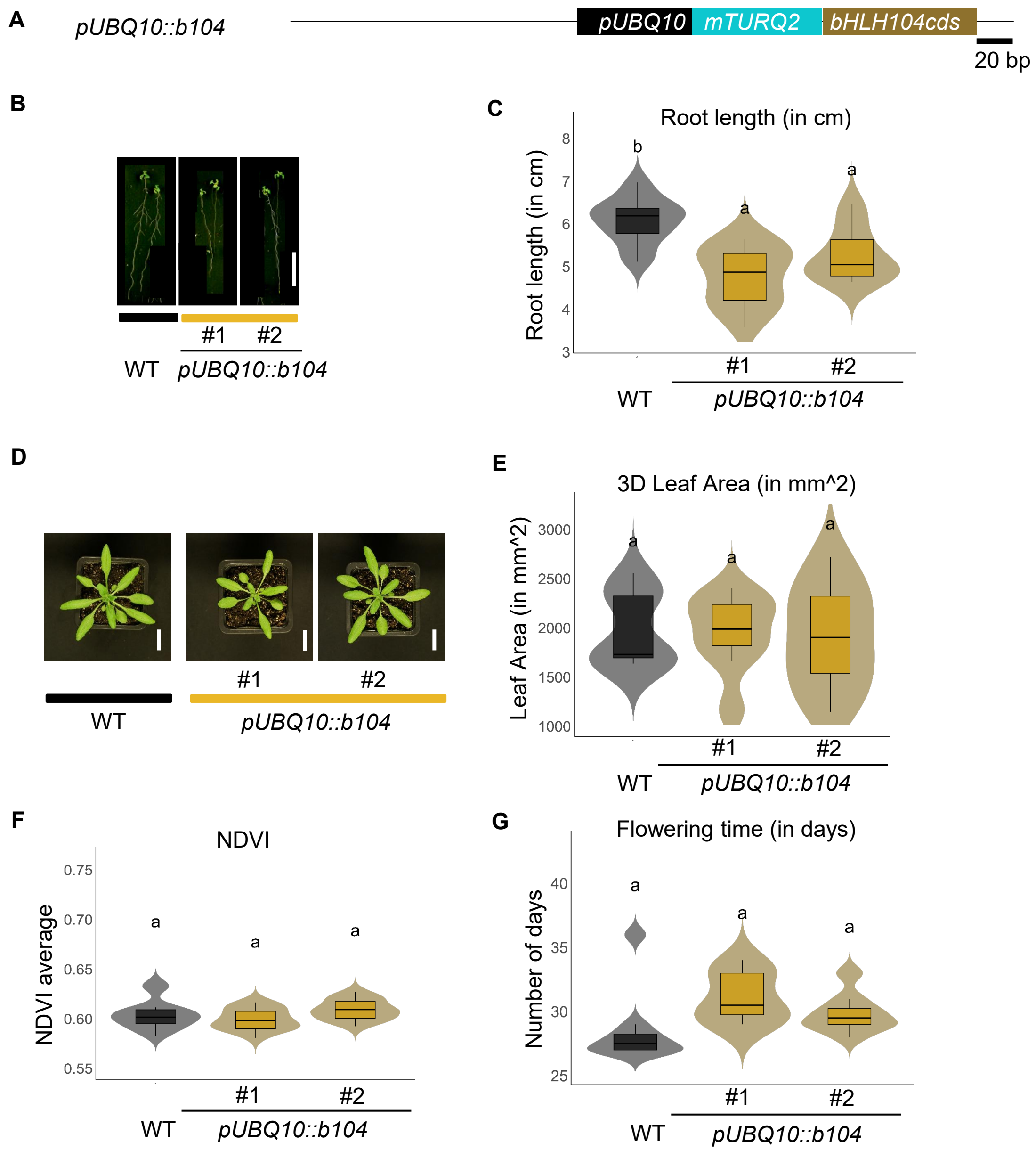

Supplmentary Figure S3. Constitutive expression of bHLH104 did not alter growth and physiological traits in Arabidopsis.

(A) Schematic representation of the construct used to generate transgenic lines expressing full-length bHLH104 (*pUBQ10::bHLH104*). The construct is driven by the ubiquitin 10 (UBQ10) promoter and is fused at the N-terminus to the mTurquoise2 fluorescent tag. Scale bar = 20 bp.

(B-C) Photos and root length quantification data of 12-day-old seedlings grown vertically on Hoagland medium supplemented with iron (+Fe). Scale bar =2 cm

(D) Representative images of 4-week-old Arabidopsis plants grown in soil. Shown are Col-0 (WT) and two independent *pUBQ10::b104* lines (#1, #2). Scale bar = 2 cm

(E–F) Quantitative analysis of aboveground phenotypes acquired using the Phenospex PlantEye system: (E) 3D leaf area (mm^2); (F) NDVI (Normalized Difference Vegetation Index).

(G) Flowering time, measured manually as the number of days to bolting.

Data represent means ± SD (n = 7–12 biological replicates per line). Statistical analysis was performed using two-way ANOVA followed by Tukey's post hoc test. Different letters indicate statistically significant differences at $p < 0.05$.

Supplementary Figure S4

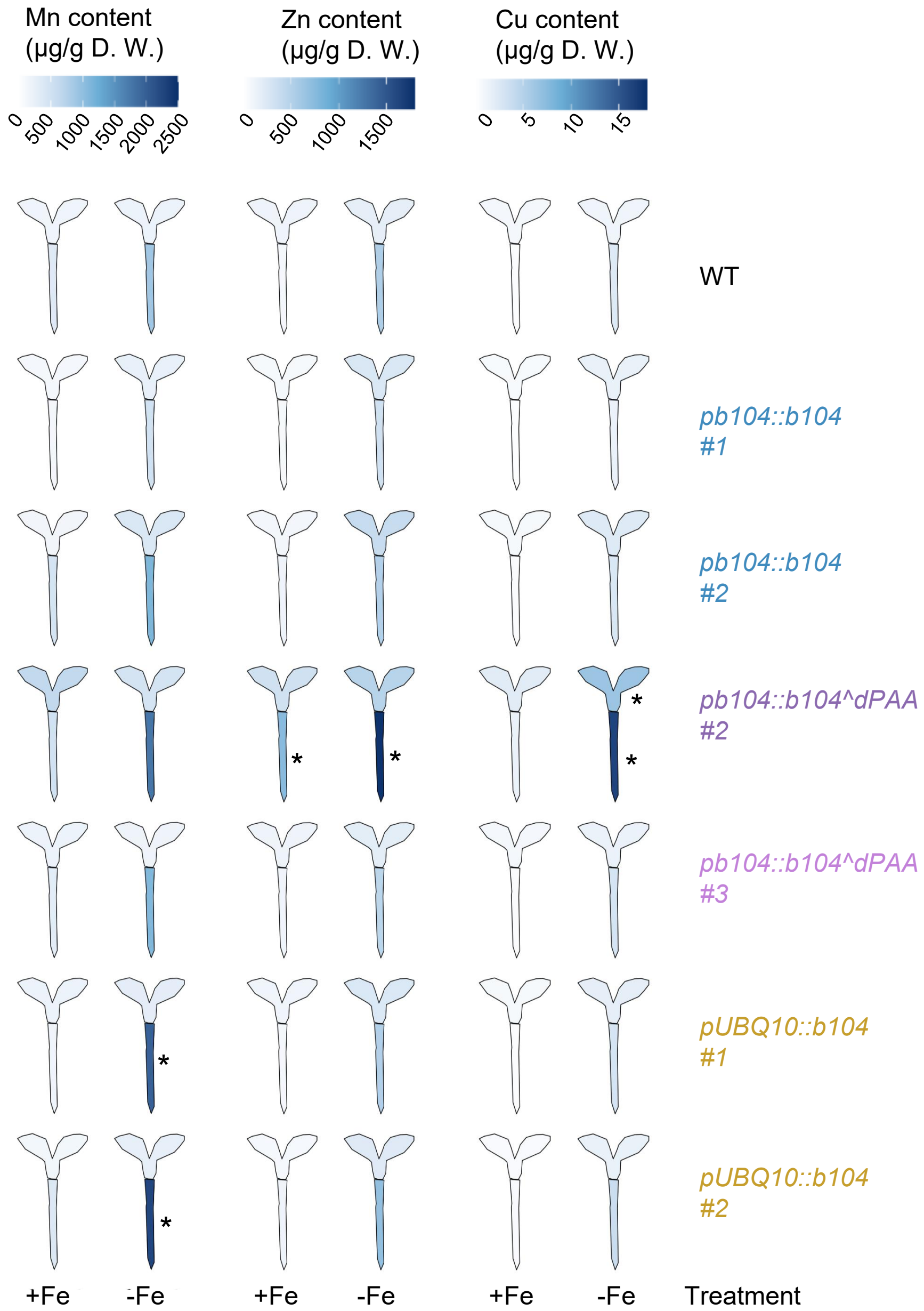

Supplementary Figure S4. Elemental content analysis of Mn, Zn, and Cu in 10-day old Arabidopsis seedlings.

Heatmap showing the distribution of Mn, Zn, and Cu content (in µg/g dry weight) across different *Arabidopsis* seedlings, including wild-type (WT), pb104::b104 (lines #1, #2), *pb104::b104^dPAA* (lines #2, #3), *pUBQ10::b104* (lines #1, #2). The color scale indicates the range of elemental concentrations from low (light blue) to high (dark blue). Seedlings were grown in Hoagland media with or without 50 mM Fe supplementation. Data were collected from 10-day-old seedlings, with elemental content measurements obtained via ICP-MS analysis. Three biological replicates per line were used. The plot was generated using the ggPlantMap package in RStudio. Asterisks indicate genotypes that differ significantly from WT within the same tissue and treatment condition ($p < 0.05$), as determined by two-way ANOVA and Tukey's post hoc test ($n = 3$ for each group).

Supplementary Figure S5

A

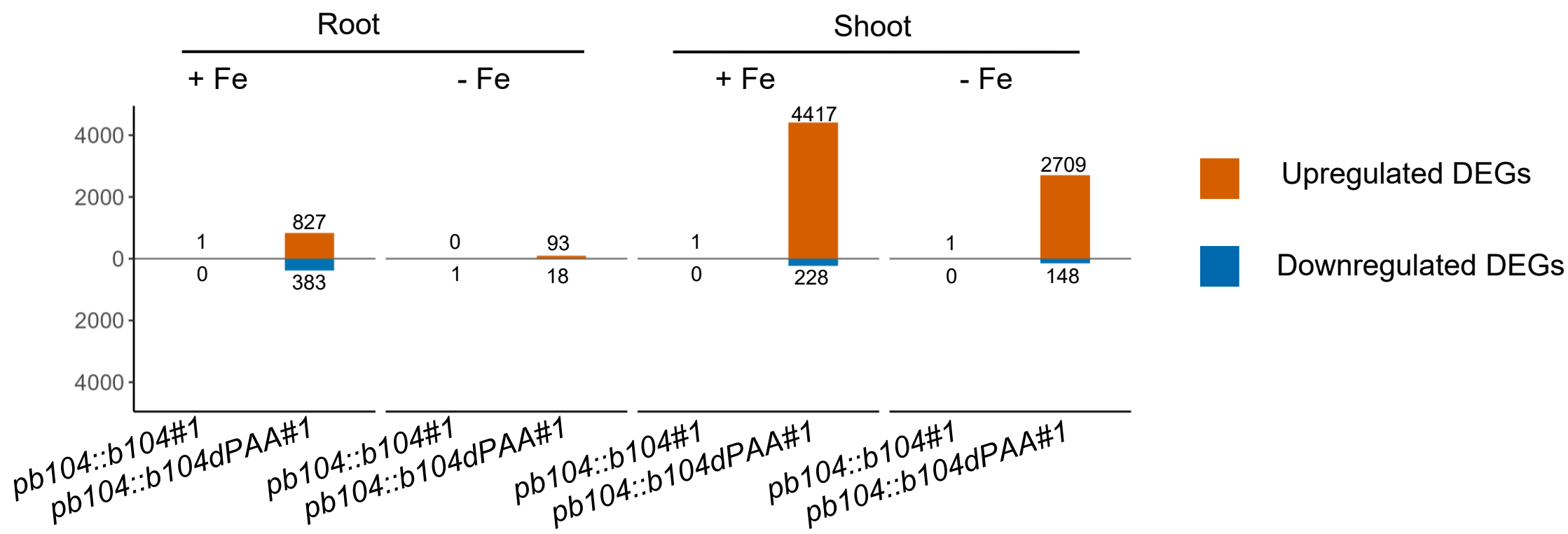

B

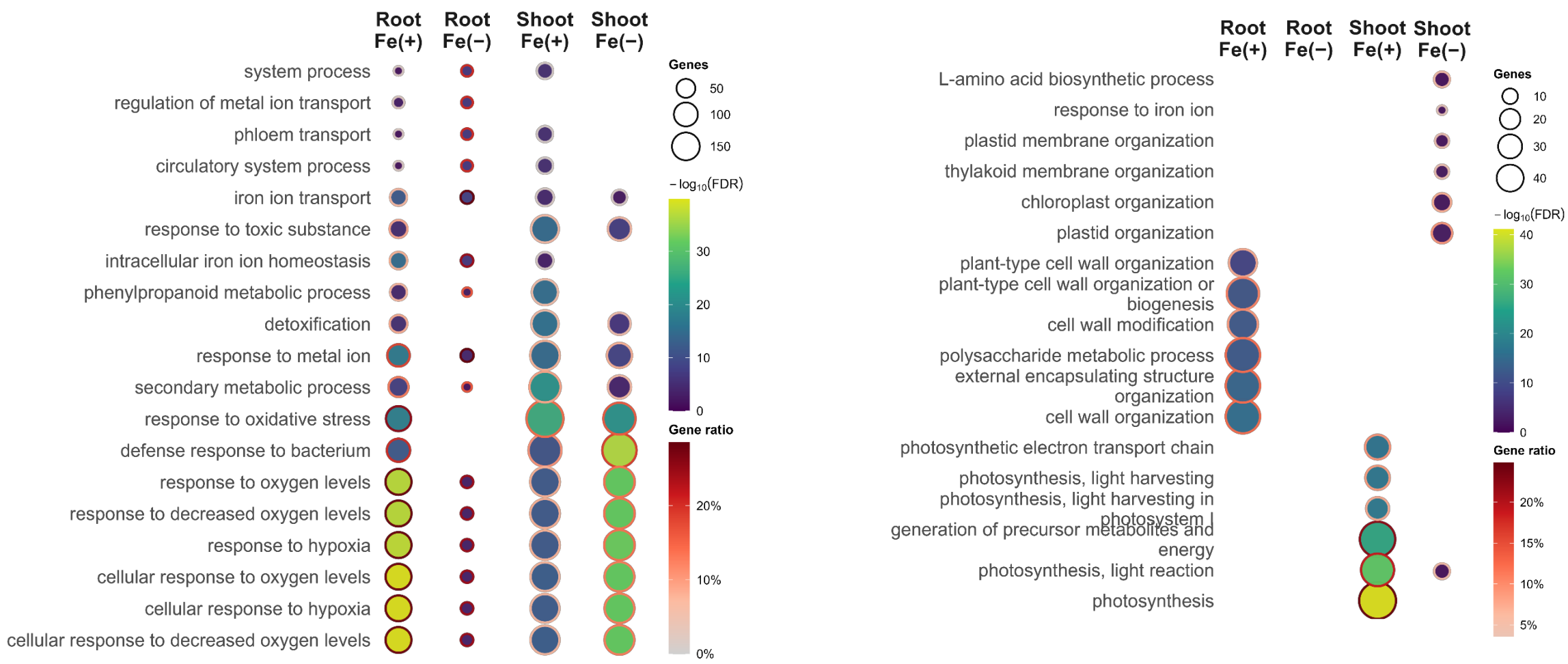

Supplementary Figure S5: Differential expression and GO enrichment across seedling tissues.

(A) Counts of differentially expressed genes (DEGs) for each line vs WT in root and shoot under Fe(+) and Fe(−). Orange = up-regulated; blue = down-regulated; numbers above/below bars indicate counts. DEGs were defined at FDR ≤ 0.05 and |log2FC| ≥ 0.58. X-axis labels show the abbreviated line IDs.

(B) GO Biological Process enrichment for the up-regulated (left panel) and down-regulated (right panel) DEG sets. Columns correspond to tissue/Fe combinations (Root Fe(+), Root Fe(−), Shoot Fe(+), Shoot Fe(−)). Each dot represents a significant term (BH FDR ≤ 0.05); dot size = number of genes in the term, fill = −log10(FDR), and ring color = GeneRatio. Terms plotted are the top-ranked per panel; the gene universe was all genes tested in the corresponding comparison.

Supplementary Figure S6

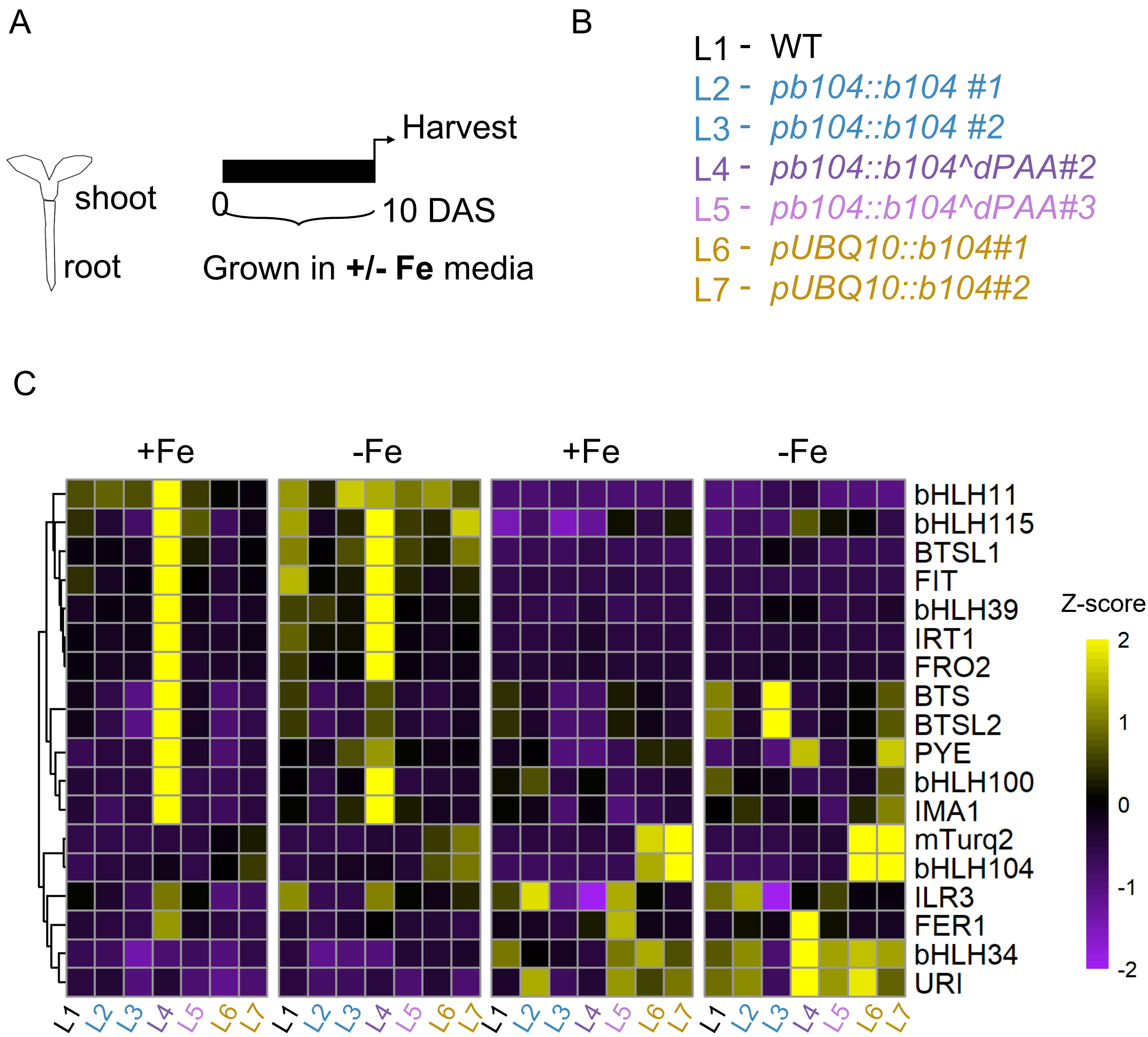

Supplementary Figure S6. Targeted gene expression profiling in seedlings.
(A) Schematic representation of the experimental design. Arabidopsis seedlings were grown for 10 days after sowing (DAS) under either iron-sufficient (+Fe) or iron-deficient (–Fe) conditions. Shoot and root tissues were collected separately for RT-qPCR analyses. (B) Genotypes used in this study. (C) Clustered heatmaps showing the expression profiles of selected Fe homeostasis genes. Heatmaps were generated in RStudio version 4.4.1 using calculated Z-scores of normalized gene expression values across tissues for both +Fe and –Fe conditions. Purple indicates low expression and yellow indicates high expression. Asterisks indicate genotypes that differ significantly from WT within the same tissue and treatment condition ($p < 0.05$), as determined by two-way ANOVA and Tukey's post hoc test ($n = 3$ for each group).

Supplementary Figure S7

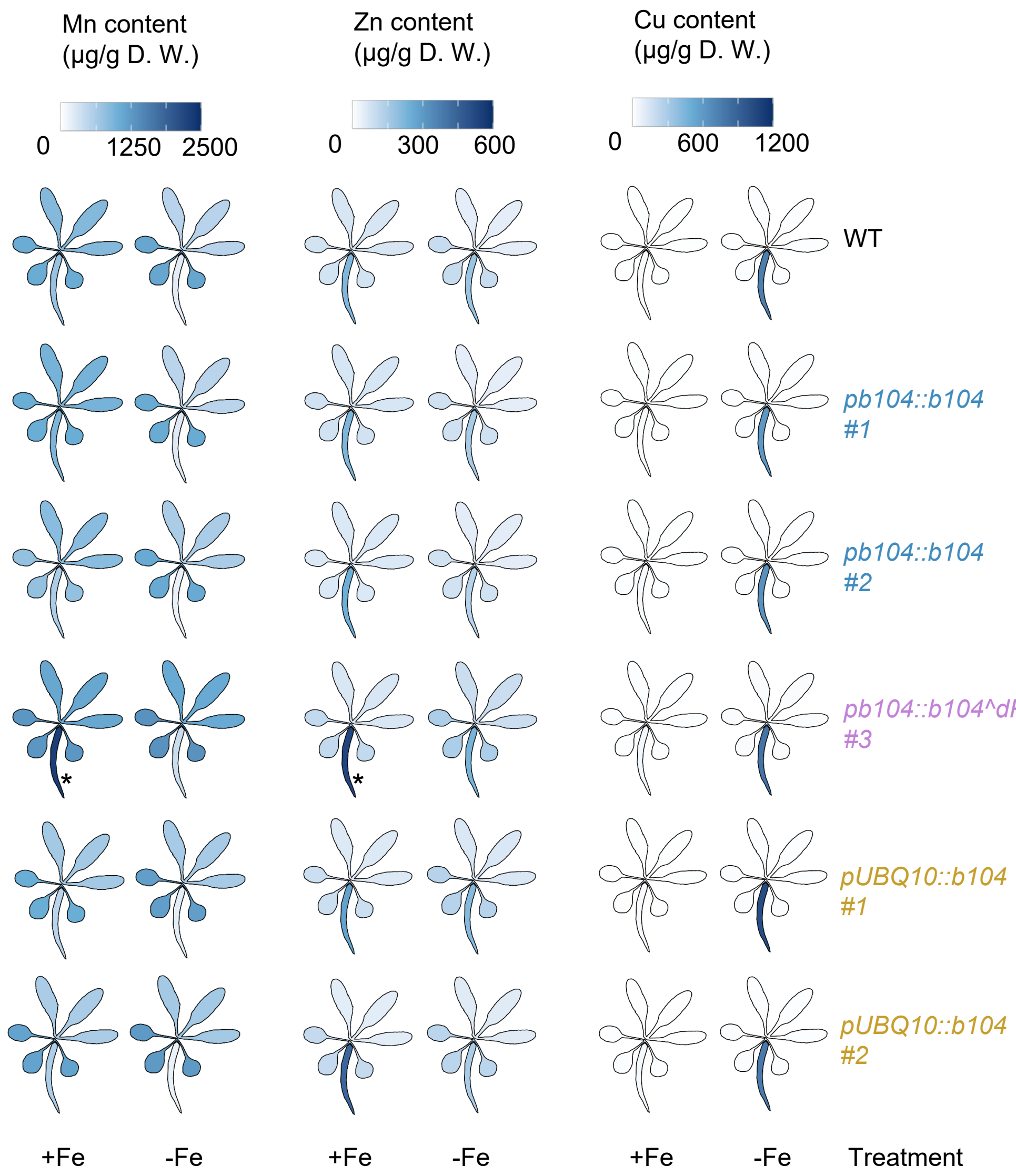

Supplementary Figure S7. Elemental content analysis of Mn, Zn, and Cu in mature *Arabidopsis thaliana*.
Heatmap showing the distribution of iron (Fe) content (in µg/g dry weight) in young leaves, old leaves, and roots of *Arabidopsis* transgenic lines, including wild-type (WT), *pb104::b104* (lines #1, #2), *pb104::b104^dPAA* (line #3), *pUBQ10::b104* (lines #1, #2). Plants were grown hydroponically under iron-sufficient (+Fe) conditions for 27 days, followed by a 3-day treatment with either +Fe or –Fe media. The color scale indicates the iron content, with darker blue shades representing higher iron concentrations. Data represent the mean values from three biological replicates (n = 3). Heatmap intensity reflects iron concentration (µg/g dry weight) measured by ICP-MS. The plot was generated using the ggPlantMap package in RStudio. Asterisks indicate genotypes that differ significantly from WT within the same tissue and treatment condition ($p < 0.05$), as determined by two-way ANOVA and Tukey's post hoc test (n = 3 for each group).

Supplementary Figure S8

A

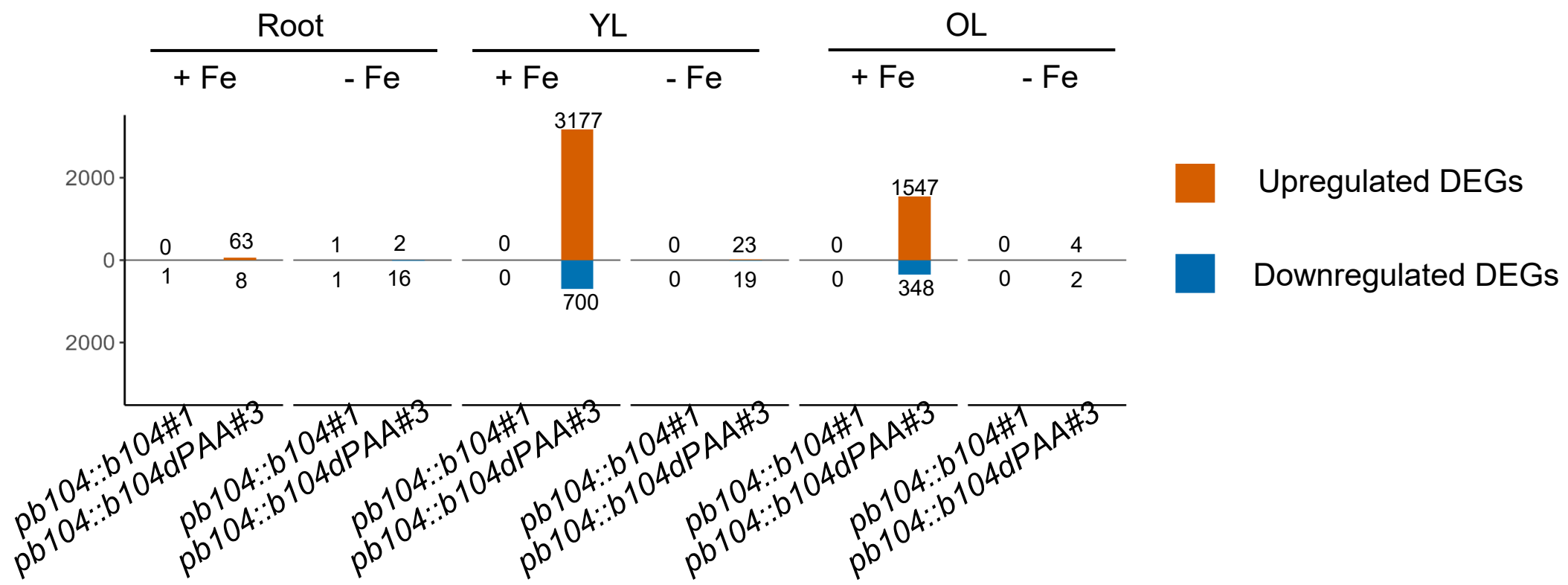

B

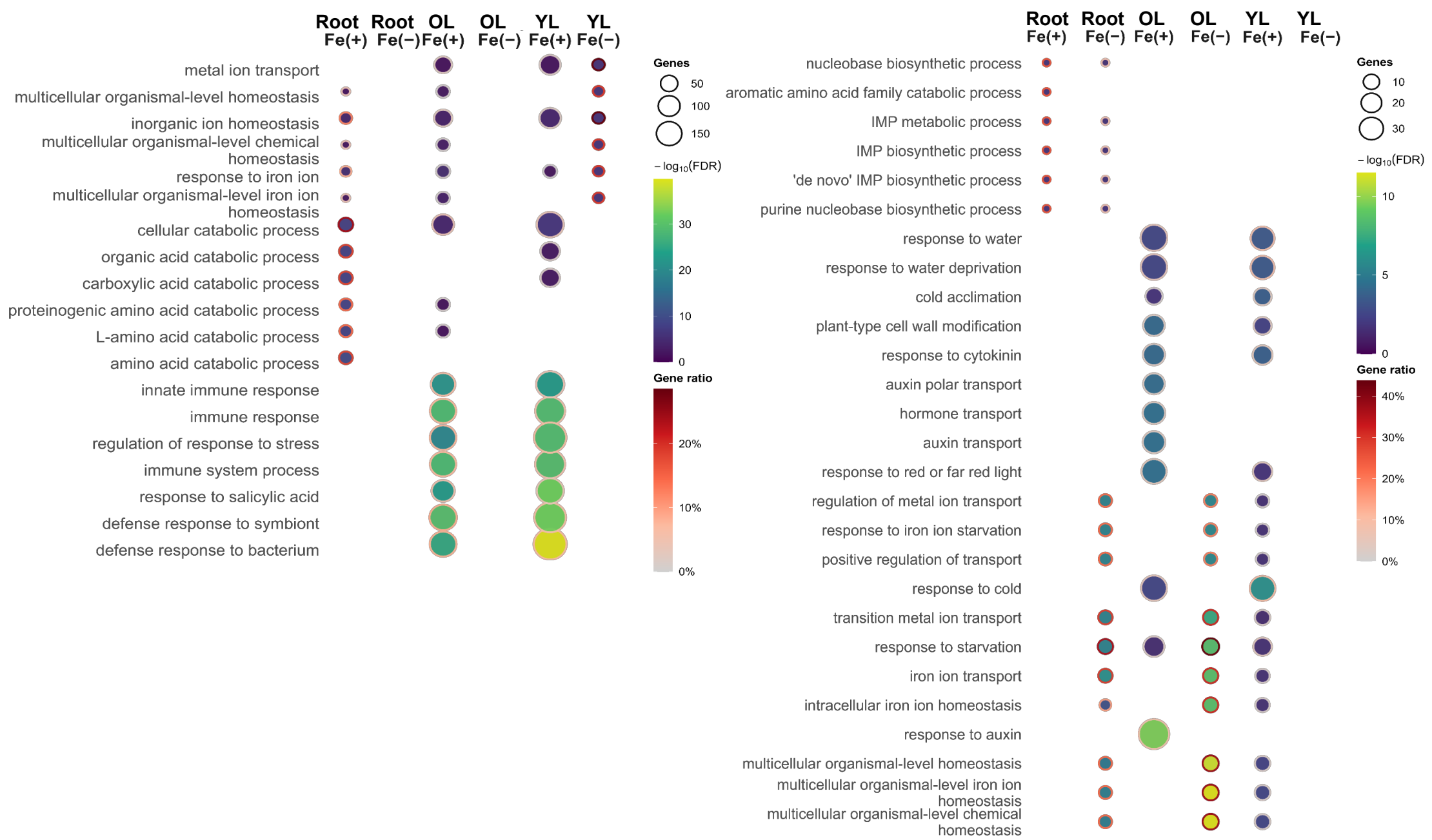

Supplementary Figure S8: Differential expression and GO enrichment across reproductive stage tissues

(A) Numbers of differentially expressed genes (DEGs) for each line vs WT in root (Root), young leaves (YL), and old leaves (OL) under Fe(+) and Fe(−). Orange bars show up-regulated DEGs; blue bars show down-regulated DEGs; values above/below bars are counts. DEGs were defined at FDR ≤ 0.05 and |log2FC| ≥ 0.58.

(B) GO Biological Process enrichment for the up-regulated (left panel) and down-regulated (right panel) DEG sets. Columns correspond to tissue/Fe combinations (Root, YL, OL × Fe(+), Fe(−)). Each dot represents a significant term (BH FDR ≤ 0.05); dot size = number of genes in the term, fill = −log10(FDR), and ring color = GeneRatio. Terms shown are the top-ranked per panel; the gene universe comprised all genes tested in the corresponding comparison. Abbreviations: YL, young leaves; OL, old leaves.

Supplementary Figure S9

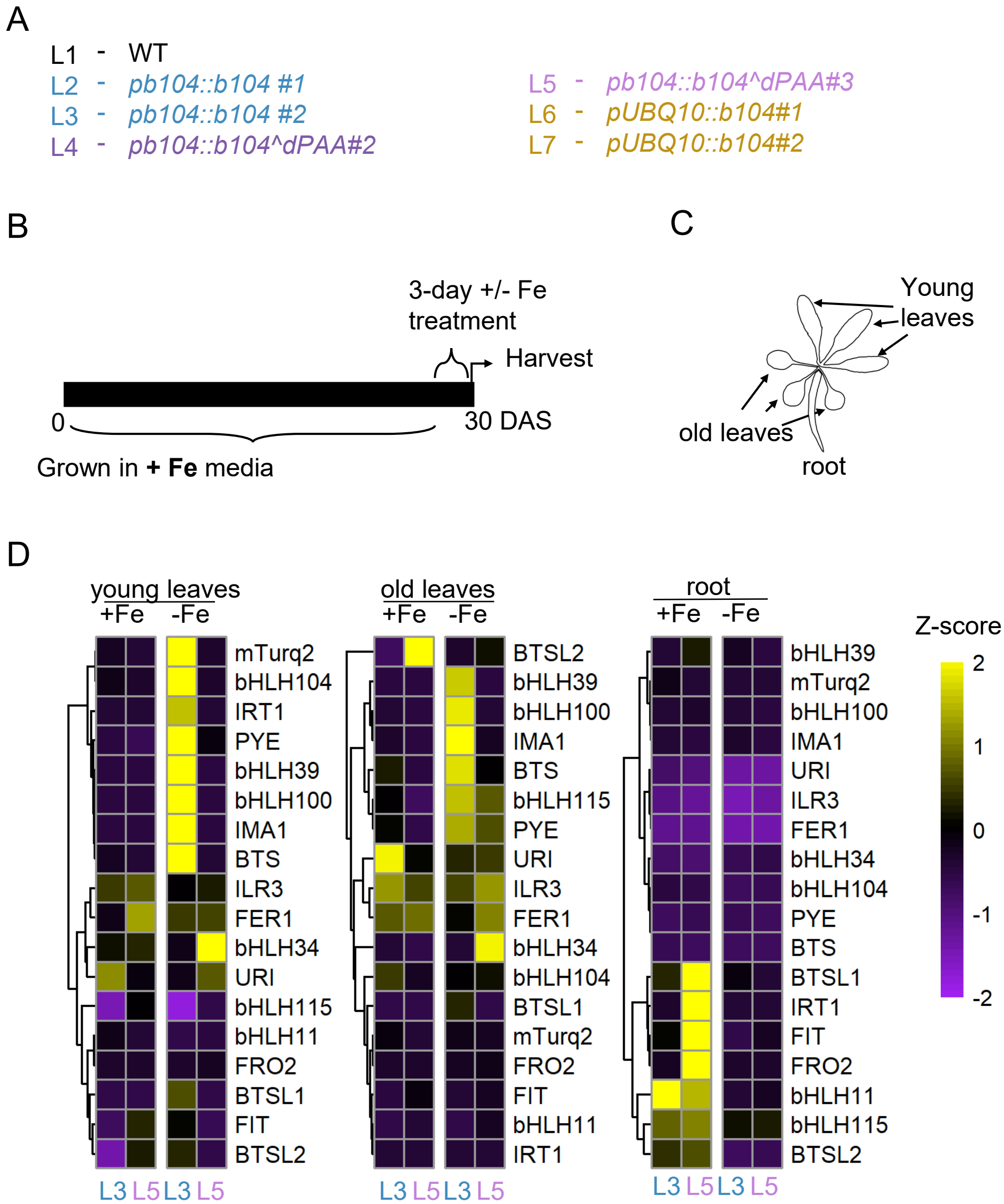

Supplementary Figure S9. Targeted gene expression profiling in reproductive-stage plants

(A) Plant lines used In this experiment

(B) Experimental design for the dataset shown. *Arabidopsis* plants were grown hydroponically under iron-sufficient (+Fe) conditions for 27 days, followed by a 3-day treatment with either +Fe or –Fe media.

(C) Schematic representation of tissue separation used for RT-qPCR analysis. Young and old leaves were separated from the roots to examine tissue-specific iron accumulation and gene expression.

(D) Clustered heatmaps showing the expression profiles of selected Fe homeostasis genes in young leaves, old leaves, and roots under both +Fe and –Fe conditions. Data represent the mean of three biological replicates (n = 3). Z-scores were calculated from normalized RT-qPCR expression values and visualized in RStudio version 4.4.1. Yellow indicates high expression; purple indicates low expression.

Supplementary Figure S10

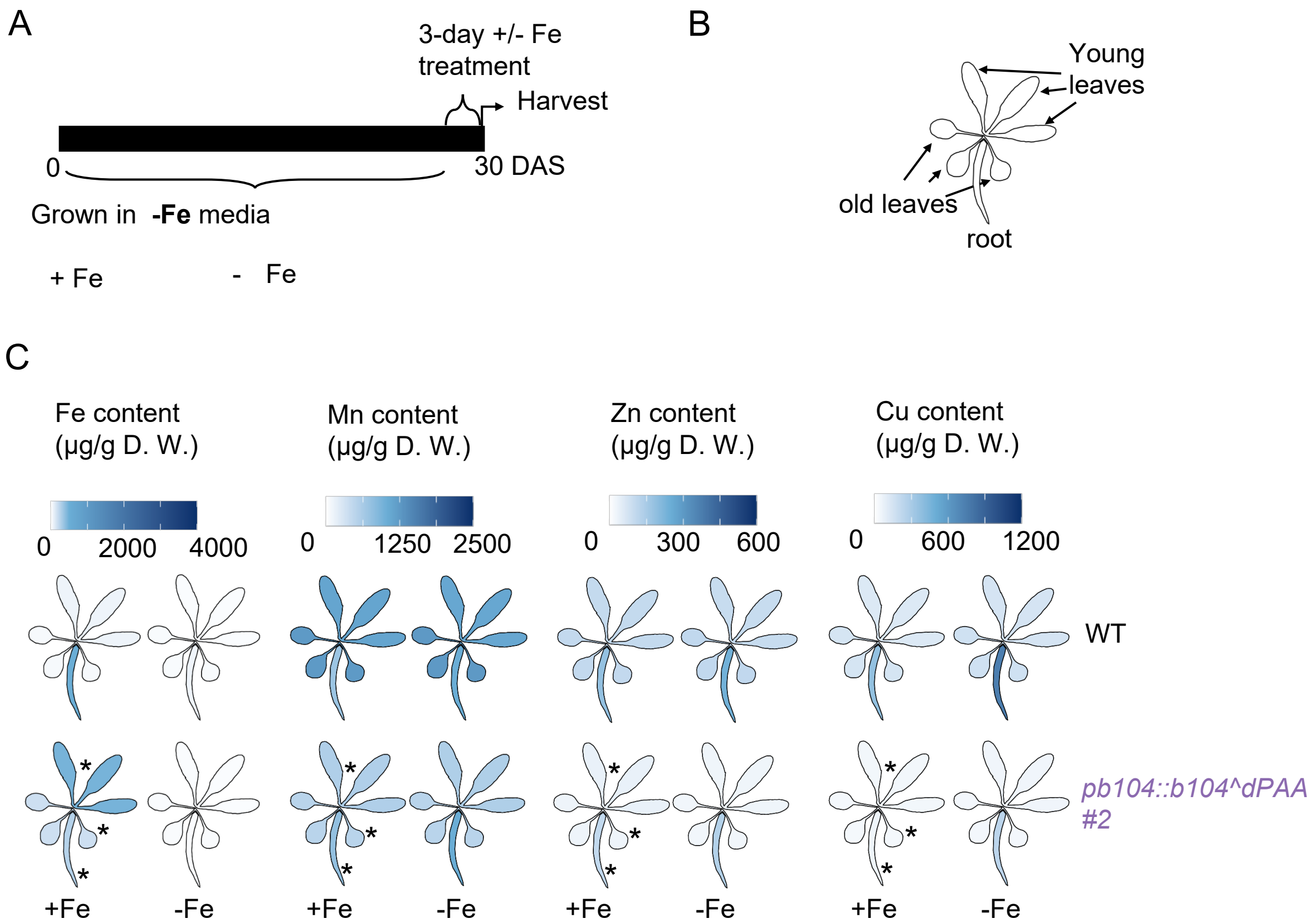

Supplementary figure S10. Tissue-specific metal accumulation in dPAA line #2 grown under iron-deficient conditions.
(A) Experimental setup: Col-0 and *pb104::b104^dPAA line #2* seedlings were grown hydroponically in Fe-deficient (–Fe) media for 27 days, followed by a 3-day treatment with either +Fe or –Fe media. Tissue collection occurred at 30 days after sowing (DAS).(B) Tissue layout: Young leaves, old leaves, and roots were separated to examine tissue-specific metal accumulation (Fe, Mn, Zn, Cu).(C) Heatmap of metal content: The distribution of Fe, Mn, Zn, and Cu content (in µg/g dry weight) in dPAA line #2 and Col-0. The color scale reflects metal concentrations, with darker blue shades indicating higher content. *pb104::b104^dPAA line #2* exhibited significant Fe accumulation in young leaves after Fe resupply, in contrast to Col-0, where most Fe remained in the roots. Data represent the mean values from three biological replicates (n = 3). Elemental content was measured by ICP-MS. The plot was generated using the ggPlantMap package in RStudio. Asterisks indicate genotypes that differ significantly from WT within the same tissue and treatment condition ($p < 0.05$), as determined by two-way ANOVA and Tukey's post hoc test (n = 3 for each group).

Supplementary Figure S11

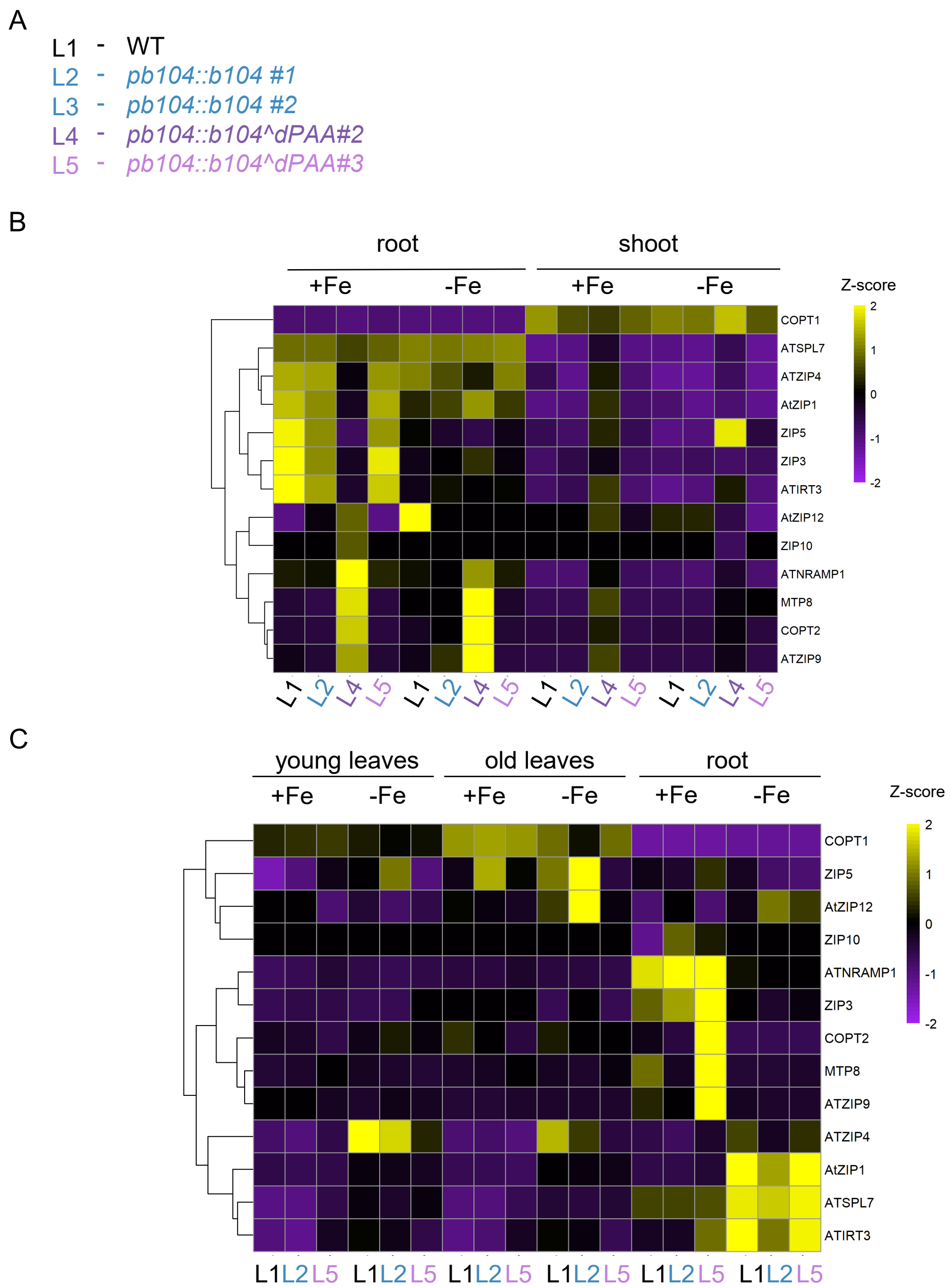

Supplementary Figure S11. Expression profiles of genes involved in Mn, Zn, and Cu homeostasis.
Clustered heatmap showing expression profiles (RNA sequencing) of genes involved in manganese (Mn), zinc (Zn), and copper (Cu) homeostasis across tissues in pb104::b104^dPAA lines under +Fe and –Fe conditions. Genes include metal transporters and the Cu homeostasis regulator SPL7 (Guerinot, 2000; Sancenón et al., 2004; Socha and Guerinot, 2014). Heatmap was generated in RStudio version 4.4.1 using calculated Z-scores of normalized gene expression values. Purple indicates low expression and yellow indicates high expression. Asterisks indicate genotypes that differ significantly from WT within the same tissue and treatment condition ($p < 0.05$), as determined by two-way ANOVA and Tukey's post-hoc test ($n = 3$ for each group).

Supplementary Figure S12

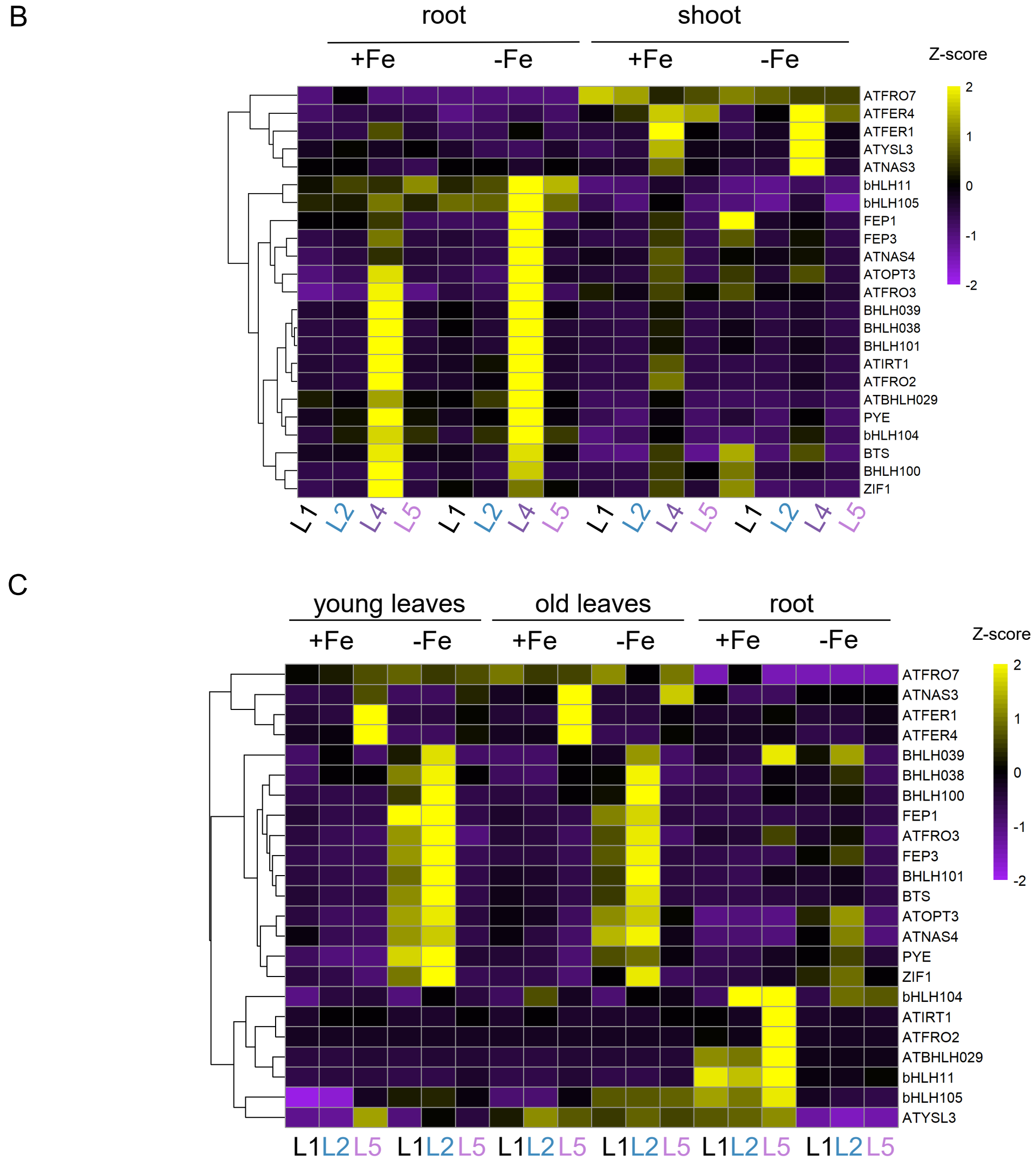

Supplementary Figure S12. Expression patterns of 23 selected Fe homeostasis genes involved in Fe acquisition and mobilization.
Clustered heatmaps showing expression profiles of 23 Fe homeostasis genes (gene selection based on Ngigi et al., 2025; Schwarz et al., 2020). Heatmaps were generated in RStudio version 4.4.1 using Z-scores of normalized gene expression values across tissues for +Fe and –Fe conditions. Purple indicates low expression; yellow indicates high expression. Asterisks indicate significant differences from WT within the same tissue and treatment ($p < 0.05$, two-way ANOVA with Tukey's post-hoc test, $n = 3$).

Supplementary Figure S13

AD	BD	AD	BD
bHLH104-C	BTSL1	BTSL1	bHLH104-C
bHLH104-C	BTSL2	BTSL2	bHLH104-C
bHLH104-C-dPAA	BTSL1	BTSL1	bHLH104-C-dPAA
bHLH104-C-dPAA	BTSL2	BTSL2	bHLH104-C-dPAA
Empty	BTSL1	BTSL1	Empty
Empty	BTSL2	BTSL2	Empty
bHLH104-C	Empty	Empty	bHLH104-C
bHLH104-C-dPAA	Empty	Empty	bHLH104-C-dPAA

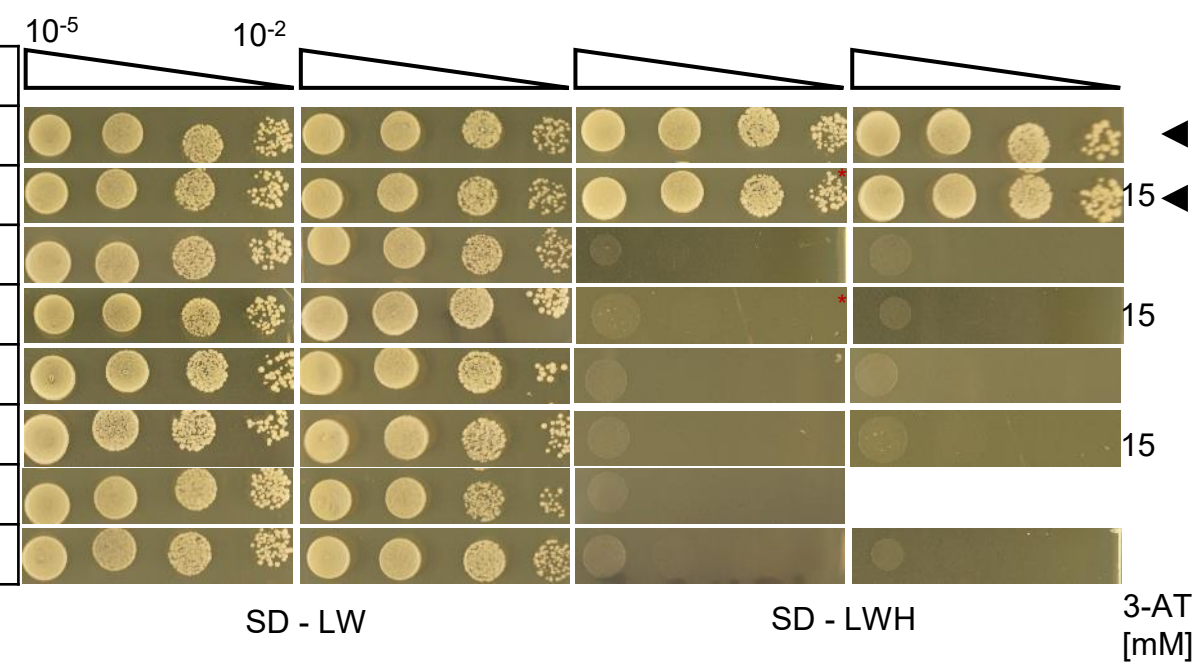

Supplementary Figure S13: Yeast two-hybrid assay results showing protein–protein interactions between bHLH104 BTSL1 and BTSL2.
bHLH104 interacts with BTSL1 and BTSL2, but not bHLH104dPAA. bHLH104^ΔPAA retains the ability to heterodimerize with full-length bHLH104, serving as a control for the presence and expression of the PAA-deleted variant. Full length bHLH104 shows autoactivation in Y2H. Hence bHLH104-C and bHLH104-C-dPAA were used.
Yeast co-transformed with the AD and BD combinations were spotted in 10-fold dilution series (A600 = 10–1–10–4) on SD-LW (transformation control) and SD-LWH plates supplemented with different 3AT concentrations (conc.) as indicated (selection for protein interaction). Negative controls: empty vectors. Arrows indicate interaction.

Supplementary Figure S14

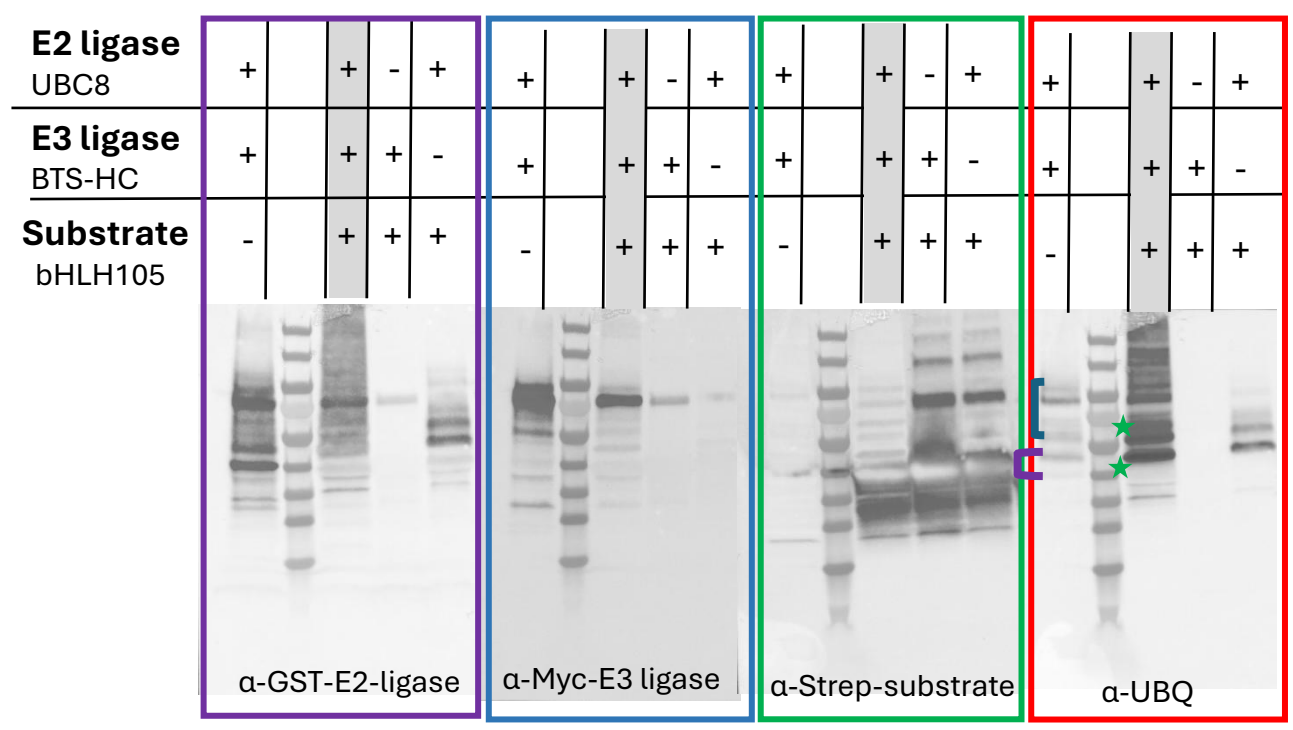

Supplementary Figure S14: Ubiquitination assay showing that bHLH115 undergoes ubiquitination
Ubigate assay showing ubiquitination of bHLH105 in the presence of E1, E2, E3, and ubiquitin (Ub). Immunoblots with anti-GST (E2), anti-Myc (E3), anti-Strep (substrate), and anti-His-UBQ (ubiquitin) confirm protein expression and substrate modification

Supplementary Table 1. Primers used in this study.

fw = forward, rev = reverse, d = delta a.k.a. deletion, -C = C-term, (att)B1/B2 = Gateway B attachment sites for BP reaction.

Primer name	Sequence (5' to 3')	Purpose	Origin
Amplification of full-length CDS or deletion constructs for Y2H			
bHLH104-C_B1 fw	GGGGACAAGTTTGTACAAAAAAGCAGGCTTCATGGCTCT	cloning of bHLH104-C (attB1)	lichtblau 2023
bHLH104-C-d_B2 rev	GGGGACCACTTTGTACAAGAAAGCTGGGTCTTAAGGCCTGAGTTCTTGAT	cloning of bHLH104-C-d (attB2)	This study
bHLH104_B2 rev	GGGGACCACTTTGTACAAGAAAGCTGGGTCTTAAGCAGCAGGAGGCCTG	cloning of bHLH104-C (attB2)	lichtblau 2022
Cloning bHLH104 promoter and CDS for transgenic lines			
bHLH104 fw	aacaggtctcaggctggatgtatccttctctcgacg	Cloning of bHLH104/bHLH104-d CDS	This study
bHLH104 rev	aacaggtctcactgaAGCAGCAGGAGGCCTGA	Cloning of bHLH104 CDS	This study
bHLH104-d rev	aacaggtctcactgaAGGCCTGAGTTCTTGAT	Cloning of bHLH104-d CDS	This study
pbHLH104 fw	AACAGGTCTCAACCTCTAGCTCTGAGAAGCGGCATC	Cloning of bHLH104 promoter	
pbHLH104 rev	AACAGGTCTCATGTTTTGAGAGTCTCCAAACAAATT	Cloning of bHLH104 promoter	This study
Amplification of full-length CDS or deletion constructs for Ubigate			
BTS-HC fw	ttgaagacaaaATGGCAGAACG	Cloning BTS HC fragment	This study
BTS-HC_rev	ttgaagacaaaagcTTAGCTGCTGGTG	Cloning BTS HC fragment	This study
optbhlh104-C fw	GGGGACAAGTTTGTACAAAAAAGCAGGCTTCATGACCGATAAACCGG	Cloning bHLH104 in pUGTP1 (attB1)	This study
optbhlh104 rev	GGGGACCACTTTGTACAAGAAAGCTGGGTCTTATGCTGCAGGCGGA	Cloning bHLH104 in pUGTP1 (attB2)	This study
optbhlh104d rev	GGGGACCACTTTGTACAAGAAAGCTGGGTCTTACGGACGCAGTTCT	Cloning bHLH104 in pUGTP1 (attB2)	This study